ANALYZING THE EFFECTS OF METEOROLOGY ON RADAR MEASURED INDEX OF REFRACTION STRUCTURE PARAMETER

THESIS

Jeffrey W. Budai, Captain, USAF

AFIT/GM/ENP/01M-1

DEPARTMENT OF THE AIR FORCE
AIR UNIVERSITY

AIR FORCE INSTITUTE OF TECHNOLOGY

Wright-Patterson Air Force Base, Ohio

APPROVED FOR PUBLIC RELEASE; DISTRIBUTION UNLIMITED.

20010730 036

ANALYZING THE EFFECTS OF METEOROLOGY ON RADAR MEASURED

INDEX OF REFRACTION STRUCTURE PARAMETER

THESIS
Jeffrey W. Budai
Captain, USAF

AFIT/GM/ENP/01M-1

The views expressed in this thesis are those of the author and do not reflect the official policy or position of the Department of Defense or the United States Government.

AFIT/GM/ENP/01M-1

ANALYZING THE EFFECTS OF METEOROLOGY ON RADAR MEASURED INDEX OF REFRACTION STRUCTURE PARAMETER

THESIS

Presented to the Faculty

Department of Engineering Physics

Air Force Institute of Technology

Air University

Air Education and Training Command

In Partial Fulfillment of the Requirements for the

Degree of Master of Science

Jeffrey W. Budai, B.S.

Captain, USAF

March 2001

ANALYZING THE EFFECTS OF METEOROLOGY ON RADAR MEASURED INDEX OF REFRACTION STRUCTURE PARAMETER

Jeffrey W. Budai, B.S.

Captain, USAF

Approved:

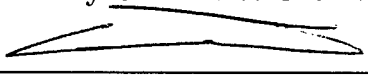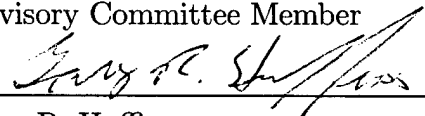|	
Michael K. Walters (signature)	2 MAR 01
Michael K. Walters	Date
Advisory Committee Chairman	
(signature)	2 MAR 01
Glen P. Perram	Date
Advisory Committee Member	
Gary R. Huffines (signature)	2 Mar 2001
Gary R. Huffines	Date
Advisory Committee Member	
Frank D. Eaton (signature)	February 20 2001
Frank D. Eaton	Date
Advisory Committee Member	

Preface

The goal of this work is to describe how meteorology affects turbulence in the index of refraction. Those modeling optical turbulence and attempting to parametrize weather's effects will find this work useful. Hopefully, findings will allow forecasters to make accurate forecasts of optical turbulence for regions of the atmosphere.

Jeffrey W. Budai

Table of Contents

List of Figures

List of Tables

Abstract

Forecasting optical turbulence is essential for the Air Force's Airborne Laser program to optimize placement of aircraft. To find how meteorology affects C_n^2, the intensity of turbulence in the index of refraction, case studies of synoptically interesting times are first chosen. Correlation coefficients are then computed between radar measured C_n^2 and meteorological quantities. The potential for mechanically turbulent activity, quantified by the variance of radar measured wind speed, is looked at.

In the analysis of this work, six meteorological features were found likely to affect C_n^2. Two of the features are directly related to potential refractivity, M, and the other four are related to the various other parameters in C_n^2, grouped into one called P.

The two meteorological features associated with affecting potential refractivity, and thus C_n^2, are jets and inversions. North of jet core level in the northern hemisphere, higher values of C_n^2 can be found north of the jet core, with lower values to the south. This is a result of synoptic-scale dynamics expressed in the thermal wind relationship. The other meteorological feature is temperature inversions. Typically higher values of C_n^2 can be found just above inversions, in the warmer side, with comparatively lower C_n^2 values underneath.

The remaining four features are related to meteorological effects on P. The first is bands of high C_n^2 occurring within regions of strong vertical wind shear. The second feature is high C_n^2 occasionally seen underneath inversions during the approach of jets that are associated with gravity wave activity. The other two meteorological features are tropopause boundaries and trough passage. High values of P are seen along the upper and lower tropopause boundaries and during trough passage.

ANALYZING THE EFFECTS OF METEOROLOGY ON RADAR MEASURED INDEX OF REFRACTION STRUCTURE PARAMETER

I. Introduction

1.1 Motivation

Many new complex weapon systems depend upon being able to monitor, measure, or propagate electromagnetic energy through the atmosphere. One such system is the Air Force's Airborne Laser (ABL) platform. The ABL is a laser weapon system consisting of a high-powered chemical laser mounted on a Boeing 747 with the intent of concentrating its laser beam on ballistic missiles, hoping to destroy them (2:4). In order to destroy a missile, the laser needs to have its power concentrated on the target for a given amount of time.

Unfortunately, turbulence in the atmosphere has many adverse effects upon laser beams. A beam's energy can spread out, decreasing the concentration of power on a target. As a beam spreads out it can interact with itself, causing scintillation effects, and also ruin the phase coherence of the beam. Further, a beam can be bent off target; and if it does manage to reach its target, it can wander about. Fortunately, the ABL will be equipped with adaptive optics technology to help compensate for turbulence. However, knowing how the atmosphere affects turbulence will be extremely important to planners who will deploy this high-profile, advanced weapon system; not only during actual deployments, but during the testing and demonstration of ABL capabilities as an effective theater missile defense system. The current Presidential Administration has stated its commitment in deploying an effective missile defense system.

1.2 Problem and Importance

The ABL program office is working to find a process which will allow planners to optimize the placement of the ABL aircraft. The Atmospheric Development Branch of the ABL program office is working to develop an Atmospheric Decision Aid (ADA) for the ABL. The ADA will be part of the Tactical Decision Aid which will integrate weather, intelligence, and operational data to optimize the ABL flight path (4). Operational capability of the ADA is planned for the summer of 2002 (5).

The Atmospheric Development Branch is interested in parametrizing optical turbulence, which is turbulence in the index of refraction for optical wavelengths. The variable C_n^2, the index of refraction structure parameter, is used to quantify the intensity of turbulence in the index of refraction. The parametrization of C_n^2 will be part of a model used to predict optical turbulence in the atmosphere (5). Understanding how weather affects C_n^2 is absolutely essential to any parametrization.

1.3 Purpose and Scope of Work

The purpose of this work is to find how meteorology affects turbulence in the index of refraction. Various weather features, such as jets and troughs, are routinely predicted in the atmosphere with fairly good reliability. Knowing how turbulence relates to these features, one could generally predict whether turbulence would be high or low in a region by its relation to the feature. Understanding where turbulence occurs helps in finding out why it occurs, aiding in parametrization of turbulence.

High-resolution C_n^2 data are available from the White Sands Missile Range (WSMR) 50 MHz radar. Being in the VHF of radar frequencies, its turbulence data are affected by moisture content of the atmosphere, unlike optical frequencies. Above 8 km, especially above the troposphere, moisture's impact on VHF radar measured C_n^2 is greatly reduced as air is typically very dry. Therefore, this work focuses on heights above 8 km where the WSMR C_n^2 data become very similar to optical turbulence C_n^2. As the ABL aircraft's operational flight level is about 12

km (2:7), this is quite acceptable. The top of the radar's range is just over 18 km. Features in the radar's turbulence data will be looked at to answer why they are there, how long they persist, and how they correlate to atmospheric data.

The results of this work will be used in the Atmospheric Development Branch's parametrization of C_n^2, improving the current model and increasing the accuracy of optical turbulence forecasts for ABL planners. Also, the analysis of data in this work will be used in the interpretation of C_n^2 data coming from the 50 MHz radar at Vandenberg AFB, which will begin taking measurements this year (5). The analysis of data in this work will also serve as a guide for forecasters in forecasting optical turbulence without the aid of a computer model for C_n^2.

1.4 Summary of Results

Two major ways were found in which meteorology affects C_n^2. The index of refraction structure parameter, C_n^2, can be expressed as a product of several parameters, P, and potential refractivity squared, M^2; that is, $C_n^2 = PM^2$ (11:58). Potential refractivity is an expression of vertical temperature gradients and several meteorological variables, such as pressure and moisture content (12:823). The quantity P is a product of several parameters used in the description of turbulent flows, such as scales of turbulent motion and kinetic energy dissipation rates, which are typically difficult to parametrize. More on the theory behind C_n^2 is briefly covered in the next chapter. From these two ways in which meteorology affects C_n^2, six major features were found in the analysis of this work and are described below. Figure 1 graphically displays these features.

Of the six major features found in the analysis of this work, two are directly related to potential refractivity, M. The first feature can be seen in Figure 1 (a). North of jet core level in the northern hemisphere, higher values of C_n^2 can be found north of the jet core, with lower values to the south. This is a result of synoptic-scale dynamics expressed in the thermal wind relationship. The other

3

(a) Jet Stream Location

(b) Temperature Inversions

(c) Strong Vertical Shear

(d) Gravity Wave Activity

(e) Tropopause Boundaries

(f) Trough Passage
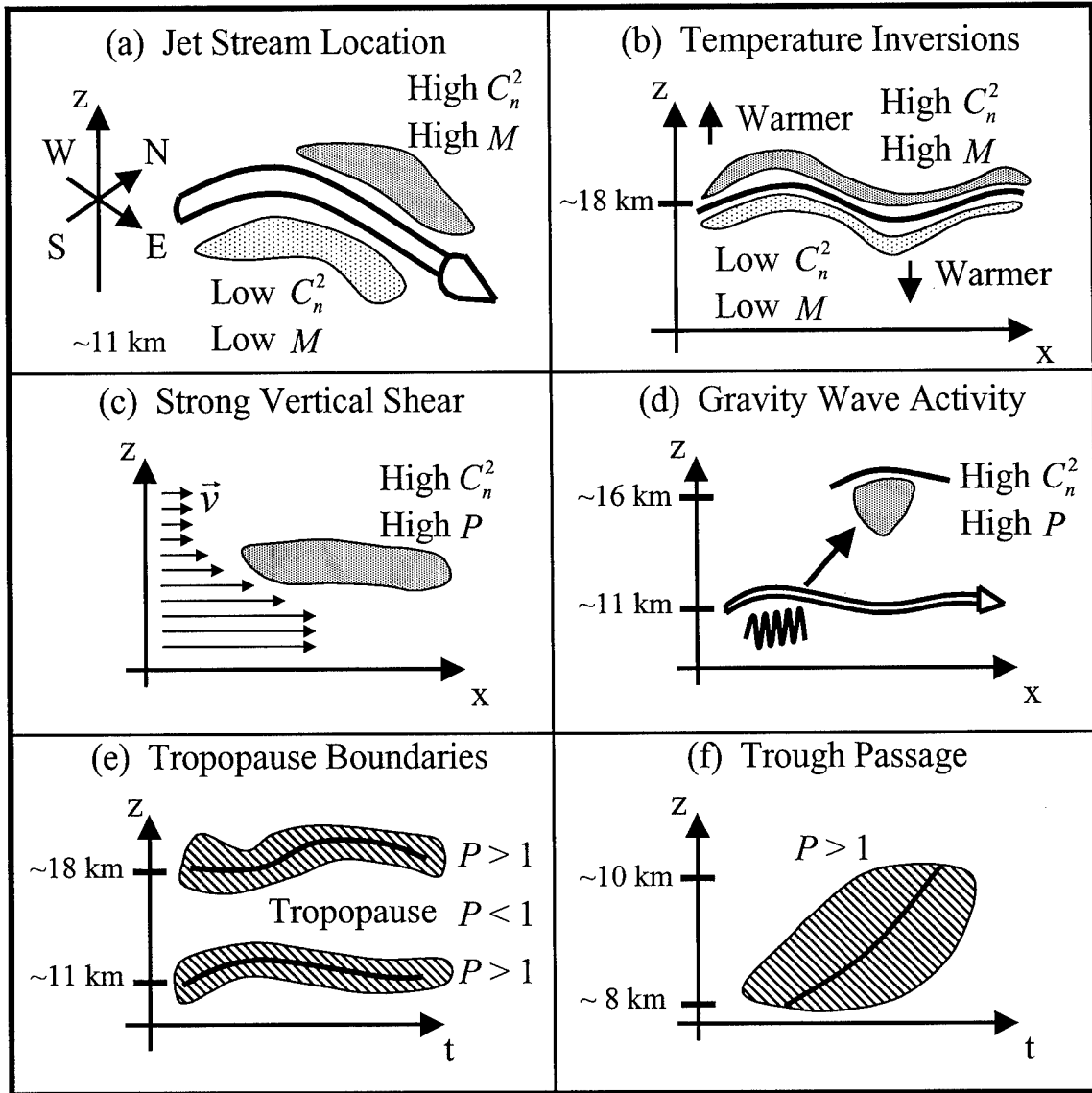
Figure 1   Highlights of findings.   Several meteorological features affect C_n^2, given by $C_n^2 = PM^2$.   (a) At jet core level in the northern hemisphere, high C_n^2 can be found north of a jet core, with lower values to the south.   (b) C_n^2 is typically higher just above inversions.   (c) Bands of high C_n^2 occur within regions of strong vertical wind shear.   (d) High C_n^2 is occasionally seen under inversions during the approach of jets that are associated with gravity waves.   (e) Along the upper and lower tropopause boundaries, values of P are typically greater than one.   While between the tropopause boundaries, values of P are usually less than one outside of mechanically turbulent areas.   (f) Large values of P are seen with the passage of troughs.   Heights are above ground level of the WSMR radar, which is 1220 m above mean sea level.

meteorological feature which affects C_n^2 is temperature inversions. Typically higher values of C_n^2 can be found just above inversions, in the warmer side, as a result of warmer temperatures increasing potential refractivity, resulting in higher C_n^2. This effect is shown in Figure 1 (b).

The remaining four features are related to meteorological effects on P. The first feature is the effect of strong vertical wind shear on P. Bands of high C_n^2 occur within regions of strong vertical wind shear. The bands of high C_n^2 cannot be accounted for by potential refractivity alone. The second feature is high C_n^2 occasionally seen underneath inversions during the approach of jets that are associated with gravity waves. Gravity waves might be propagating kinetic energy into regions underneath inversions, providing turbulent kinetic energy and enhancing C_n^2. The other two meteorological features which affect C_n^2 are tropopause boundaries and trough passage. High values of P are seen along the upper and lower tropopause boundaries and during trough passage. Values of P are usually much greater than 1 along the boundaries and during passage of troughs. Values of P are typically less than one between the tropopause boundaries, and outside of mechanically turbulent regions. Figures 1 (c) through (f) display these meteorological effects on C_n^2.

1.5 Thesis Organization

This chapter presented the motivation behind and the importance of this work. In the next chapter, several important concepts are defined. The theory of turbulence in the index of refraction is covered, as well as general information about the WSMR 50 MHz radar which measures turbulence. The third chapter describes the data sets which are available for this work. After the data sets are described, the methodology for solving the problem is covered in the fourth chapter. The fifth chapter presents a detailed data analysis, employing the methodology given in the fourth chapter. A conclusion follows with a summary of findings and a recommendation for future work in the field.

5

II. Subject Background

This chapter provides a background of important concepts and previous findings. First, a few characteristics which help define turbulence are mentioned. Next, a brief discussion on the theory behind turbulence in the index of refraction is given, followed by an overview of the WSMR radar. Lastly, recent work with the WSMR radar is covered.

2.1 Theory

2.1.1 Turbulence. Brief definitions of turbulence tend to be vague. It is best, however, to mention some important characteristics that all turbulent flows have. Randomness is one of the most obvious characteristics. This characteristic of the irregularity of flows makes statistics a useful way to describe them. Diffusion, the rapid rate of mixing of properties in a medium, is another fundamental characteristic of turbulence. The last important characteristic of turbulent flows mentioned here is dissipation. Energy in turbulent flows is transferred to the internal energy of the medium through viscous losses. Without a constant supply of energy, turbulent flows die out. All turbulent flows have these characteristics, and more. Turbulence in the index of refraction of the atmosphere is of primary importance for this work.

2.1.2 Index of Refraction Turbulence. Random fluctuations in the index of refraction of air have an effect on the propagation of electromagnetic energy. Statistics are used to describe the randomness of these fluctuations. Structure functions, developed by Kolmogorov, are used to describe random functions and the intensity of random fluctuations (11:9). Tatarski's theory (11:27-58) of turbulence in the index of refraction is based off of large-scale eddies transferring their energy down to smaller scales where eventually viscous losses dissipate energy, transferring energy into heat. Fluctuations in the index of refraction are brought about by this

mixing. The structure function for the index of refraction (11:58) is given by

$$D_n(r) = \begin{cases} C_n^2 r^{2/3} & \text{for } l_0 < r < L_0 \\ C_n^2 l_0^{2/3} \left(\dfrac{r}{l_0} \right)^2 & \text{for } r < l_0 \end{cases} \tag{1}$$

where C_n^2 is the index of refraction structure parameter. It is a measure of the intensity of turbulent fluctuations in the index of refraction, measured a distance r apart. C_n^2 has dimensions of $[\text{L}]^{-2/3}$. The outer scale of turbulence, the characteristic size of the large-scale eddies, is L_0 while the inner scale of turbulence is l_0. The inner scale of turbulence is where energy is dissipated into heat. The range between the two scale sizes is the inertial subrange.

The index of refraction structure parameter is

$$C_n^2 = a^2 \alpha' L_0^{4/3} M^2 \tag{2}$$

where a^2 is a universal constant, α' is a ratio of eddy diffusivities, and the potential refractivity is

$$M = c_2 \frac{p}{T\theta} \frac{\partial \theta}{\partial z} \left(1 + c_3 \frac{q}{T} - \frac{c_3}{2} \frac{\partial q}{\partial z} \frac{\theta}{T} \left(\frac{\partial \theta}{\partial z} \right)^{-1} \right) \tag{3}$$

with $c_2 = -7.76 \times 10^{-3} \dfrac{\text{K m s}^2}{\text{kg}}$, and $c_3 = 1.55 \times 10^4$ K (12:823). Other symbols have their usual meteorological meanings.

For this work, C_n^2 is defined more simply as

$$C_n^2 = PM^2 \tag{4}$$

grouping a^2, α', and $L_0^{4/3}$ into one parameter P.

2.2 WSMR 50 MHz Radar

Measurements of C_n^2 used in this work came from the 50 MHz radar at White Sands Missile Range, New Mexico. The radar operated there for many years, but was recently moved to Vandenberg AFB. At 1220 m above mean sea level, the radar was located at 32°24′N, 106°21′W in the Tularosa basin, about 60 km northeast of El Paso, Texas (9:82). This site is located between two mountain ridges, the Organ Mountains to the west and the Sacramento Mountains to the east. Both mountain ridges run north-south. The climate is a semi-arid, highland desert.

The radar consists of three fixed coaxial-collinear antennas (9:82). One antenna points 15° off-zenith towards the north, another 15° off-zenith towards the east, and the remaining one points in the vertical. Each antenna measures returned back-scattered power for one full minute, completing a full profile of data every three minutes. This temporal resolution makes the radar a good source of data for comparison with meteorological events.

A very important fact is the 50 MHz radar is calibrated to measure C_n^2 (9:82). The calibrated range is from 10^{-20} to 10^{-13} m$^{-2/3}$. More radar parameters are listed in Nastrom and Eaton's work with the 50 MHz radar (9:82). More on the theory behind the scattering of electromagnetic energy and its relationship to C_n^2 can be read in other works such as Tatarski (11:59-80) and VanZandt (12).

2.3 Previous Work

Recent work with the WSMR 50 MHz radar has found that gravity wave activity and small-scale turbulence are enhanced when winds are strong near 5.6 km (9:81). The greatest enhancements are found between 16 km and 18 km. Nastrom and Eaton propose that enhanced turbulence is due to upward propagating gravity waves originating in the troposphere during periods of strong winds, and that the local static stability and winds are not enough to account for the increased turbulence seen.

In a later paper, they reached several conclusions concerning the variability of winds and turbulence seen by the WSMR 50 MHz radar. The hourly variances of all three wind components follow a lognormal distribution (10:2147). However, the variances of the horizontal winds are mostly anisotropic; that is, small scale turbulence in winds has a preferred direction. Also, in the troposphere the mean of $\log(C_n^2)$ tends to be greater during the summer. In the stratosphere, however, no evidence of a seasonal trend in the mean of $\log(C_n^2)$ exists.

Recent work from an Air Force Institute of Technology student involved multiple linear regression between optical turbulence and synoptic-scale meteorological variables (3:4). The three minute WSMR 50 MHz radar data were averaged into 6 hour increments and then multiple linear regression was employed. Capt Hajek found that weak linear relationships exist between some variables and averaged $\log(C_n^2)$. Variables with the strongest correlation are temperature, bulk Richardson number, and the total and ageostrophic wind components.

This work is follow-on research to Capt Hajek's work done from 1997 to 1998.

III. Data Description

Three good sets of data are available for analysis. The WSMR 50 MHz radar has produced excellent temporal and spatial resolution C_n^2 data, as well as horizontal wind speed data. The National Centers for Environmental Prediction (NCEP) and National Center for Atmospheric Research (NCAR) have large-scale meteorological data available for synoptic analysis. Fine-scale meteorological data, for better comparison with the radar data, are available from the Air Force Combat Climatology Center (AFCCC).

3.1 WSMR Radar Data

Raw data from the WSMR 50 MHz radar have already been processed and the following fields are available from 1996: C_n^2, zonal and meridional components of wind, and a quality control parameter. Vertical velocity data are not available.

Ten months of processed data, in 3 minute increments, are available from 1996. There are data gaps, however. March and April have the most data. July, August, and September have a few days of missing data; while February, May, June, and October are missing more than one half of their days in data. The spatial resolution of the processed data is good. In 150 m increments, 112 height ranges are available from 2075 m to 18,725 m above ground level.

The quality control parameter in the processed data was generated from an algorithm developed by Weber and Wuertz (13:1) of the National Oceanic and Atmospheric Administration. Data were compared to themselves in height and time for consistency and a positive integer from 0 to 100 was assigned. The lower the number, the better the data. Since data were compared to themselves, errors were not always detected by the consistency check (13:2).

To compare the fine-scale temporal resolution radar data to the comparatively coarse meteorological data (discussed later) the radar data needs to be put into a

10

30 minute intervals
about each 3 hour point

Median values after QC

$\Delta t = 3$ min

$\Delta t = 3$ hr
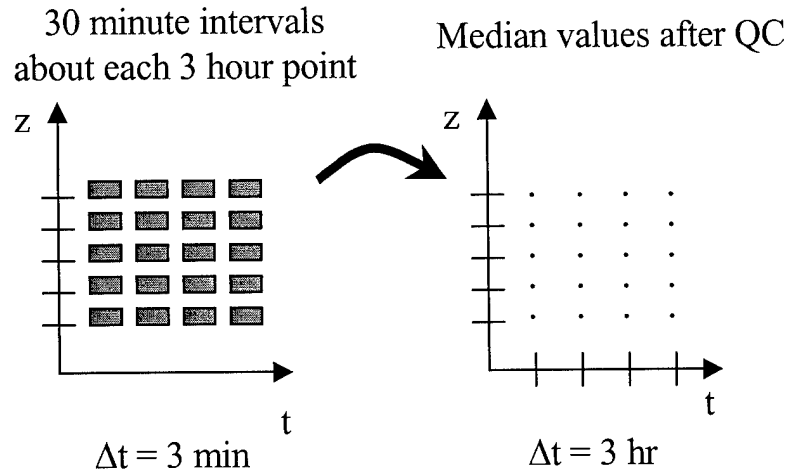
Figure 2   Radar data conversion.   For each height, data are taken within a 30
minute window every 3 hours; quality control is performed on those data,
then the median of the good data is taken.   The final data set has been
quality controlled and is in 3 hour intervals for comparison with other
meteorological data.

slightly different format.   Fine-scale meteorological data are available in 3 hour

increments at 00 UTC, 03 UTC, 06 UTC...   To put the radar data into this format,

a 30 minute window of data, centered on every 3 hour point, is taken.   Data with a

quality control parameter greater than 15 are considered bad data and not included

in the 30 minute window of data.   The median of the remaining set of data is taken

and that median is assigned to be the representative value at that 3 hour point.   For

reference, the quality control parameter associated with the median value of C_n^2 is

saved too, as a measure of the quality of C_n^2 at that 3 hour mark.   Figure 2 provides

a picture of the conversion.   With good radar data in an appropriate format, large-

scale meteorological data are needed to overview synoptic situations.   NCEP/NCAR

meteorological data are used for this purpose.

3.2   NCEP/NCAR Reanalysis Data

The NCEP/NCAR started a project in 1991 to take global measurements of

meteorological data, perform quality control, and run a data assimilation system

11

to produce global fields of meteorological data (6:437). After assimilating balloon measurements, surface observations, satellite, and other forms of data, many fields of standard meteorological quantities were produced. These fields cover all of the continental United States and provide an excellent way of observing synoptic features in the atmosphere with reliability.

Temporal resolution of available reanalysis data is in 6 hour increments. Also, the data have a horizontal spatial resolution of 2.5° by 2.5°, roughly 280 km by 280 km. Vertical resolution is 17 pressure levels from 1000 hPa to 10 hPa. While this resolution is fair for observing synoptic-scale features, such as long-wave troughs, jets, fronts, it is not fine enough for comparisons with the more fine-scale radar data. The AFCCC meteorological data do have a good spatial and temporal resolution.

3.3 AFCCC Meteorological Data

AFCCC uses a mesoscale dynamical-numerical model to generate high-resolution gridded data (1:344). The name of the program that generates the gridded data is Advanced Climate Modeling and Environmental Simulations (ACMES). The program uses the NCEP/NCAR reanalysis data, along with earth surface characteristics, as initial conditions. It also assimilates surface and upper-air observations into the program. The model generated grids of data with a resolution of roughly 11 km by 11 km, in 60 sigma-pressure levels over southern New Mexico. A total of 52 variables came with the ACMES data set. The most important of the 52 are shown in Table 1.

A few quantities are derived from the ACMES data set, which can be seen in Table 2. The most important derived quantity is potential refractivity as it has a direct impact on C_n^2 according to theory. The calculation of relative vorticity and horizontal temperature advection does not account for curvature of the earth. The effect of curvature on these calculations is negligible at the latitude of WSMR.

Table 1   Important ACMES variables.

Variable	Description
H_t	Terrain height above mean sea level
u	Zonal wind speed
v	Meridional wind speed
T	Temperature
T_v	Virtual Temperature
θ	Potential temperature
q	Specific humidity
R_i^*	Bulk-Richardson number (BRN)
N^2	Brunt-Väisälä frequency squared
$\sqrt{\left(\dfrac{\partial u}{\partial z}\right)^2 + \left(\dfrac{\partial v}{\partial z}\right)^2}$	Total vertical shear

Table 2   Derived ACMES variables.

Derived Quantity	Description
$-\overrightarrow{v} \cdot \nabla T$	Horizontal temperature advection
$\zeta = \dfrac{\partial v}{\partial x} - \dfrac{\partial u}{\partial y}$	Relative vorticity
$M = c_2 \dfrac{p}{T\theta}\dfrac{\partial \theta}{\partial z}\left(1 + c_3\dfrac{q}{T} - \dfrac{c_3}{2}\dfrac{\partial q}{\partial z}\dfrac{\theta}{T}\left(\dfrac{\partial \theta}{\partial z}\right)^{-1}\right)$ $c_2 = -7.76 \times 10^{-3}\dfrac{\text{K m s}^2}{\text{kg}},\ c_3 = 1.55 \times 10^4\ \text{K}$	Potential refractivity
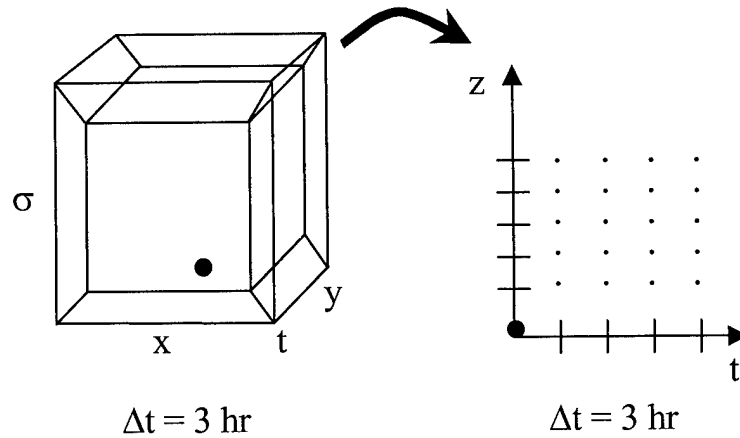
Figure 3   ACMES data conversion. For comparison with radar data, ACMES
            data are converted from sigma-pressure coordinates to height coordinates.
            The closest horizontal grid point to WSMR (2.65 km away) is used for
            vertical profiles.

For comparison with the radar data, the ACMES data need to be converted
from sigma-pressure coordinates to height coordinates: 112 height ranges in 150 m
increments starting from 2075 m above ground level. Since pressure is recorded on
each sigma surface, all variables are logarithmically interpolated to pressure coordi-
nates in 20 hPa increments. After interpolation to pressure coordinates, the hypso-
metric equation is employed to convert to geopotential height coordinates, based off
of mean temperatures in layers. Geopotential heights are converted to geometric
ones using the Smithsonian Meteorological Tables (8:217-219) and the appropriate
equation therein. The closest horizontal grid point to WSMR, 2.65 km away, is
used for vertical profiles of data. Horizontal interpolation is not done as the grid
spacing is roughly 11 km and such interpolation makes little difference in the vertical
profiles. Figure 3 provides a picture of the conversion.

With three good data sets available, the next chapter describes the methodol-
ogy for finding how meteorology affects C_n^2.

IV. Research Methodology

To find how meteorology affects C_n^2, case studies of synoptically interesting times are chosen. Correlation coefficients are computed between radar measured variables and meteorological quantities to see how they relate to each other during each case study. The potential for mechanically turbulent activity and its effect on C_n^2 is looked at too. Mechanical turbulence is quantified by the calculation of the variance of radar measured wind speeds. Each of the methods just mentioned are explained in more depth below.

4.1 Case Studies

To capture different synoptic situations, and how they affect C_n^2, case studies are chosen in the springtime to correspond to times when the polar jet is active in the region of the WSMR radar. The dynamics associated with the polar jet make for an exciting time with meteorological quantities changing. On a synoptic scale, for instance, jets and their associated wind shears have an impact on horizontal temperature gradients and might impact C_n^2 in a predictable way. Three case studies in April 1996 are looked at. The first two case studies are each 7 days long, and the last is 6 days. The length of the case studies is long enough to capture the approach of jets, their associated features, and their departure. To see how meteorological quantities associated with synoptic features relate to C_n^2, correlation coefficients are used.

4.2 Correlation Coefficients

Having vertical profiles of data over time, correlation coefficients are an ideal way to see how quantities relate. The radar data and meteorological quantities over the whole of the case studies are from fairly stationary processes. There are broad fluctuations in values during the case studies, but generally the means of the

15

quantities do not continually grow or decrease over time. Radar C_n^2 varies so wildly over short periods of time, by several orders of magnitude, that the logarithm of C_n^2 is used when computing all correlation coefficients. Taking the log of C_n^2 stabilizes its variance.

Correlation coefficients between $\log(C_n^2)$ and ACMES variables are computed at constant heights. That is, for each height over the entire case study, one correlation coefficient value of lag 0 is computed. Once all of the coefficients are computed, they are plotted in the fashion shown in Figure 4. Correlation coefficients are computed with lag, m, of 0 from the equation

$$r_m(x,y) = \frac{\sum_{i=1}^{N-m} (x_i - \overline{x})(y_{i+m} - \overline{y})}{\sqrt{\left[\sum_{i=1}^{N-m} (x_i - \overline{x})^2\right]\left[\sum_{i=1}^{N-m} (y_{i+m} - \overline{y})^2\right]}} \tag{5}$$

where

$$\overline{x} = \sum_{i=1}^{N-m} \frac{x_i}{(N-m)} \qquad\qquad \overline{y} = \sum_{i=m+1}^{N} \frac{y_i}{(N-m)}$$

After quality control of the radar data, after inconsistent data are removed, gaps are filled in by linear interpolation and extrapolation in time. This does affect correlation coefficient values, but only in a minor way. It was found that the general pattern of correlation coefficients plotted with height changed very little when heavy interpolation was performed, compared to very little interpolation. Values of the coefficients would change by an amount usually less than 0.05 and the overall shape of the curves would remain the same. Filling in data gaps by linear interpolation and extrapolation in time has little effect on the coefficients and the shapes of the curves with height. The shapes of the curves and the relative strengths of local minima and maxima are important to the analysis, not precise numerical values at each height.

16
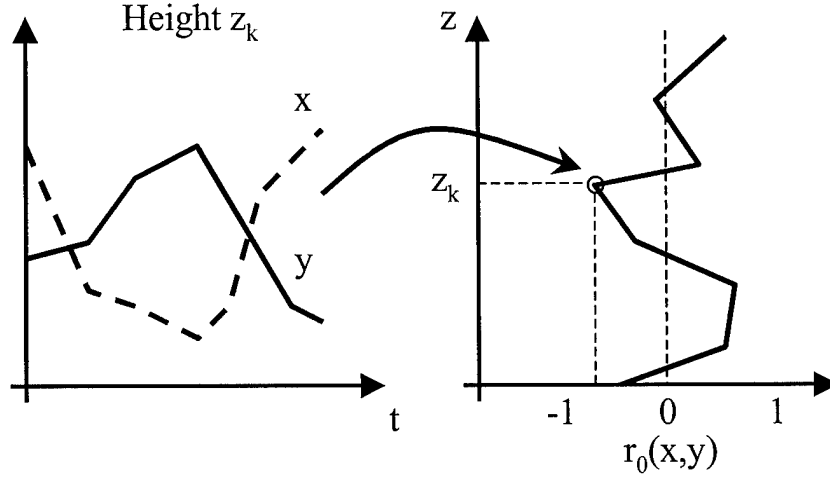
Figure 4   Correlation coefficient computation. For each height, correlation coeffi-
cients are computed over the entire case study period.

4.3   Wind Speed Variance

To identify regions of possible mechanical turbulence, and how they might af-
fect C_n^2, variance of wind speeds is used as an indicator of possible mechanically
turbulent activity.   To illustrate the concept, imagine flying an airplane in an en-
vironment with a sustained wind speed without speed variance.   If the wind speed
becomes randomly modulated from turbulent activity, the variance of the speed will
increase. As the variance of the wind speed increases more, the plane becomes tossed
about from the turbulent motion.   High speed variance does not imply turbulence,
though.   Simple wave motion has speed variance, but might not have the defining
characteristics of turbulent flows.   Though high variance of wind speeds does not
imply mechanical turbulence, high wind speed variance is used as an indicator of
potentially turbulent activity.

Variance of the radar measured wind speeds is calculated over 30 minute inter-
vals, at every three hour mark corresponding to the times of the ACMES variables
and 30 minute medians of radar C_n^2.   Quality control was less stringent to allow
for more variability from the observed radar data.   Obviously bad data were still
removed.   Total wind speed variance is the quantity used to identify possibly me-

17

chanically turbulent areas, which is given by

$$\left(\sqrt{s_u^4 + s_v^4}\right) \tag{6}$$

where

$$s_u^2 = \sum_{i=1}^{N} \frac{(u_i - \overline{u})^2}{N - 1} \qquad s_v^2 = \sum_{i=1}^{N} \frac{(v_i - \overline{v})^2}{N - 1}$$

and

$$\overline{u} = \sum_{i=1}^{N} \frac{u_i}{N} \qquad \overline{v} = \sum_{i=1}^{N} \frac{v_i}{N}$$

V. Data Analysis

Three case studies are chosen from the month of April 1996. Radar data are available in long, continuous blocks with few quality control gaps. The polar and subtropical jets are active throughout the month. The individual case studies are chosen by jet position in relation to the WSMR radar and features which appear in the radar C_n^2 data.

The case studies are analyzed below, one at a time. Each case study begins with a general overview of the synoptic situation and a description of the interesting features seen in the radar data. Each analysis is broken into two layers: the upper troposphere to lower tropopause, and the mid-tropopause to lower stratosphere. The tropopause is defined here not as a single height, but a layer from where static stability rapidly increases and temperature remains fairly constant to the stratosphere, where static stability rapidly increases again and temperature begins to increase with height. The tropopause layer is usually from 11 km to 17 km.

5.1 Case Study 1

5.1.1 Overview. The first case study is chosen for two significant features which appear in a plot of WSMR $\log(C_n^2)$ with height from 00 UTC 17 April 1996 to 00 UTC 24 April 1996. These two features can be seen in Figure 5. The first feature is a series of high and low $\log(C_n^2)$ values occurring at about 12 km. This pattern is significant as it occurs at the proposed flight level of the ABL aircraft (2:7). The other feature is the band of high $\log(C_n^2)$ values occurring at roughly 17 km throughout the period.

An initial inspection of the synoptic situation for this case study is best seen at jet level, close to 200 hPa. In Figures 6 and 7, the polar jet can be seen undulating north and south of the WSMR radar during the week. Superimposing 2-D horizontal wind speed onto the plot of $\log(C_n^2)$, seen in Figure 8, shows the pattern of high and
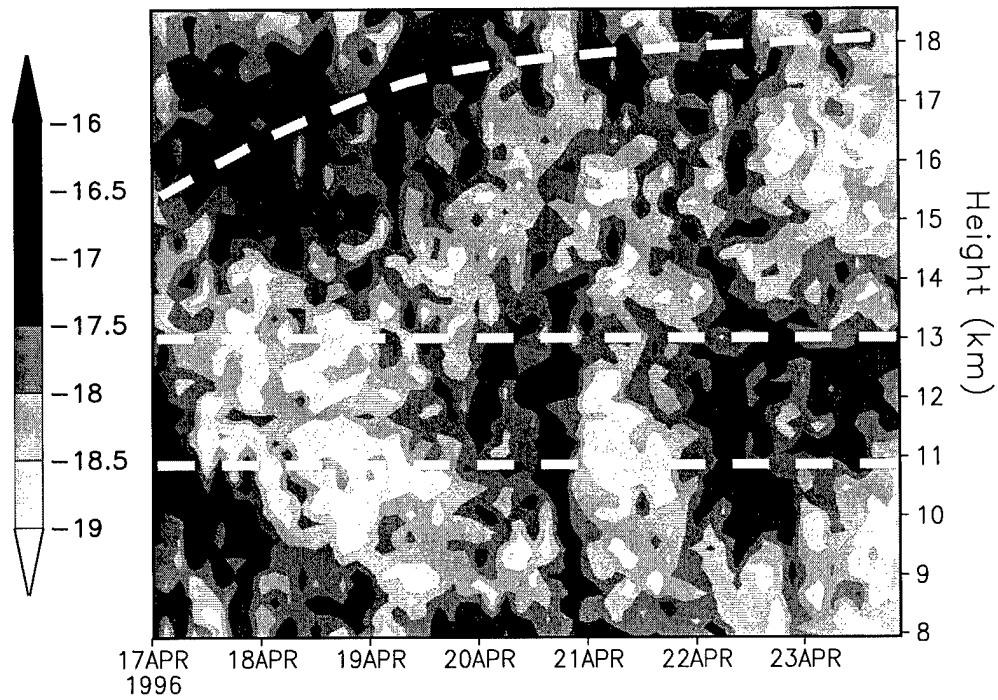
Figure 5   Case study 1 WSMR $\log(C_n^2)$. Two features of interest in this case study are denoted by dashed lines: the series of high and low $\log(C_n^2)$ values between 11 km and 13 km, and the band of high $\log(C_n^2)$ at roughly 17 km.

low $\log(C_n^2)$ values occurring at or occasionally near the region of maximum wind speeds, at about 11 km. The 17 km band feature resides just at and underneath the stratospheric inversion, shown in the superposition of temperature on the plot of $\log(C_n^2)$ in Figure 9. These two synoptic-scale features, the jet position and stratospheric inversion, seem to be associated with the patterns of $\log(C_n^2)$. It is logical then to analyze these $\log(C_n^2)$ features based on height. The analysis below is broken into two general regions: the upper troposphere to lower tropopause, and the mid-tropopause to lower stratosphere.

5.1.2 Upper Troposphere to Lower Tropopause. For this case study, the upper troposphere to lower tropopause region is from 8 km to 13 km. These are heights where the lower tropopause boundary generally exists, heights in which the polar jet core occurs.

To look more closely at how the position of a jet core and the pattern of $\log(C_n^2)$ at 12 km might be related, the horizontal position of the closest jet core with respect to WSMR is denoted in Figure 10. In the figure, it seems that high $\log(C_n^2)$ generally occurs when the closest jet core is to the south, and low $\log(C_n^2)$ occurs when the closest jet core is to the north. Also, the vertical gradient of potential temperature is generally weak in areas of low $\log(C_n^2)$ and high in areas of high $\log(C_n^2)$. The proximity and relative position of the jet core affecting C_n^2 can be explained by the thermal wind relationship.

The high and low $\log(C_n^2)$ pattern is likely a result of the relationship between the vertical shear of wind and horizontal gradients of temperature, expressed in the thermal wind relationship (see Appendix A). North of jet core level in the northern hemisphere, on the lower pressure side, the lower tropopause boundary is lower and static stability is higher. Potential refractivity is generally higher, and thus C_n^2 is higher. At jet level $\log(C_n^2)$ is lower to the south of the jet core as the lower tropopause boundary is higher and static stability and potential refractivity are
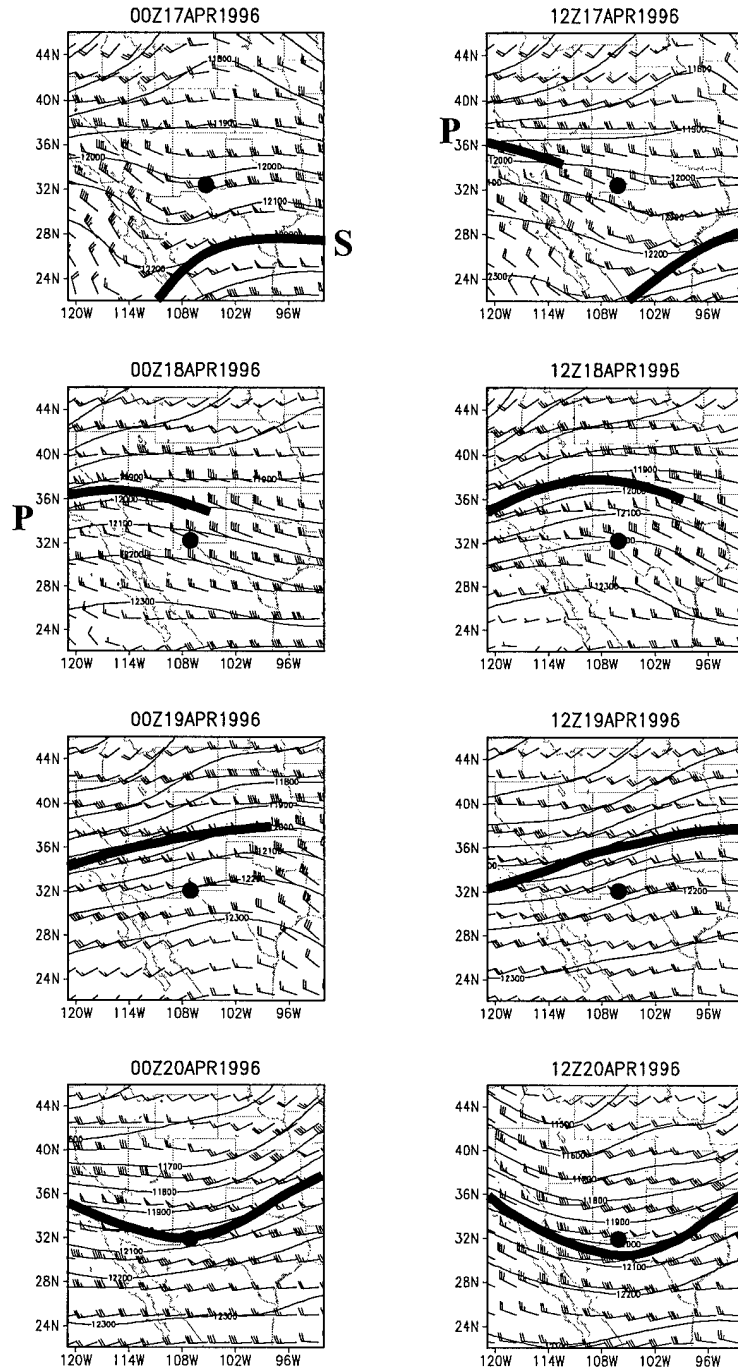
Figure 6   Case study 1 NCEP/NCAR 200 hPa analysis. The polar (P) and sub-
tropical (S) jet cores are denoted by solid line and the WSMR radar by
dot. Geopotential height is in meters MSL and wind barbs are in meters
per second.
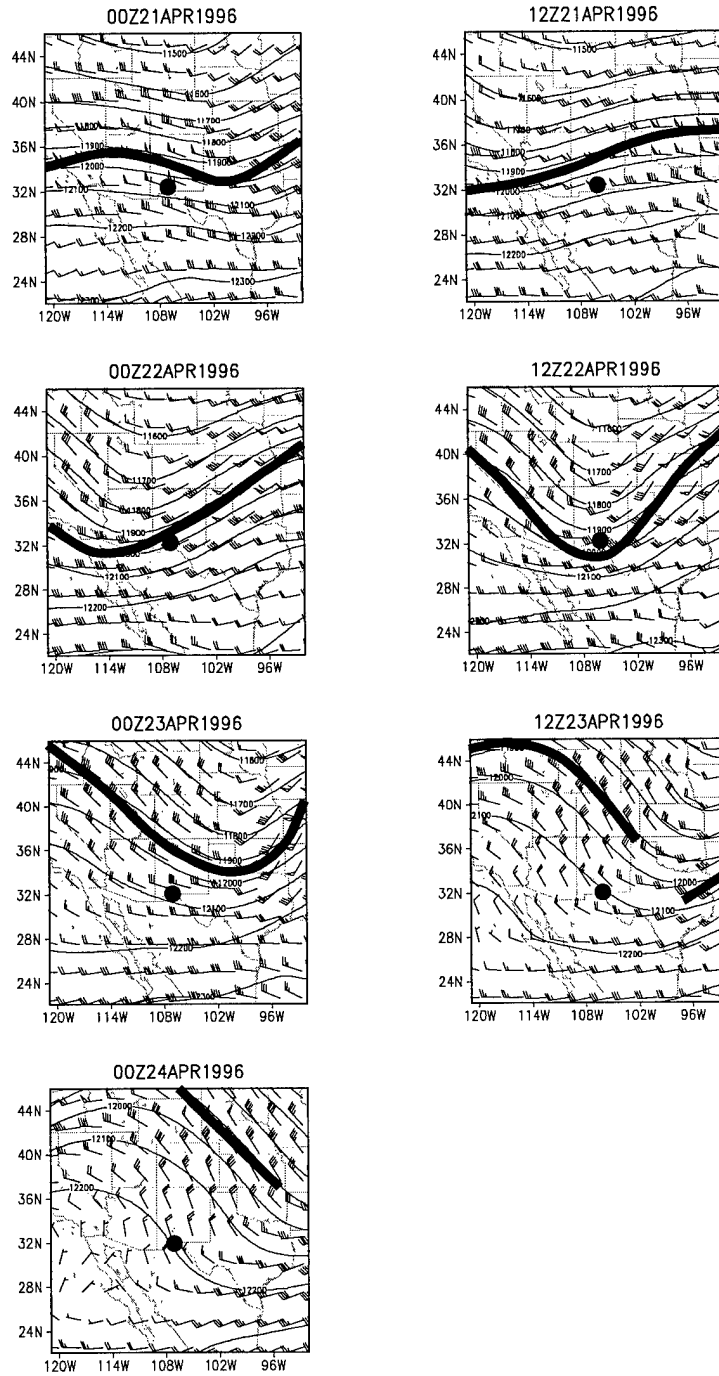
Figure 7   Case study 1 NCEP/NCAR 200 hPa analysis.   The polar jet core is denoted by solid line and the WSMR radar by dot.   Geopotential height is in meters MSL and wind barbs are in meters per second.
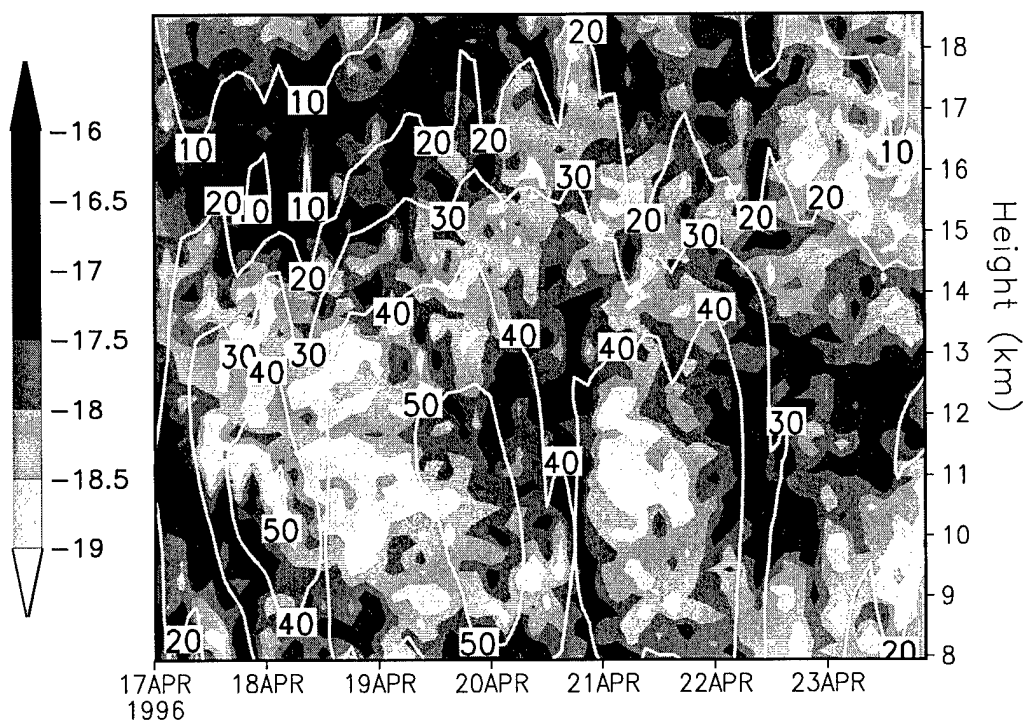
Figure 8   Case study 1 WSMR $\log(C_n^2)$ and ACMES 2-D horizontal wind speed (m/s).
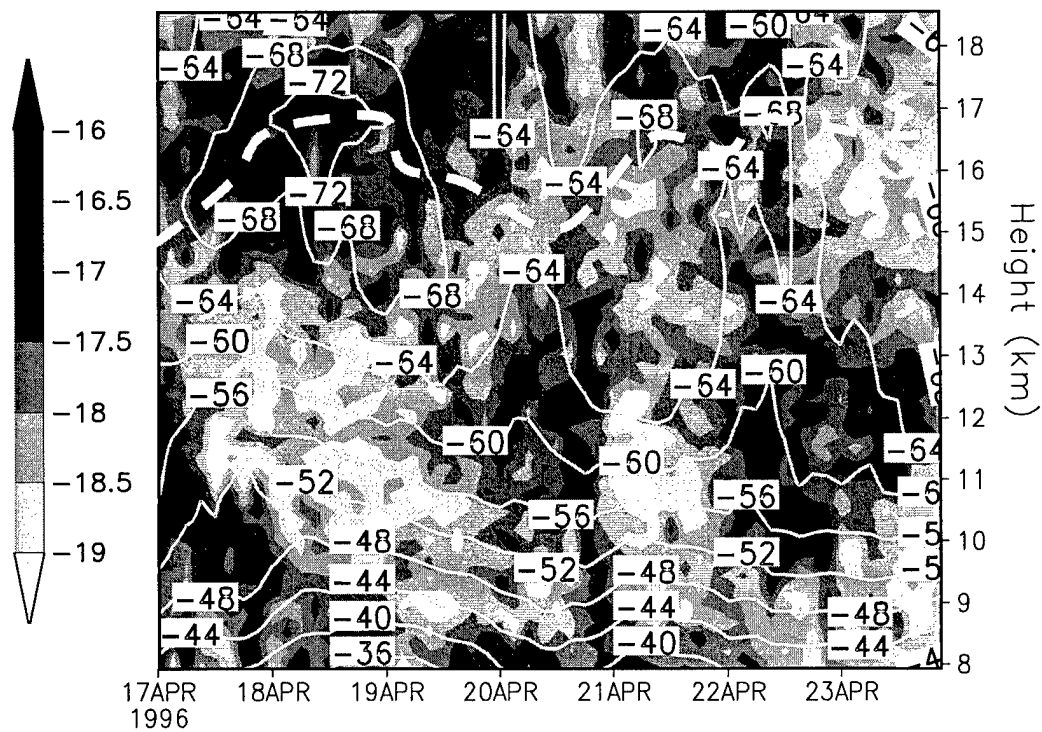
Figure 9   Case study 1 WSMR $\log(C_n^2)$ and ACMES temperature (°C). The base of the stratospheric inversion is denoted by dashed line.
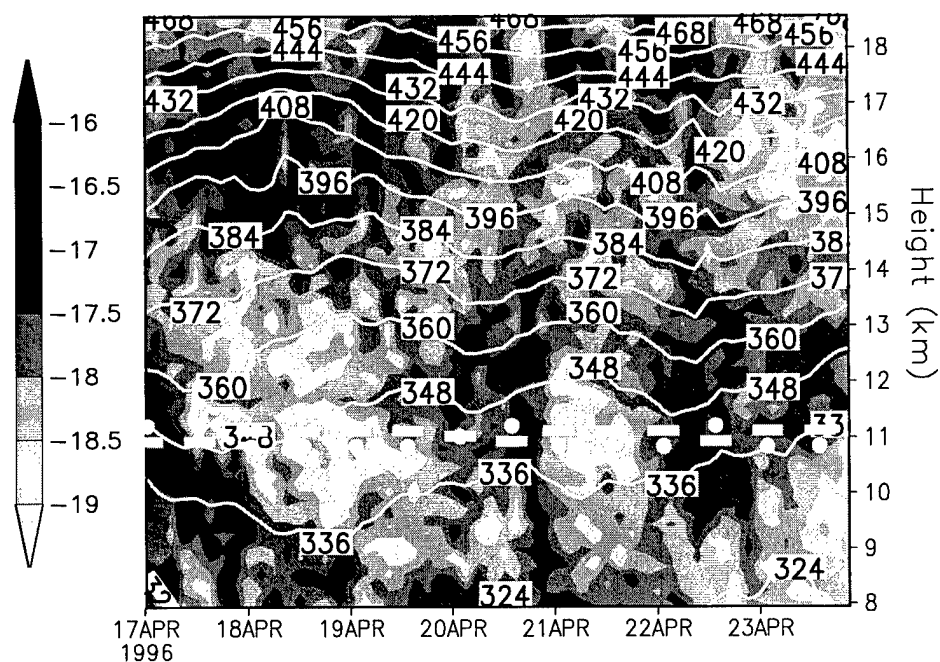
Figure 10   Case study 1 WSMR $\log(C_n^2)$, ACMES potential temperature (K), and closest jet position. Closest jet position is with respect to the WSMR radar and denoted on the figure at about 200 hPa. At 11 km, high $\log(C_n^2)$ generally occurs when the jet core is to the south, and low $\log(C_n^2)$ occurs when the jet core is to the north.

lower. This relationship is apparent in Figure 11 (a) which shows the correlation coefficient between $\log(C_n^2)$ and $\log(M^2)$, the log of potential refractivity squared, computed for each height over the entire period. From 8 km to 13 km the correlation coefficient is roughly 0.6, with a peak of about 0.8 at 12 km. A good relationship between $\log(C_n^2)$ and $\log(M^2)$ exists in the region of the jet core.

Similarly, vertical gradients of temperature and potential temperature have a good correlation with $\log(C_n^2)$ in this layer, not shown in the figure. This is logical as potential refractivity is a function of these vertical temperature gradients. Other correlation coefficients computed between $\log(C_n^2)$ and thermodynamic variables show some interesting features with height. But in general, most correlation coefficients are small, between -0.4 and 0.4. Other correlation coefficients for this case study can be seen in Figure 12.

Summarizing the findings from this jet-level layer, there is good linear dependence between $\log(C_n^2)$ and $\log(M^2)$, the log of potential refractivity squared. The relationship is best at about 12 km, just above the average height of the jet core, with a correlation coefficient value of about 0.8. Similar correlation coefficient values occur with $\log(C_n^2)$ and other variables that are functions of vertical temperature gradients, such as the Brunt-Väisälä frequency. Synoptic-scale dynamics, explained with the thermal wind relationship, appears to play a strong and predictable role in affecting $\log(C_n^2)$ in the upper troposphere and lower tropopause when a jet core is present.

5.1.3 Mid-Tropopause to Lower Stratosphere. The remaining heights in this case study, 13 km to just over 18 km, define the mid-tropopause to lower stratosphere layer. As seen in Figure 13 (a), the lower stratosphere boundary begins roughly between 16 km and 17 km, where the dominant feature of this atmospheric layer resides. The high $\log(C_n^2)$ band typically resides above the stratospheric boundary, in the warmer region, but from 12 UTC 17 April 1996 to 12 UTC 19 April 1996 there

Figure 11   Case study 1 correlation coefficients of lag 0. Coefficients are computed at constant height between WSMR $\log(C_n^2)$ and variables at top of each graph.
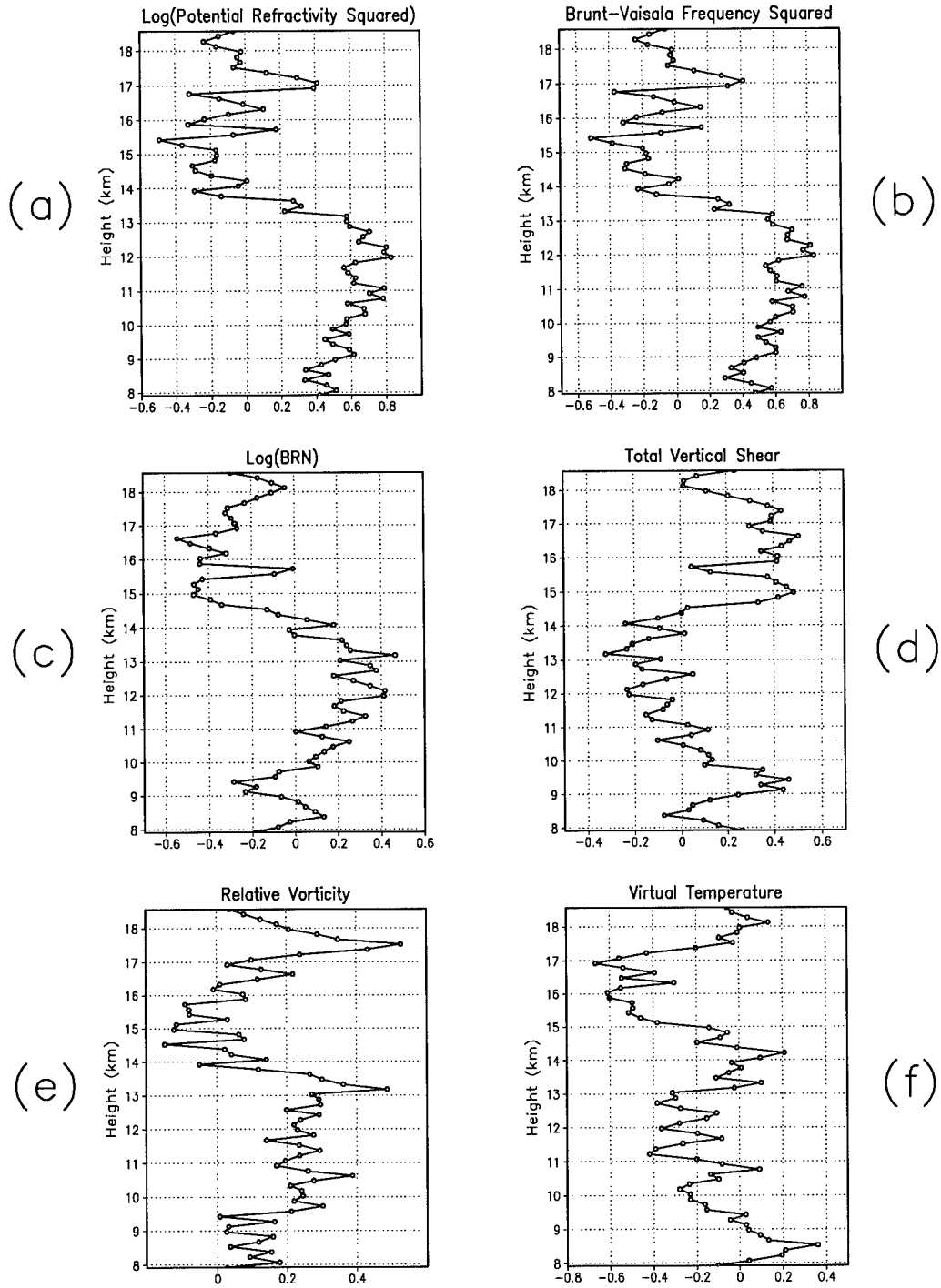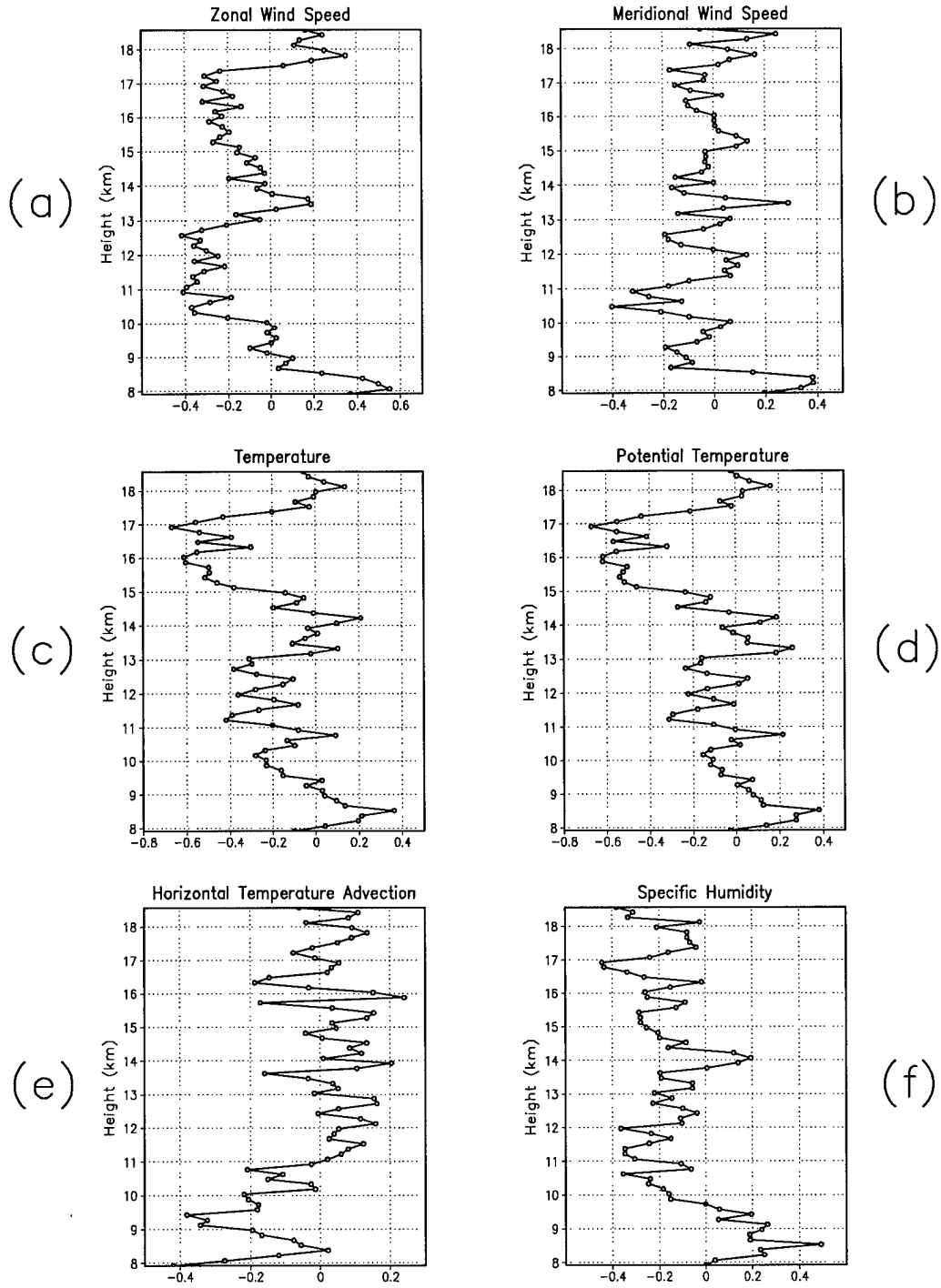
Figure 12   Case study 1 correlation coefficients of lag 0. Coefficients are computed at constant height between WSMR $\log(C_n^2)$ and variables at top of each graph.

is high $\log(C_n^2)$ below the boundary in the colder tropopause region. The part of the band in the stratospheric side can best be explained by the effect a temperature inversion has on potential refractivity.

Potential refractivity, being a function of vertical temperature gradients, is higher above the inversion (in the warm layer) and lower below the inversion (in the cold layer), assuming moisture is negligible or the same in both layers. A detailed description comparing C_n^2 between layers can be referenced in Appendix B. Assuming roughly equal values of P in $C_n^2 = PM^2$, higher values of C_n^2 would be located in the stratospheric side of the inversion, with comparatively lower C_n^2 values underneath. The effect of potential refractivity on the high C_n^2 band can be seen in Figure 13 (b). But this does not explain the high C_n^2 below the stratospheric boundary from 12 UTC 17 April 1996 to 12 UTC 19 April 1996, as M^2 is only high above the inversion. The approach of the polar jet during these times and mechanical turbulence might account for the higher C_n^2 below the inversion.

Figure 6 shows the polar jet approaching and departing the WSMR radar from 12 UTC 17 April 1996 to 12 UTC 18 April 1996. During these times $\log(C_n^2)$ is high underneath the stratospheric inversion, seen in Figure 14 (a). These high $\log(C_n^2)$ values also occur where the Brunt-Väisälä frequency squared is low, as shown in Figure 14 (b). Low Brunt-Väisälä frequency regions favor buoyant instability, compared to higher Brunt-Väisälä frequency regions, as lower Brunt-Väisälä frequencies imply lower buoyant Richardson numbers and a greater likelihood for mechanical turbulence. Possible energy sources for mechanical turbulence are regions which have high Reynolds stress or high shear (7:436). Appendix C shows how these two sources are related to turbulent kinetic energy. Figure 14 (c) shows that ACMES total vertical shear, $\sqrt{\left(\frac{\partial u}{\partial z}\right)^2 + \left(\frac{\partial v}{\partial z}\right)^2}$, roughly occurs in the regions of high $\log(C_n^2)$ underneath the inversion. But looking at the fine-scale WSMR radar data in Figure 15 shows that the band of high $\log(C_n^2)$ underneath the inversion at 15 km, Figure 15 (a), occurs exactly where there is high total vertical shear, Figure 15 (c), calculated
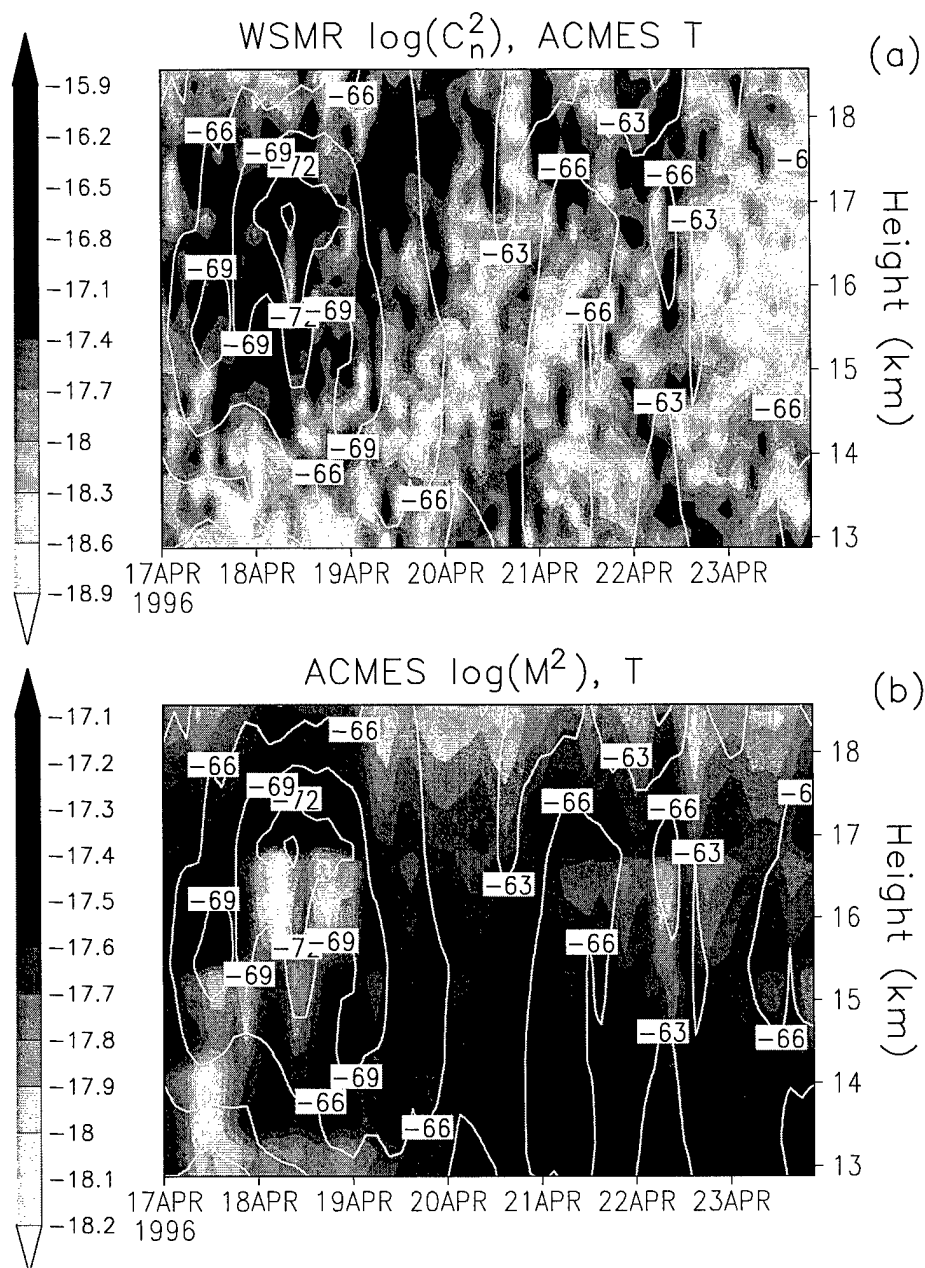
Figure 13   Case study 1 WSMR $\log(C_n^2)$ and ACMES log of potential refractivity squared in the mid-tropopause to lower stratosphere. From 17 April to 19 April, high $\log(C_n^2)$ exists below the stratosphere (a), where $\log(M^2)$ is low compared to other times (b). Temperature (°C) is contoured.

from the radar measured wind speeds. The approach of the polar jet and its strong vertical wind shears at 15 km seems to be providing a source of turbulent kinetic energy in the region, increasing C_n^2.

It is interesting to find high C_n^2 under the inversion occurring in a low Brunt-Väisälä frequency squared environment, compared to values above the inversion. In the upper troposphere to lower tropopause region discussed earlier, high C_n^2 generally occurred in high potential refractivity environments, where Brunt-Väisälä frequency squared was higher. This apparent conflict can be explained as there are two different forms of turbulence at work. Mechanical turbulence seems to be affecting C_n^2 just below the stratospheric inversion, while microscale turbulence parametrized by potential refractivity is affecting C_n^2 more strongly near the lower tropopause boundary and above the stratospheric inversion. This explains why $\log(C_n^2)$ is not correlating well with the log of potential refractivity squared and the Brunt-Väisälä frequency squared in this upper layer, though total vertical shear seen in Figure 11 (d) does correlate more strongly than before.

The effect of mechanical turbulence on C_n^2 is parametrized in P. Values of $\log(P)$, calculated by subtracting ACMES $\log(M^2)$ data from the WSMR $\log(C_n^2)$ data, are shown in Figure 16. High values of P can be seen beneath the stratospheric inversion from 17 April to 19 April 1996 in the region of higher total vertical shear. Perhaps P is greater there as the amount of turbulent kinetic energy available for cascade through the inertial subrange is greater. Above the inversion during these times, P is lower, though still greater than 1.

Other features in Figure 16 show that along the lower stratospheric boundary P is typically greater than 1. In the mid-tropopause, P is typically less than 1, outside of mechanically turbulent areas. At 12 km, P is typically greater than 1 when the WSMR radar is north of a jet, and less than 1 then the radar is south of a jet. Perhaps these features are related to the outer scale of turbulence, L_0, being affected by increased static stability.

32
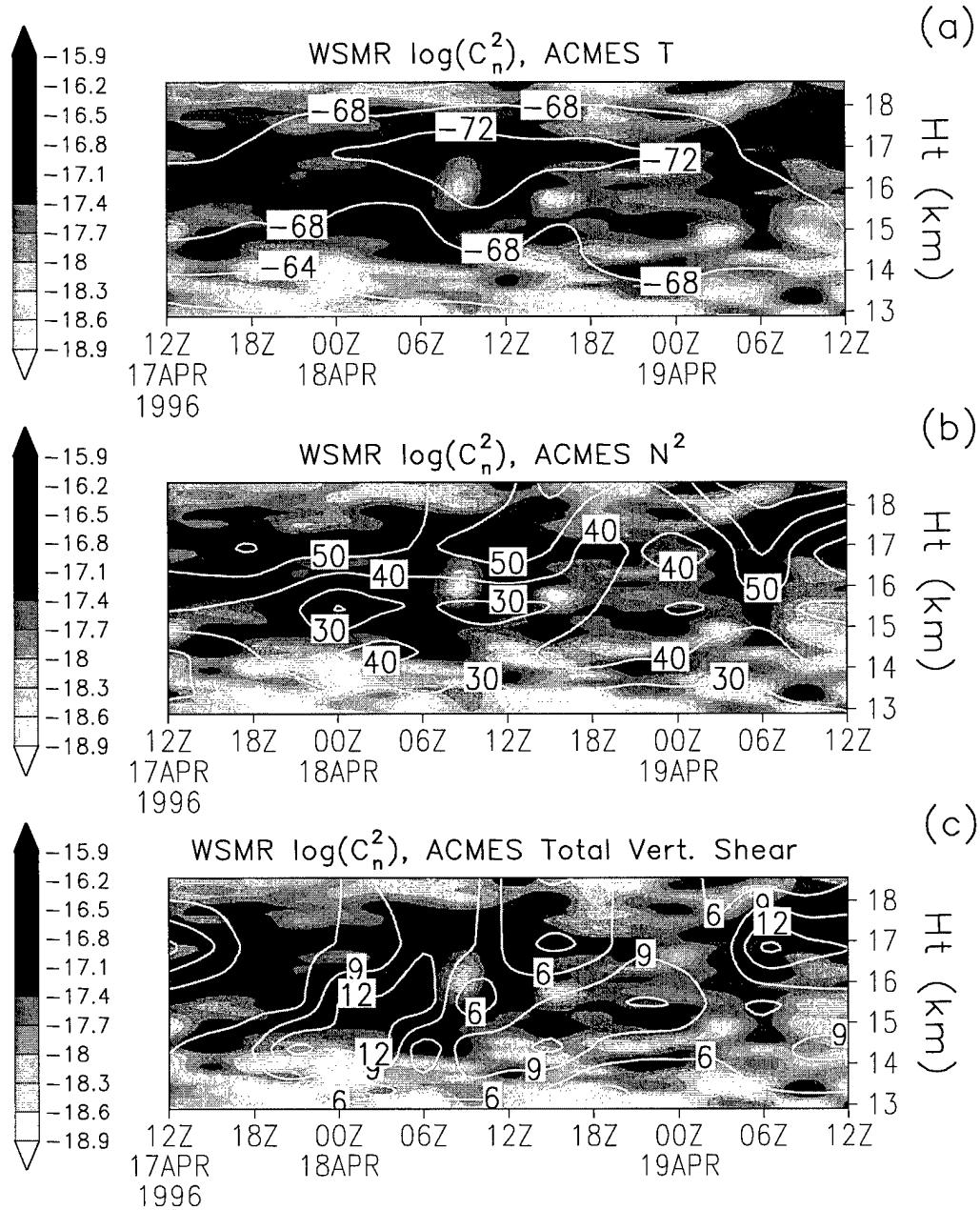
Figure 14   Case study 1 upper-level WSMR $\log(C_n^2)$ and ACMES data. (a) High $\log(C_n^2)$ occurs under the inversion. Temperature (°C) is contoured. (b) Under the inversion, high $\log(C_n^2)$ occurs where Brunt-Väisälä frequency squared is low.   Brunt-Väisälä frequency squared $(1/s^2)$, contoured, is multiplied by 10^5. (c) Total vertical shear $(1/s)$ is multiplied by 10^4.
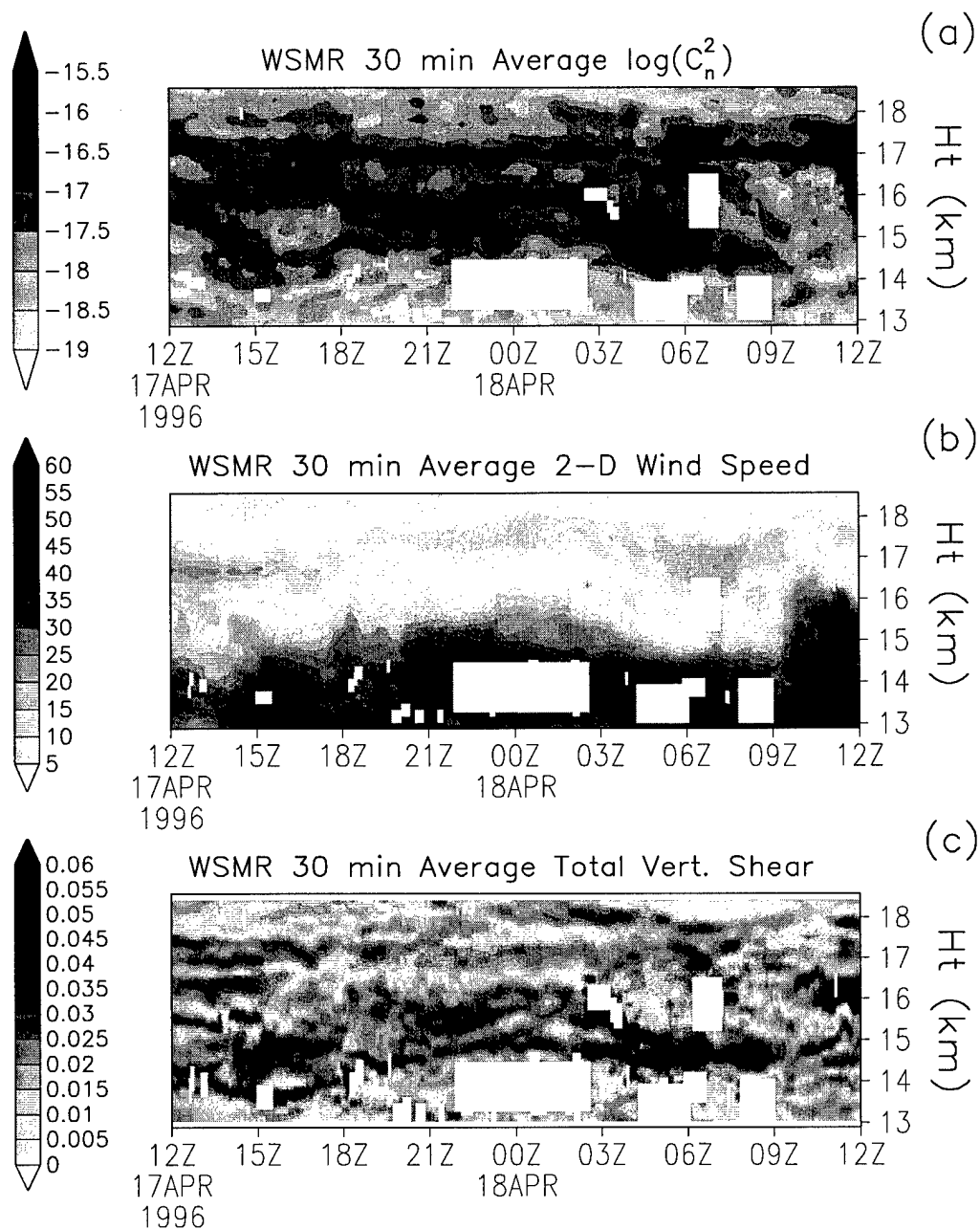
Figure 15   Case study 1 fine-scale WSMR radar data. (a) Radar $\log(C_n^2)$ data are averaged in 30 minute intervals every 3 minutes. Two $\log(C_n^2)$ bands appear. (b) The lower band at 15 km resides atop a region of high radar measured wind speeds (m/s). (c) The lower band of high $\log(C_n^2)$ is in a region of strong vertical shear (1/s). White blocks are missing data that have been quality controlled.
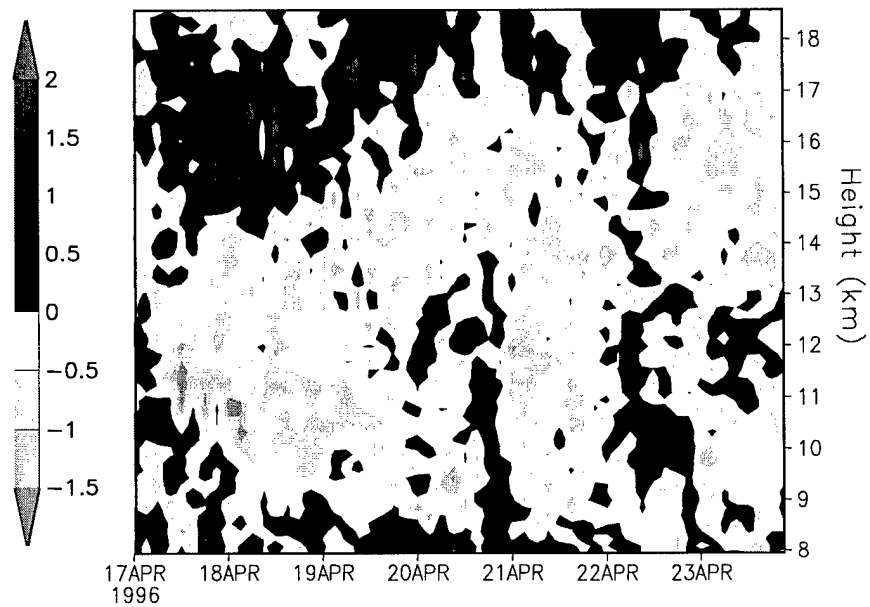
Figure 16   Case study 1 calculated $\log(P)$.   Values of $\log(P)$, calculated by subtracting ACMES $\log(M^2)$ data from the WSMR $\log(C_n^2)$ data, show higher values of P along the lower stratospheric boundary at about 18 km.   In the mid-tropopause, from 14 km to 16 km, P is typically less than 1 outside of mechanically turbulent areas.

Lastly, a few remarks about some other atmospheric variables and their correlation to $\log(C_n^2)$. Temperature and potential temperature correlate stronger with $\log(C_n^2)$ than they did in the lower levels, as seen in Figures 12 (c) and (d). Correlation coefficient values are around -0.5 from 15 km to 17 km, with peaks of about -0.6. The reason for this is that high values of C_n^2 reside just above the base of the stratospheric inversion in the coldest part of the inversion, and because high values of C_n^2 exist beneath the base of the inversion, also in a cold region, where mechanical turbulence seems to be increasing C_n^2. This is easily seen in Figure 9 from 15 km to 17 km. The relationship between temperature and C_n^2 seen in the mid-tropopause to lower stratosphere layer is likely not from a simple, intrinsic relationship between the two, but from general weather patterns associated with features in this layer.

5.1.4 Summary. For this case study, there is good linear dependence between $\log(C_n^2)$ and the log of potential refractivity squared in the lower levels from 8 km to 13 km. The relationship is best just above the average height of the jet core, with a correlation coefficient value of about 0.8. The relationship dwindles above 12 km. The series of high and low $\log(C_n^2)$ values at 12 km during the period of the case study can be explained with the thermal wind relationship. The position of the closest jet core with its associated vertical wind shears affects horizontal temperature gradients, which in turn affect potential refractivity and thus C_n^2. Synoptic-scale dynamics plays a strong and predictable role in affecting $\log(C_n^2)$ when a jet core is present in both time and space.

From the mid-tropopause to the lower stratosphere, high values of $\log(C_n^2)$ occur above the stratospheric inversion where potential refractivity increases because static stability increases in the stratosphere. High values of $\log(C_n^2)$ also occur beneath the stratospheric inversion where turbulent kinetic energy is available from strong vertical wind shears associated with the approach and departure of the polar jet. Potential refractivity alone is not enough to account for the higher $\log(C_n^2)$

values beneath the inversion. This is partly evidenced by the increased correlation of $\log(C_n^2)$ to total vertical shear in the upper levels.

5.2   Case Study 2

5.2.1   Overview.   Case study 2 is chosen for two banded features and a patch of high C_n^2 which appear in the data. Unlike the pattern of high and low $\log(C_n^2)$ values seen in case study 1, case study 2 has a fairly uniform band of $\log(C_n^2)$ between 9 km and 12 km. Figure 17 shows $\log(C_n^2)$ for this case study, which runs from 00 UTC 8 April 1996 to 00 UTC 15 April 1996. The other banded feature rises from 13 km to 18 km over the period. These bands are positioned similar to those in seen in case study 1. The remaining feature of interest is the patch of high $\log(C_n^2)$ centered at 15 km on 00 UTC 14 April, appearing underneath the upper level band.

Again looking at 200 hPa for a general overview of the synoptic situation, Figures 18 and 19 show that a jet core does not repeatedly pass over the WSMR radar as with case study 1. For the entire period of this case study, the WSMR radar lies between the subtropical jet to the south and the polar jet to the north, though at times they come close. This might affect the strength of linear dependence of $\log(C_n^2)$ with the log of potential refractivity squared.

Just as with case study 1, the lower band of high $\log(C_n^2)$ rests near a region of maximum wind speeds, as seen in Figure 20. In Figure 21 the upper band of high $\log(C_n^2)$ resides near the stratospheric inversion, similar to case study 1. Keeping the same height ranges used in the analysis of the first case study, the upper troposphere to lower tropopause region is discussed first.

5.2.2   Upper Troposphere to Lower Tropopause.   The lower band of high $\log(C_n^2)$ resides at the lower tropopause boundary where static stability, and thus potential refractivity, generally increases. Correlation coefficients of $\log(C_n^2)$ with the log of potential refractivity squared are shown in Figure 22 (a). Typical values
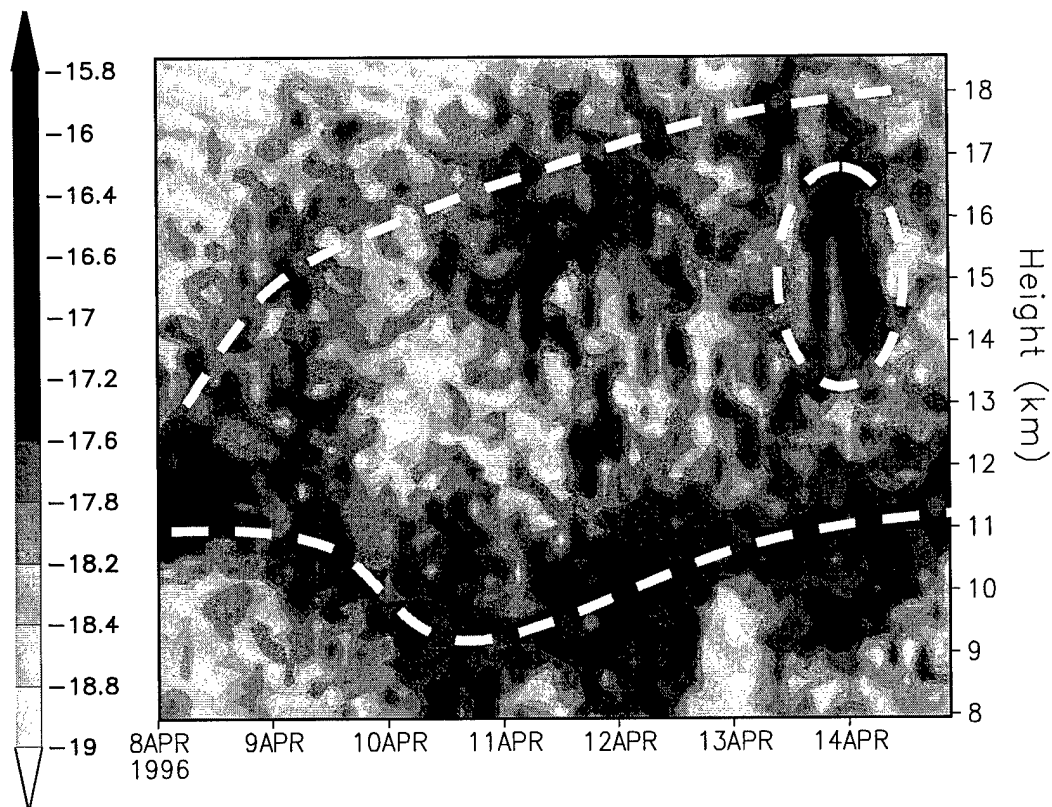
Figure 17   Case study 2 WSMR $\log(C_n^2)$.   Significant features in this case study are denoted by dashed line: the high $\log(C_n^2)$ band between 9 km and 12 km, the upper band of high $\log(C_n^2)$ from 13 km to 18 km, and the high $\log(C_n^2)$ centered at 15 km on 00 UTC 14 April 1996.
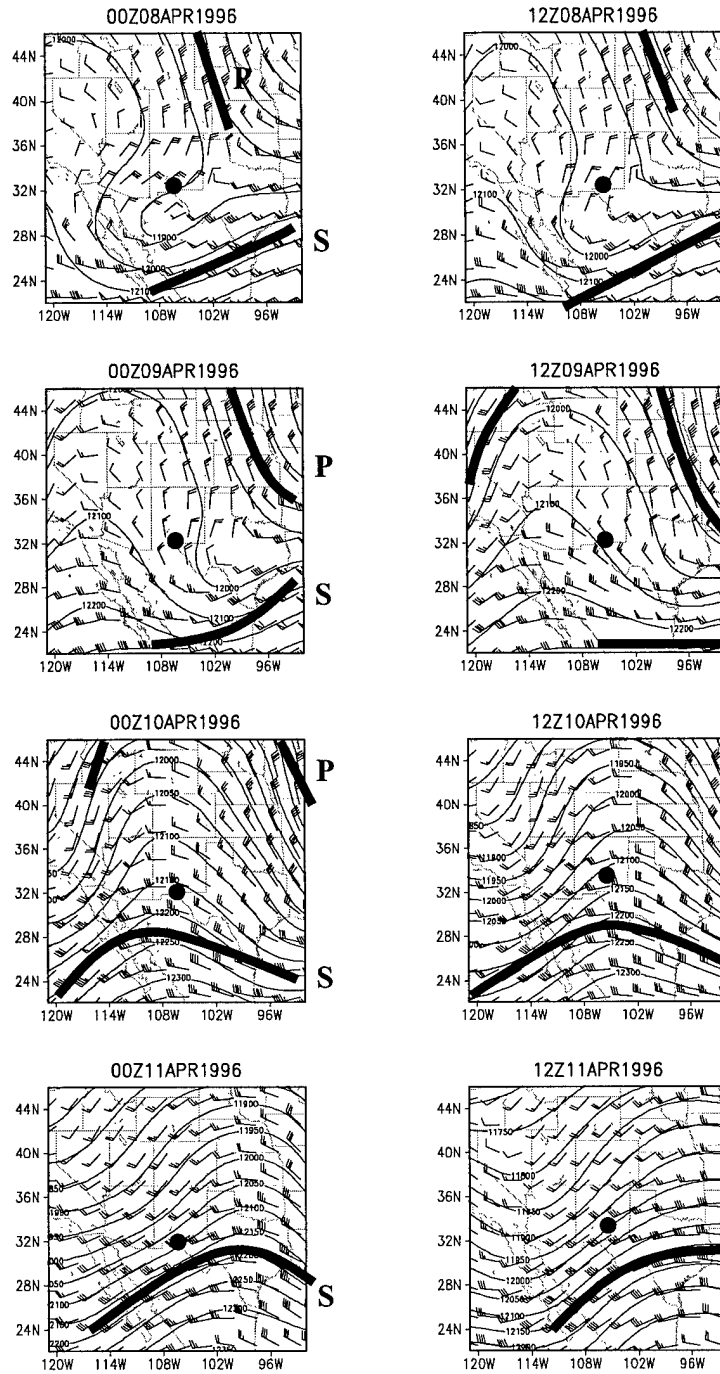
Figure 18   Case study 2 NCEP/NCAR 200 hPa analysis.   The polar (P) and subtropical (S) jet cores are denoted by solid line and the WSMR radar by dot.   Geopotential height is in meters MSL and wind barbs are in meters per second.
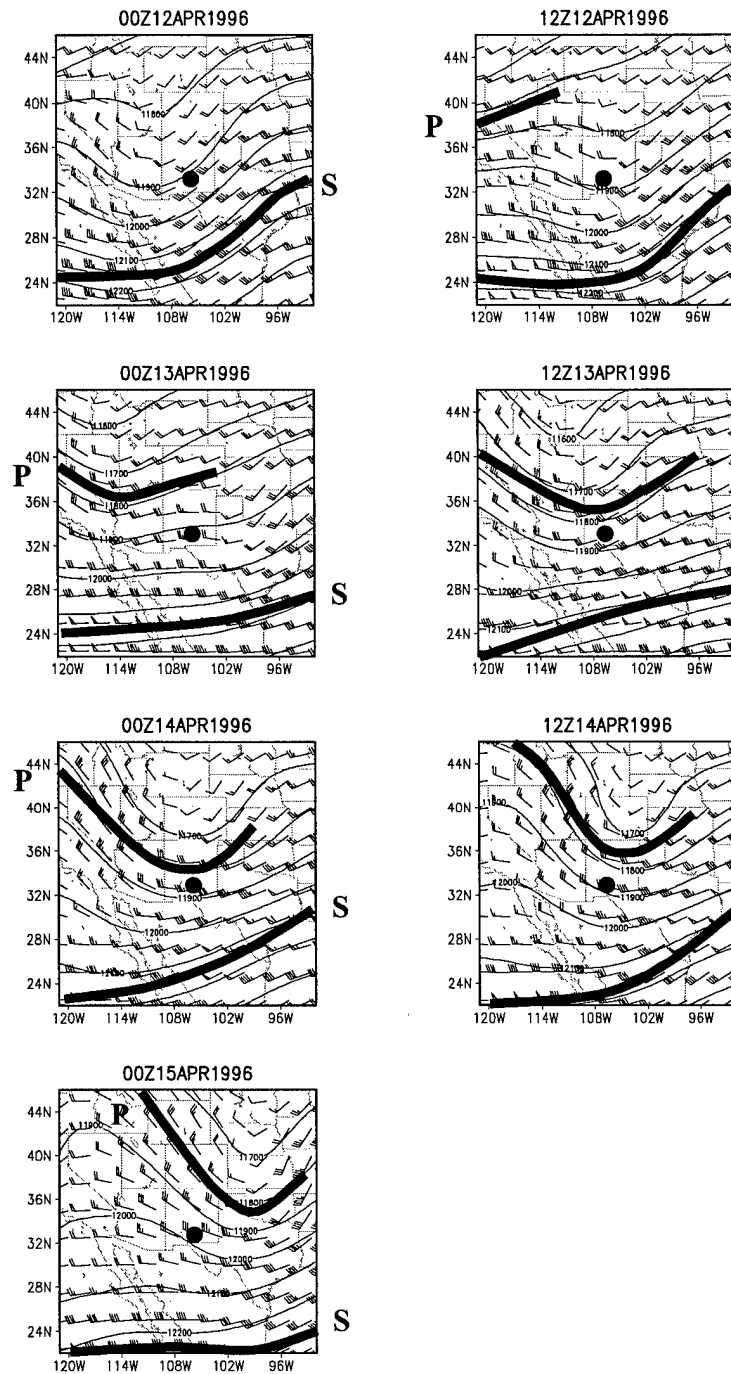
Figure 19   Case study 2 NCEP/NCAR 200 hPa analysis.   The polar (P) and
subtropical (S) jet cores are denoted by solid line and the WSMR radar
by dot.   Geopotential height is in meters MSL and wind barbs are in
meters per second.
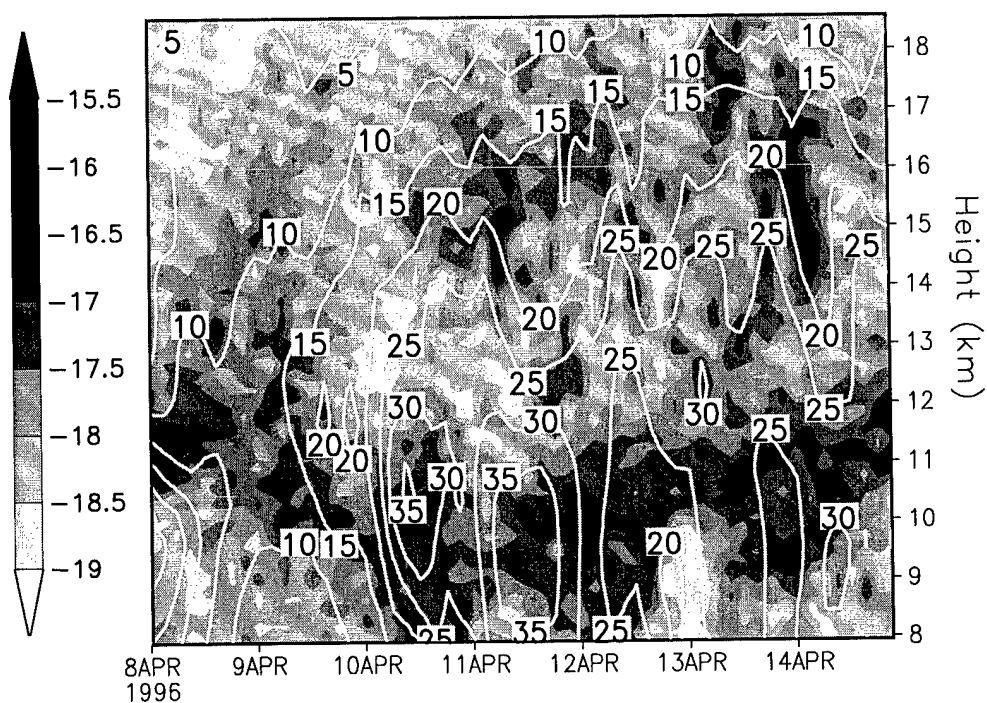
Figure 20   Case study 2 WSMR $\log(C_n^2)$ and ACMES 2-D horizontal wind speed (m/s).
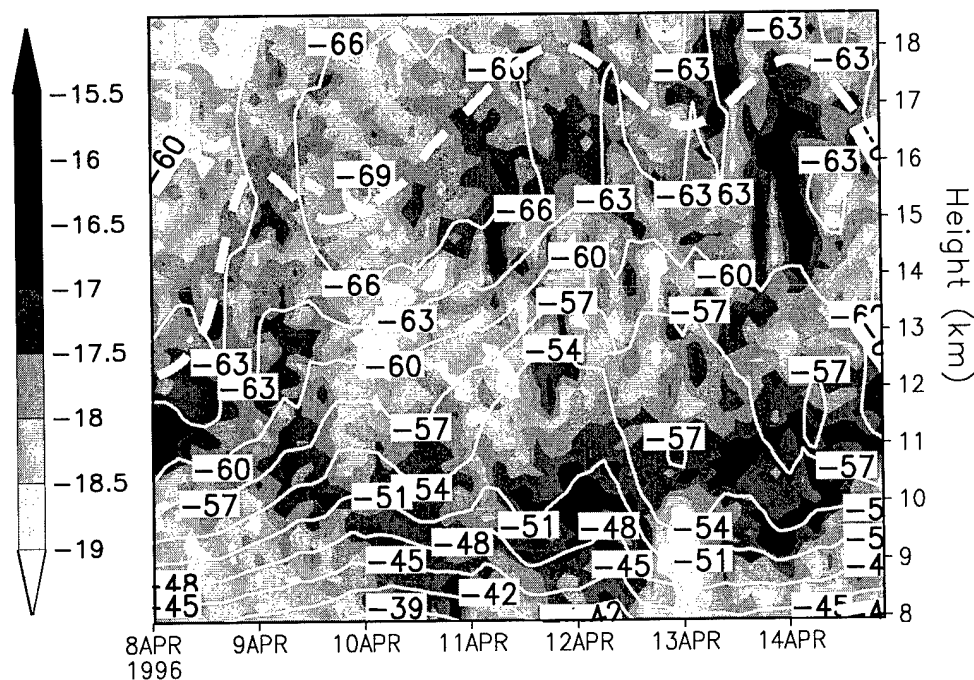
Figure 21   Case study 2 WSMR $\log(C_n^2)$ and ACMES temperature (°C). The base of the stratospheric inversion is denoted by dashed line.

41

in this layer are just under 0.4, with a minimum value close to 0 and a maximum of 0.6. The linear dependence of $\log(C_n^2)$ with $\log(M^2)$ is weaker between the polar and subtropical jets. In case study 1, the linear dependence was higher, but proximity to the polar jet during that case study was closer and for longer periods of time. A similar pattern with correlation coefficients occurs with the Brunt-Väisälä frequency squared, seen in Figure 22 (b).

An interesting pattern occurs with the correlation coefficients of $\log(C_n^2)$ with temperature. In Figure 23 (c) the coefficients underneath 10.5 km are positive with values of about 0.5, and above they are negative values of about -0.5. The reason for this is a patch of higher temperatures north of the subtropical jet sweeping across New Mexico during the case study. This is seen in Figure 24. As the upper-level warm air passes through New Mexico from 00 UTC 11 April 1996 to 12 UTC 12 April 1996 at the 200 hPa level, the lower tropopause boundary drops and C_n^2 is less than in the high C_n^2 band associated with the boundary. The pattern in the correlation coefficients is not due to a simple, intrinsic relationship between C_n^2 and temperature alone. Correlation coefficients calculated at constant heights throughout the entire time period show this relationship as the lower tropopause boundary shifts with height and the upper-level warm air shifts with the passage of the subtropical jet. This is more easily seen with the realizations of $\log(C_n^2)$ and temperature in Figures 25 (c) and (d). A similar pattern with correlation coefficients occurs with the zonal and meridional components of wind, seen in Figures 23 (a) and (b). Most likely the proximity of the jets and the dynamics associated with winds and temperatures are the reasons for these patterns.

5.2.3 Mid-Tropopause to Lower Stratosphere. In this layer the linear dependence of $\log(C_n^2)$ with the log of potential refractivity squared is very weak, as seen in Figure 22 (a). This is similar to case study 1. Unlike case study 1 though, the relationship between $\log(C_n^2)$ and temperature disappears. The correlation coefficients are mostly between -0.2 and 0.2 for all heights, seen in Figure 23 (c). However,

42
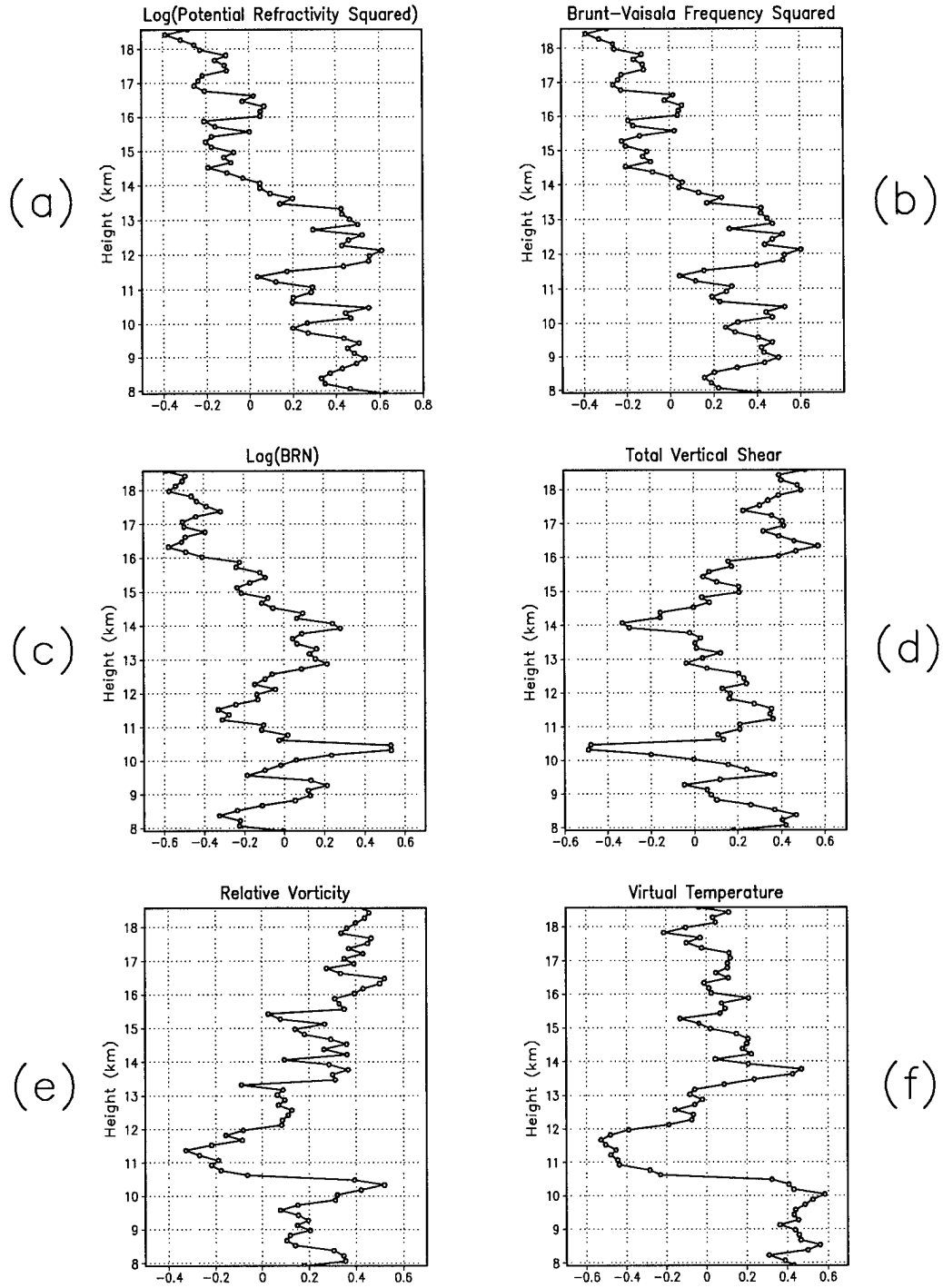
Figure 22   Case study 2 correlation coefficients of lag 0. Coefficients are computed at constant height between WSMR $\log(C_n^2)$ and variables at top of each graph.
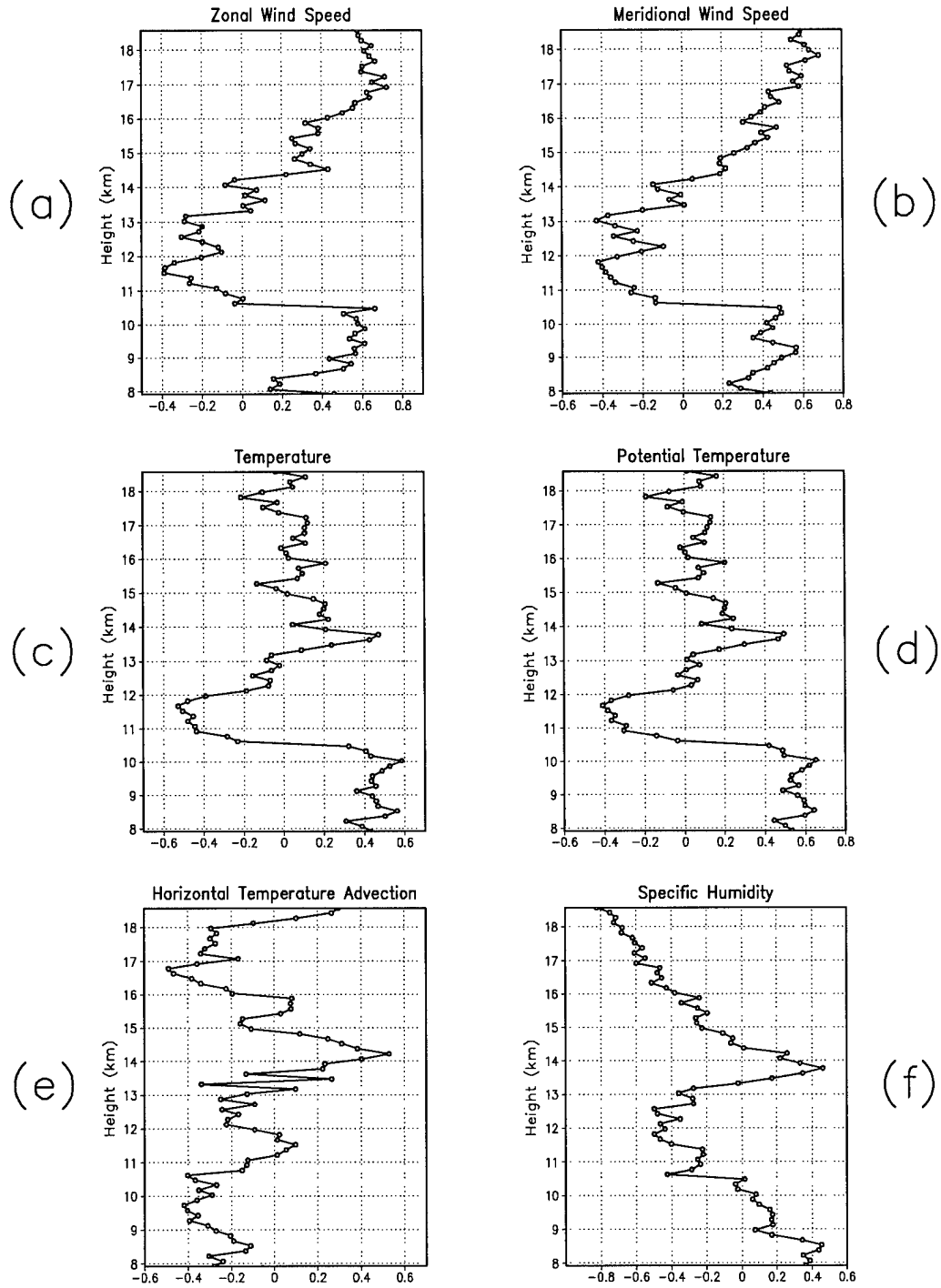
Figure 23   Case study 2 correlation coefficients of lag 0. Coefficients are computed at constant height between WSMR $\log(C_n^2)$ and variables at top of each graph.
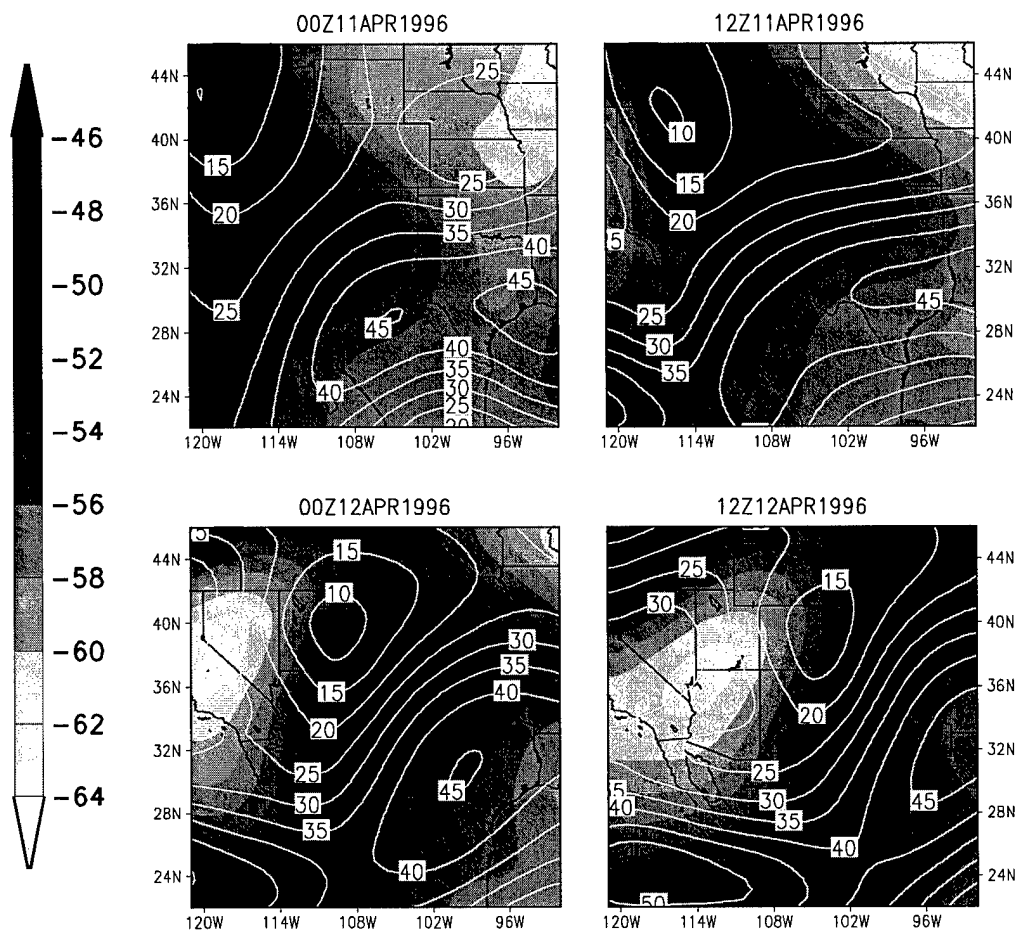
Figure 24   Case study 2 NCEP/NCAR 200 hPa temperature analysis. Temperatures (°C), shaded, are shown from 00 UTC 11 April 1996 to 12 UTC 12 April 1996. 2-D wind speeds (m/s) are contoured. The four panels show the passage of warm air, north of the subtropical jet.

45
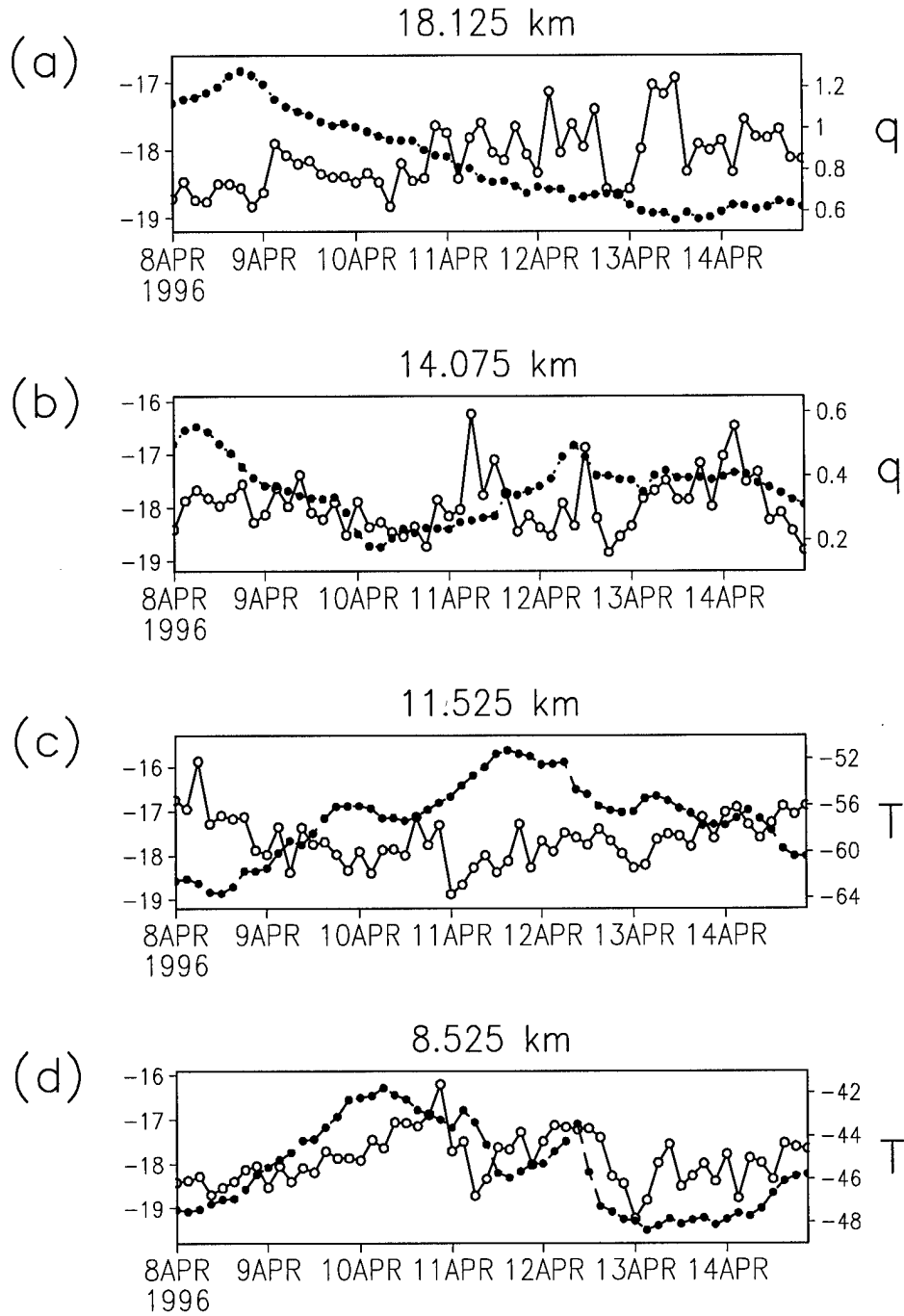
Figure 25   Case study 2 realizations of WSMR $\log(C_n^2)$ and ACMES specific humidity and temperature.   (a) and (b)   Specific humidity (kg/kg) is multiplied by 10^6 and denoted with black circles.   (c) and (d)   Temperature (°C) is denoted with black circles.   (a) through (d) show the relationship between variables at different heights and how those relationships affect correlation coefficients. $\log(C_n^2)$ is represented by white, open circles in all plots.

46
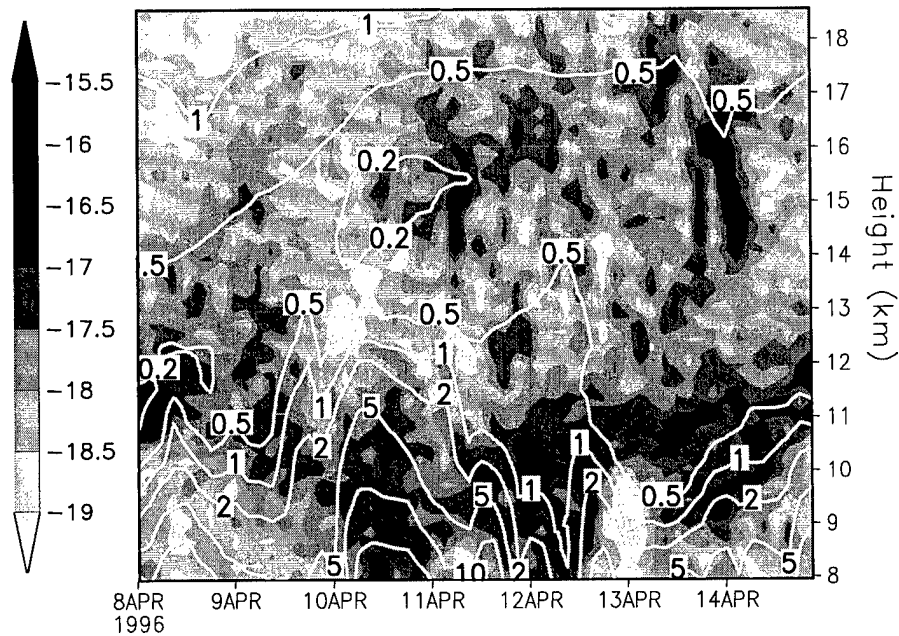
Figure 26   Case study 2 WSMR $\log(C_n^2)$ and ACMES specific humidity.   Specific
humidity (kg/kg) is multiplied by 10^6.   Specific humidity is higher in
the lower stratosphere compared to the upper tropopause.

with this case study a much stronger linear relationship exists between $\log(C_n^2)$ and
the zonal component of wind, with values exceeding 0.7 near 17 km.   This can be
seen in Figure 23 (a).   This relationship and the relationship between $\log(C_n^2)$ and
specific humidity, seen in Figure 23 (f), might be due to the proximity of jets (and
thus the stratosphere in this layer) and the dynamics and general features seen with
them.   For instance, in this case study the stratospheric air is more humid than the
air along the upper tropopause boundary, as seen in Figure 26.   One would expect
high C_n^2 associated with low specific humidity, thus a negative correlation coefficient
in the upper levels.   This is more easily seen in the realizations shown in Figures
25 (a) and (b).   Again, these patterns in the correlation coefficients with height are
probably not due to simple, intrinsic relationships between the variables; but rather
to dynamics and general weather patterns associated with features in this layer.

The patch of high $\log(C_n^2)$ centered at 15 km on 00 UTC 14 April 1996 rests
underneath the stratospheric inversion.   Just as with case study 1, this patch of

47

high $\log(C_n^2)$ occurs during the approach of the polar jet. The patch of high $\log(C_n^2)$ can be seen more closely in Figure 27 (a). As with the high $\log(C_n^2)$ seen under the stratospheric inversion in case study 1, the log of potential refractivity squared does not seem to account for this pattern. In Figure 28, high values of $\log(C_n^2)$ occasionally occur in weak $\log(M^2)$ regions, compared to lower $\log(C_n^2)$ regions with higher $\log(M^2)$. It is likely the parameters embedded in P, where $C_n^2 = PM^2$, are different in these regions. To look at what could affect P, the potential for mechanical turbulence is looked at.

Looking at the total variance of horizontal wind speed as potential indicator of mechanical turbulence, Figures 27 (a) and (b) show that the high $\log(C_n^2)$ patch occurs exactly where there is high variance in the radar measured wind speeds. Possible sources for this mechanical turbulence could be from shear, which provides energy for turbulent activity, or from gravity wave activity.

Looking first at shear, Figure 19 shows the polar jet had been moving towards WSMR steadily since 00 UTC 13 April to 00 UTC 14 April, whereafter it moved off to the northeast. Passage of a trough occurs during these times. Figures 27 (b) and (c) show that the high variance regions occur above the region of high horizontal wind speed. The high variance regions also occur above and underneath regions of maximum ACMES total vertical shear, not in regions of maximum total vertical shear. Also, the high variance does not occur just in low Brunt-Väisälä frequency squared regions. The high variance regions do not occur mostly in regions with the lowest buoyant Richardson number, where one would think there would be the greatest possibility of mechanical turbulence. But again looking at fine-scale radar data, Figure 29 shows the high $\log(C_n^2)$ patch occurring above a region of high radar measured wind speeds. The high $\log(C_n^2)$ patch corresponds exactly where there is high total vertical shear, Figure 29 (c), calculated from the radar measured wind speeds. As with case study 1, C_n^2 is likely higher in this region from mechanical
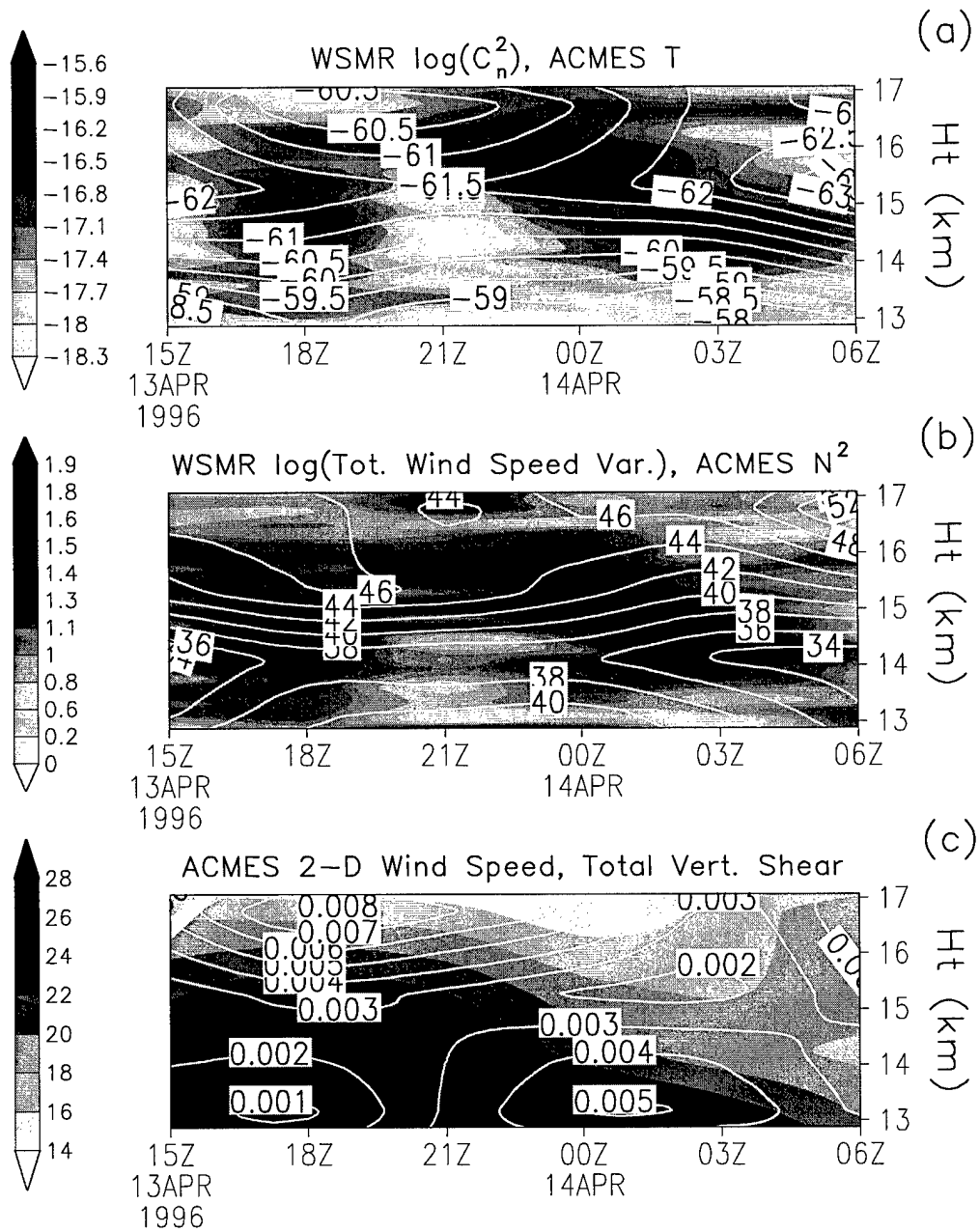
Figure 27   Case study 2 upper-level WSMR $\log(C_n^2)$ and ACMES data. (a) High $\log(C_n^2)$ occurs under the inversion. Temperature (°C) is contoured. (b) High log of total wind speed variance, shaded, occurs at the same heights and times as high $\log(C_n^2)$. Brunt-Väisälä frequency squared $(1/s^2)$, countoured, is multiplied by 10^5. (c) Horizontal wind speed (m/s) is shaded.

49
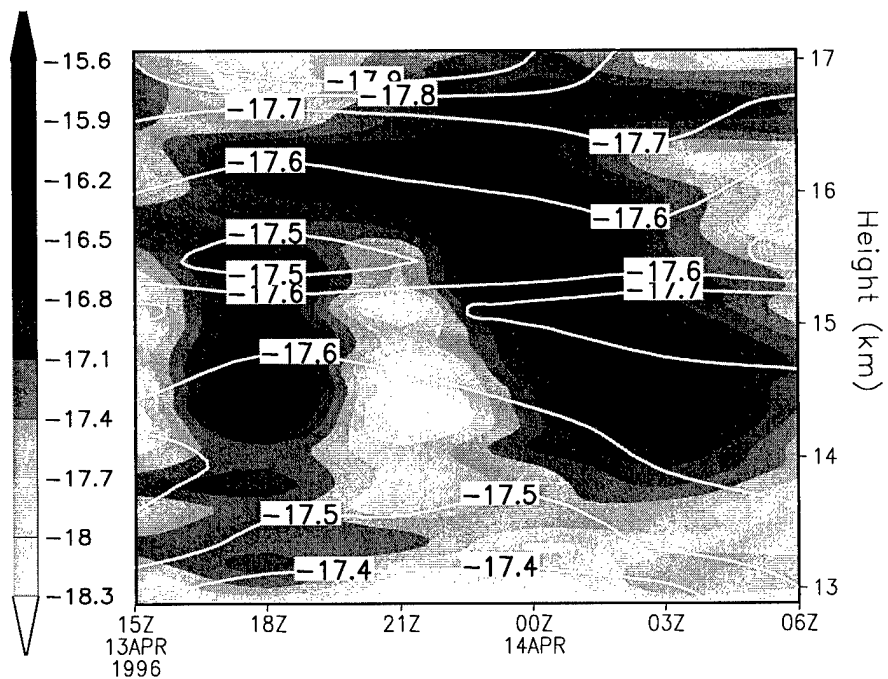
Figure 28   Case study 2 WSMR $\log(C_n^2)$ and ACMES log of potential refractivity squared, M^2.   High values of $\log(C_n^2)$, shaded, occasionally occur in weak $\log(M^2)$ regions, contoured, compared to lower $\log(C_n^2)$ regions with higher $\log(M^2)$.

turbulence, the source of which is turbulent kinetic energy available from strong vertical wind shears associated with the approach and departure of the polar jet.

Gravity wave activity could also be a source of mechanical turbulence in this region where the high total variance of wind speed occurs. Gravity waves might be transporting energy from one region of the atmosphere to this region of high wind speed variance, increasing the amount of turbulent kinetic energy in the region, enhancing C_n^2. Appendix C briefly shows how the transport of kinetic energy is related to turbulent kinetic energy production.

Nastrom and Eaton (9:85) found WSMR radar wind speeds at 5.6 km correlated well with increased turbulence above the troposphere. They concluded that the increased turbulence seen was result of gravity wave activity in the troposphere associated with troughs. Different from their study, correlation coefficients between $\log(C_n^2)$ at all heights and the ACMES horizontal wind speed only at 5.675 km are calculated and shown in Figure 30. Not much of a difference exists between the values in this figure and the correlation coefficients separately calculated between the zonal and meridional components and $\log(C_n^2)$, which coefficients were always calculated at the same height. The approach of the polar jet around 00 UTC 14 April 1996 and gravity wave activity might be a source of the mechanical turbulence seen underneath the stratospheric inversion. Figure 31 shows radar zonal wind speed averaged about 30 minute intervals near 12 km from 15 UTC 13 April 1996 to 06 UTC 14 April 1996. The modulated speeds seen in the figure could be showing gravity waves within the curved, cyclonic flow of the jet. Gravity waves propagating upward from this region might be transporting kinetic energy upwards, providing turbulent kinetic energy aloft where the variance of wind speeds is high, enhancing C_n^2. These gravity waves might be internal gravity waves associated with the polar jet, or they might be externally forced waves originating at the surface as wind flows over terrain. Figure 32 shows 2-dimensional wind speeds, on a constant pressure surface, close to the surface at 00 UTC 14 April 1996. The flow is strong and per-
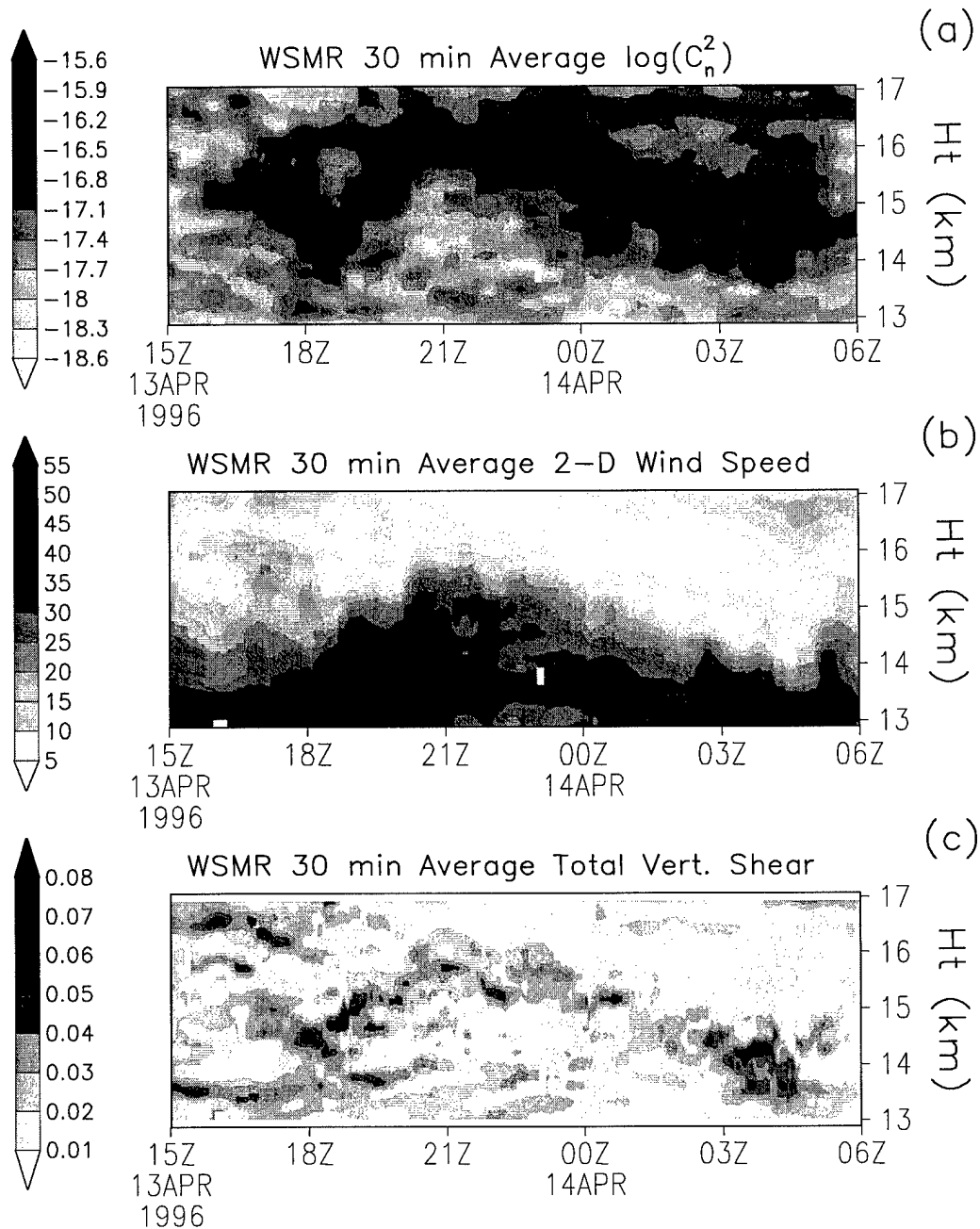
Figure 29   Case study 2 fine-scale WSMR radar data.   (a)   Radar $\log(C_n^2)$ data are averaged in 30 minute intervals every 3 minutes.   (b) The band of high $\log(C_n^2)$ resides atop a region of high radar measured wind speeds (m/s).   (c)   The band of high $\log(C_n^2)$ is in a region of strong vertical shear.   White blocks are missing data that have been quality controlled.
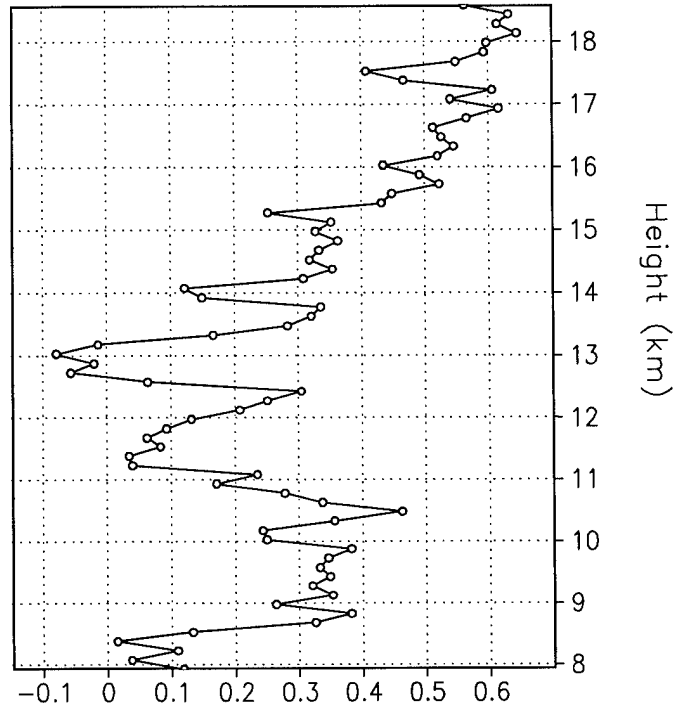
Figure 30   Case study 2 correlation coefficients between WSMR $\log(C_n^2)$ at each height and ACMES 2-D horizontal wind speeds only at 5.675 km.

pendicular to the terrain, which is favorable for terrain-induced gravity waves. A detailed description of gravity waves is covered in Appendix D.

As with case study 1, values of $\log(P)$ are calculated from the ACMES and WSMR data. Figure 33 shows several features. A more uniform band of P values resides along the lower tropopause boundary between 9 km and 12 km. Values of P are typically greater than 1. Along the lower stratosphere boundary from 11 April through 14 April 1996, values of P are also greater than 1. Before 11 April, the vertical gradient of temperature is weak, making for a less well-defined stratospheric boundary. Perhaps this is why P values are lower before 11 April along the boundary. Between the two boundaries in the mid-tropopause, P is usually less than 1, outside of mechanically turbulent areas. The patch of high $\log(C_n^2)$ on 00 UTC 14 April 1996, centered at 15 km, has values of P much greater than 1. Again, mechanical turbulence and an increased amount of turbulent kinetic energy available
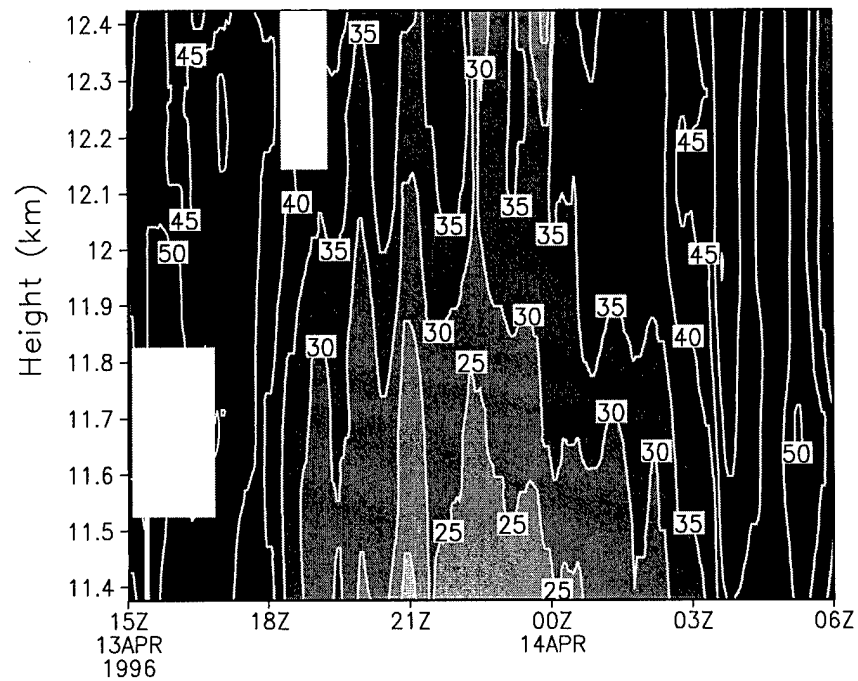
Figure 31   Case study 2 WSMR 30 min average zonal wind speed (m/s).   Zonal
wind speed measured every three minutes by the WSMR radar is aver-
aged about 30 minute intervals.   Wave patterns appear in the speeds
underneath the region of maximum wind speeds for a depth of over 1
km.   White blocks are missing data that have been quality controlled.
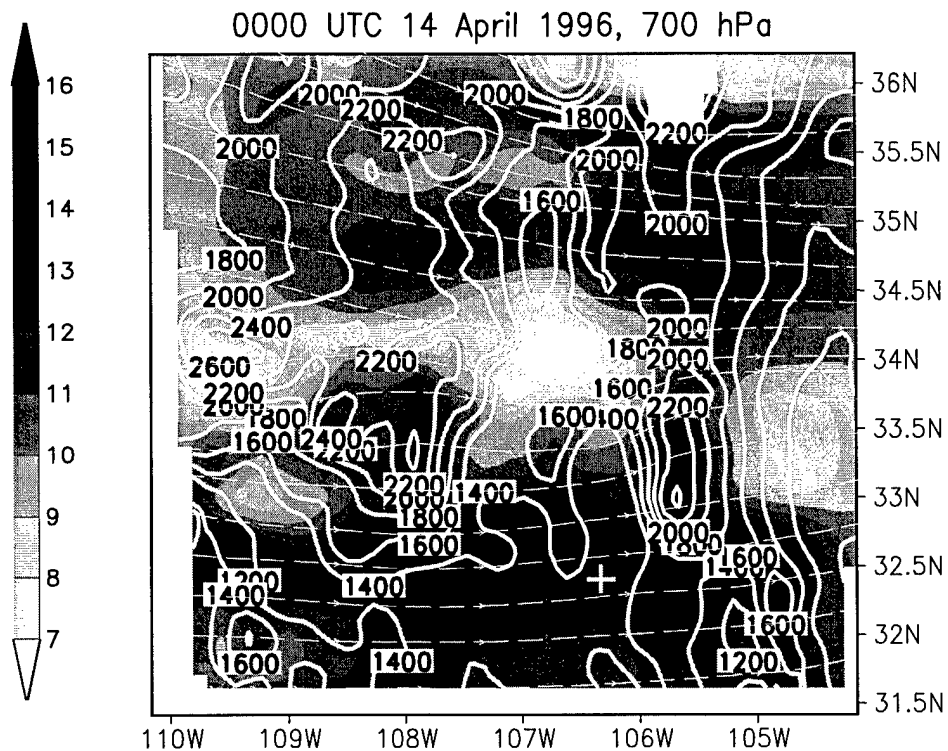
Figure 32 Case study 2 ACMES 2-D wind speeds at 700 hPa.   Wind speeds
(m/s) are shaded.   Streamlines of flow are thin dashed lines.   Flow is
perpendicular to the terrain near the WSMR radar, denoted by a white
cross at 32°24'N, 106°21'W. Surface terrain (m) above mean sea level
is contoured.   The white block at 36°N is where the 700 hPa surface
intersects the terrain.
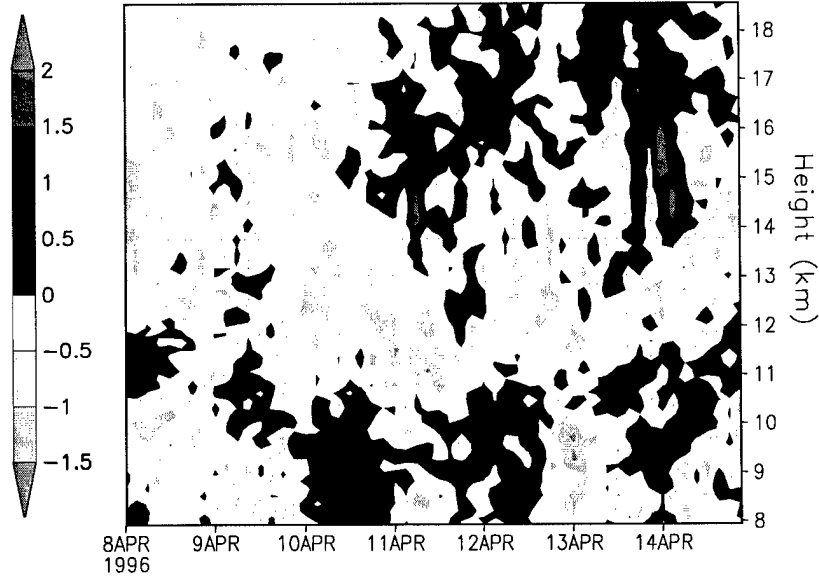
Figure 33   Case study 2 calculated $\log(P)$.   Values of $\log(P)$ are calculated by subtracting ACMES $\log(M^2)$ data from the WSMR $\log(C_n^2)$ data.

for cascade through the inertial subrange might make for higher values of P, and thus C_n^2.

5.2.4   Summary.   Case study 2 occurs between the polar and subtropical jets. Patterns in several of the correlation coefficients occur which are most likely from association with the dynamics of the atmosphere and typical weather patterns, rather than simple, intrinsic relationships to C_n^2.   Other variables correlate in a similar fashion to case study 1. The log of potential refractivity squared correlates well at the lower tropopause boundary, but not so well in the mid-tropopause and lower stratosphere.

The approach and departure of the polar jet and its associated strong vertical wind shears are a likely source of turbulent kinetic energy which increases C_n^2 underneath the stratospheric inversion. Gravity wave activity might also be a source of turbulent kinetic energy, seen in the increased variance of radar measured wind speeds under the stratospheric inversion. Internal gravity waves in the curved, cyclonic flow of the polar jet might be propagating kinetic energy upwards to where

the variance of wind speeds is high, enhancing C_n^2. Externally forced gravity waves originating at the surface might also be a source of mechanical turbulence, enhancing C_n^2.

5.3 Case Study 3

5.3.1 Overview.
Synoptically this case study is similar to case study 2. The polar jet remains to the north of the WSMR radar during this case study, though it comes very close on 00 UTC 29 April 1996. The subtropical jet remains well to the south of WSMR, seen in Figures 34 and 35.

The interesting features in the radar C_n^2 data can be seen in Figure 36. Two banded C_n^2 features appear at roughly 12 km and 17 km, just as with the other case studies. The upper band occurs near the stratospheric inversion, seen in Figure 37, while the lower band occurs at the lower tropopause boundary. A few patches of high $\log(C_n^2)$ appear on 25 April and 28 April. The patch of high $\log(C_n^2)$ on 25 April is significant as it seems to be affecting the correlation of $\log(C_n^2)$ with the log of potential refractivity squared in a way which is opposite to that seen in the previous two case studies.

5.3.2 Upper Troposphere to Lower Tropopause.
Unlike the positive correlation of $\log(C_n^2)$ with the log of potential refractivity squared seen in the upper troposphere to lower tropopause in the first two case studies, the correlation coefficients from 8 km to 10 km are negative, with a minimum value of about -0.4 at 9 km, seen in Figure 38 (a). The high $\log(C_n^2)$ on 25 April is centered at 9 km and this high $\log(C_n^2)$ at this height is affecting the correlation coefficients to $\log(M^2)$. Figure 39 (c) shows that $\log(C_n^2)$ is high on 25 April and decreasing, but the log of potential refractivity is low and increasing. This affects the overall correlation between the two variables over the entire period at this height. High variance of radar measured wind speeds corresponds to this region of high $\log(C_n^2)$. Figures 40
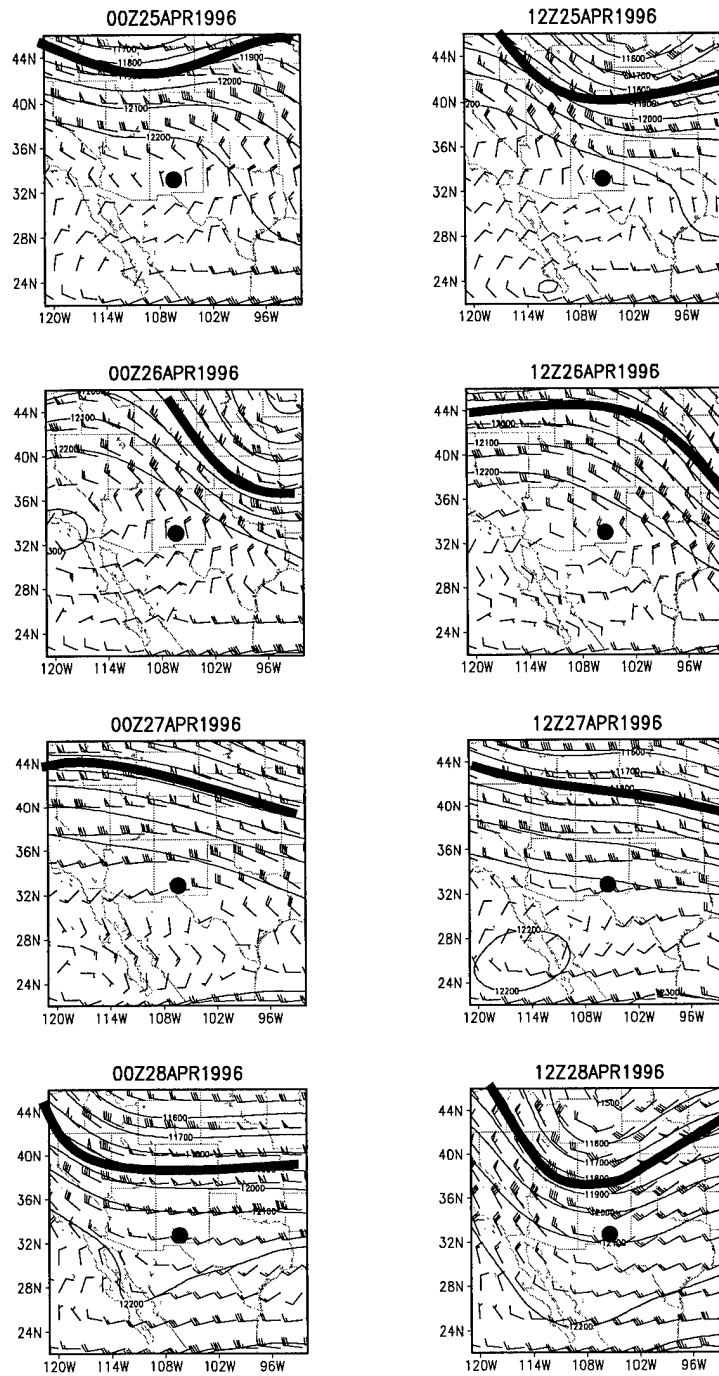
Figure 34   Case study 3 NCEP/NCAR 200 hPa analysis.   The polar jet core is
denoted by solid line and the WSMR radar by dot. Geopotential height
is in meters MSL and wind barbs are in meters per second.
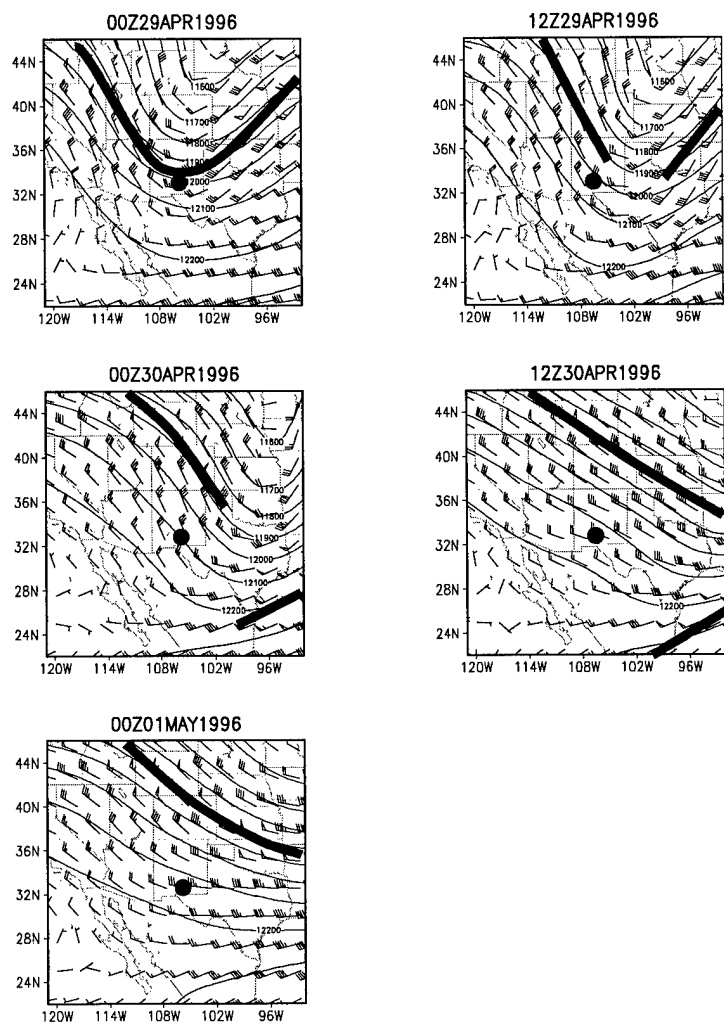
Figure 35   Case study 3 NCEP/NCAR 200 hPa analysis.   The polar jet core is
denoted by solid line and the WSMR radar by dot. Geopotential height
is in meters MSL and wind barbs are in meters per second.
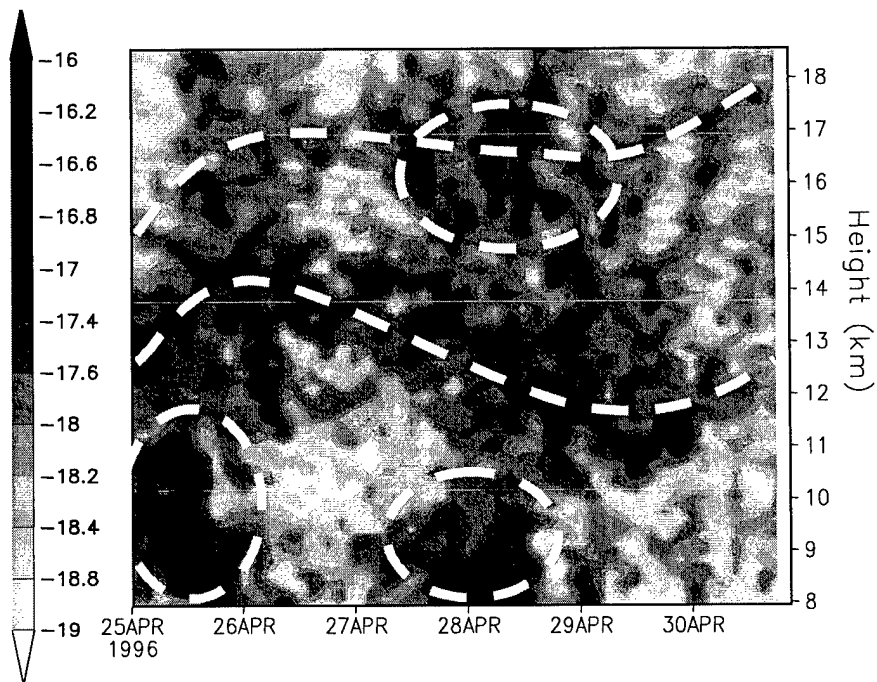
Figure 36   Case study 3 WSMR $\log(C_n^2)$.   Significant features in this case study are denoted by dashed line: the high $\log(C_n^2)$ band at roughly 12 km, the upper band of high $\log(C_n^2)$ at roughly 17 km, and the patches of high $\log(C_n^2)$ appearing on 25 April and 28 April 1996.
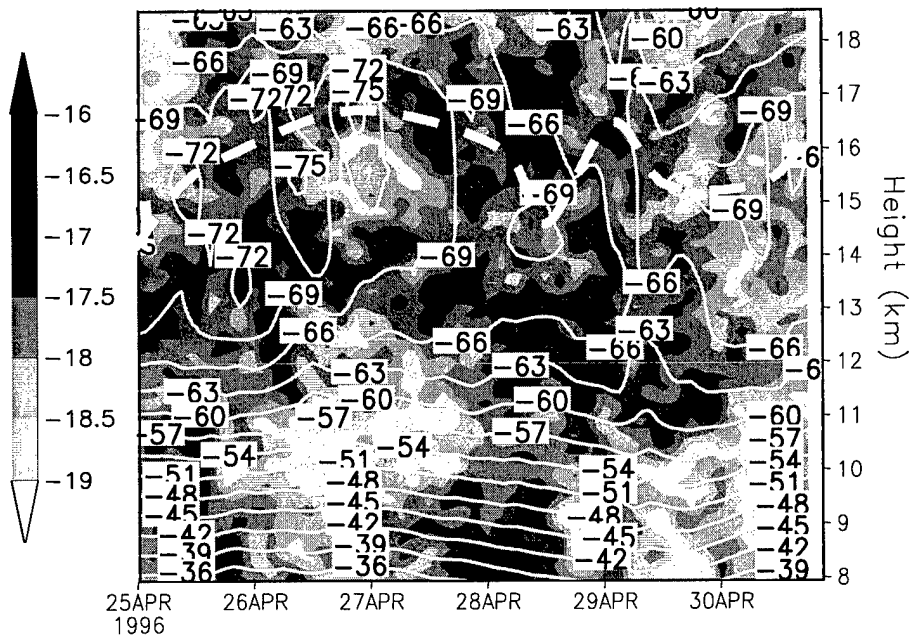
Figure 37   Case study 3 WSMR $\log(C_n^2)$ and ACMES temperature (°C).   The base of the stratospheric inversion is denoted by dashed line.

(a) and (b) show the general overlap of C_n^2 and high total variance of wind speeds beneath 11 km from 03 UTC to 15 UTC on 25 April. The possibility of mechanical turbulence, seen in the high variance of radar measured wind speeds, is a likely reason for increased $\log(C_n^2)$ seen at 9 km on 25 April, off-setting the correlation of $\log(C_n^2)$ to the log of potential refractivity squared at this level.

The high C_n^2 and high variance of wind speeds on 25 April 1996 occurs in a region of sporadically high total vertical wind shear, calculated from the radar measured wind speeds, seen in Figure 40 (c) from 03 UTC to 15 UTC between 8 km and 10 km. The ACMES total vertical shear, seen in Figure 40 (b) for the same times and heights, shows lower total shear values. The actual shear observed by the radar might be a source of turbulent kinetic energy which is increasing C_n^2 in the region. Another possible source of mechanical turbulence could be from the passage of a trough.

From 00 UTC 25 April 1996 through 00 UTC 26 April, the polar jet core does approach and depart New Mexico, seen in Figure 34. However, the jet core does not come close to WSMR at all. With the approach and departure of the polar jet, a trough does pass through WSMR during this time. Possibly turbulent behavior associated with the passage of the trough during this time could account for the high variance of radar measured wind speeds and high C_n^2 seen, as hypothesized by Nastrom and Eaton (9:86). It might be that the outer scale of turbulence changes, or the amount of kinetic energy available for cascade through the inertial subrange changes, during the passage of the trough, affecting the parameters P in $C_n^2 = PM^2$.

Patterns in the correlation coefficients between $\log(C_n^2)$ and other variables can be seen in Figure 41. Wind speeds, temperatures, and specific humidity patterns are likely a result of realizations of the variables at constant heights being affected by the movement of the lower tropopause boundary and the differences of these variables from troposphere to tropopause values. This argument is the same as that used for the patterns seen in the other two case studies.

Figure 38   Case study 3 correlation coefficients of lag 0. Coefficients are computed
at constant height between WSMR $\log(C_n^2)$ and variables at top of each
graph.
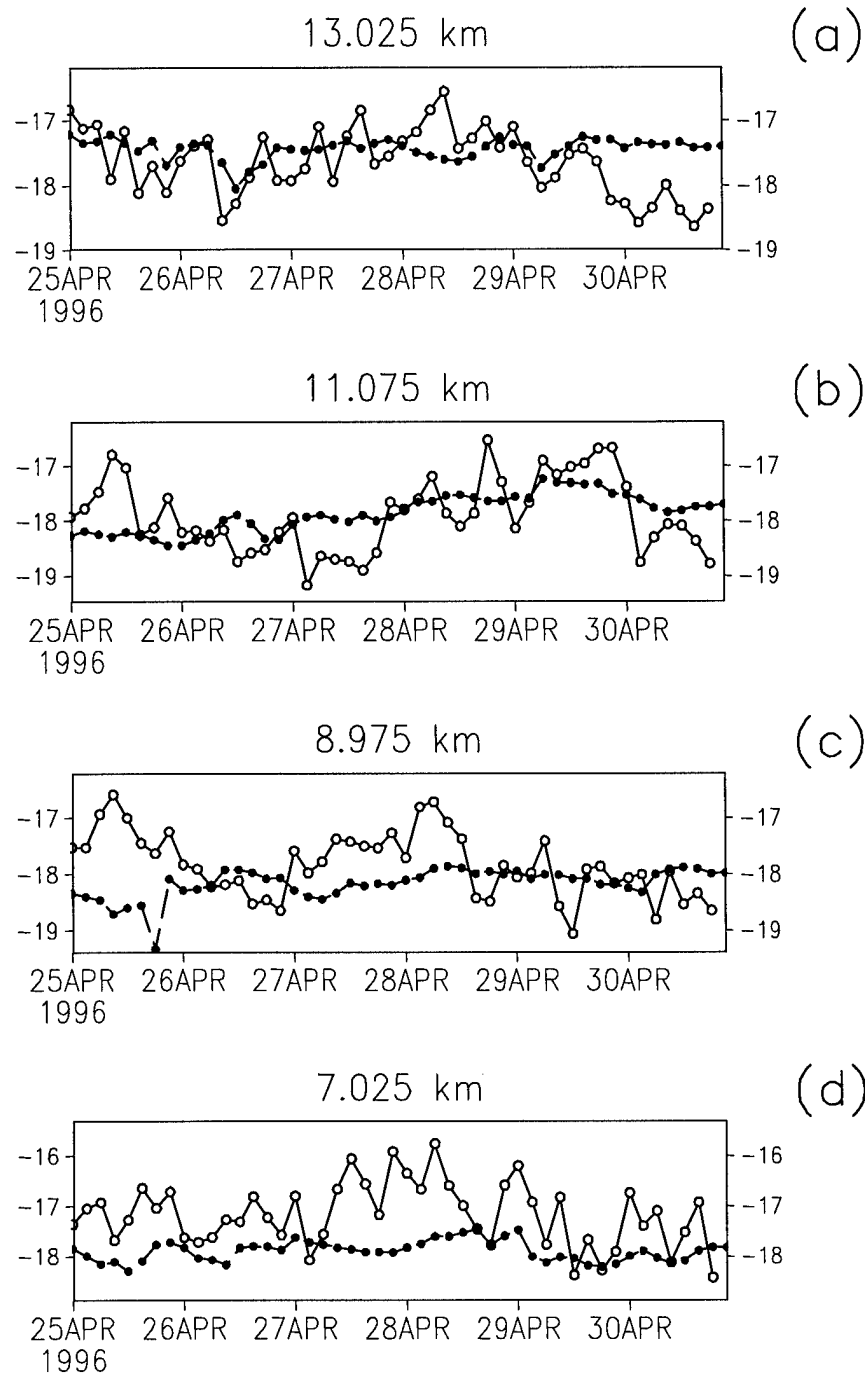
Figure 39   Case study 3 realizations of WSMR $\log(C_n^2)$ and the log of potential refractivity squared, M^2, at different heights.   (a) through (d) show the relationship between the two variables at different heights and how those relationships affect correlation coefficients. $\log(C_n^2)$ is denoted by white circles and $\log(M^2)$ by black circles.

Figure 40   Case study 3 lower-level WSMR and ACMES data from 25 April to 26 April 1996.   (a) The logarithm of potential refractivity squared is contoured.   (b) The logarithm of WSMR total wind speed variance, (m^2/s^2) is shaded.   ACMES total vertical shear (1/s) is multiplied by 10^4.   (c) WSMR radar total vertical shear (1/s) is shaded.   Brunt-Väisälä frequency squared $(1/s^2)$ is multiplied by 10^5.   White blocks are missing data that have been quality controlled.
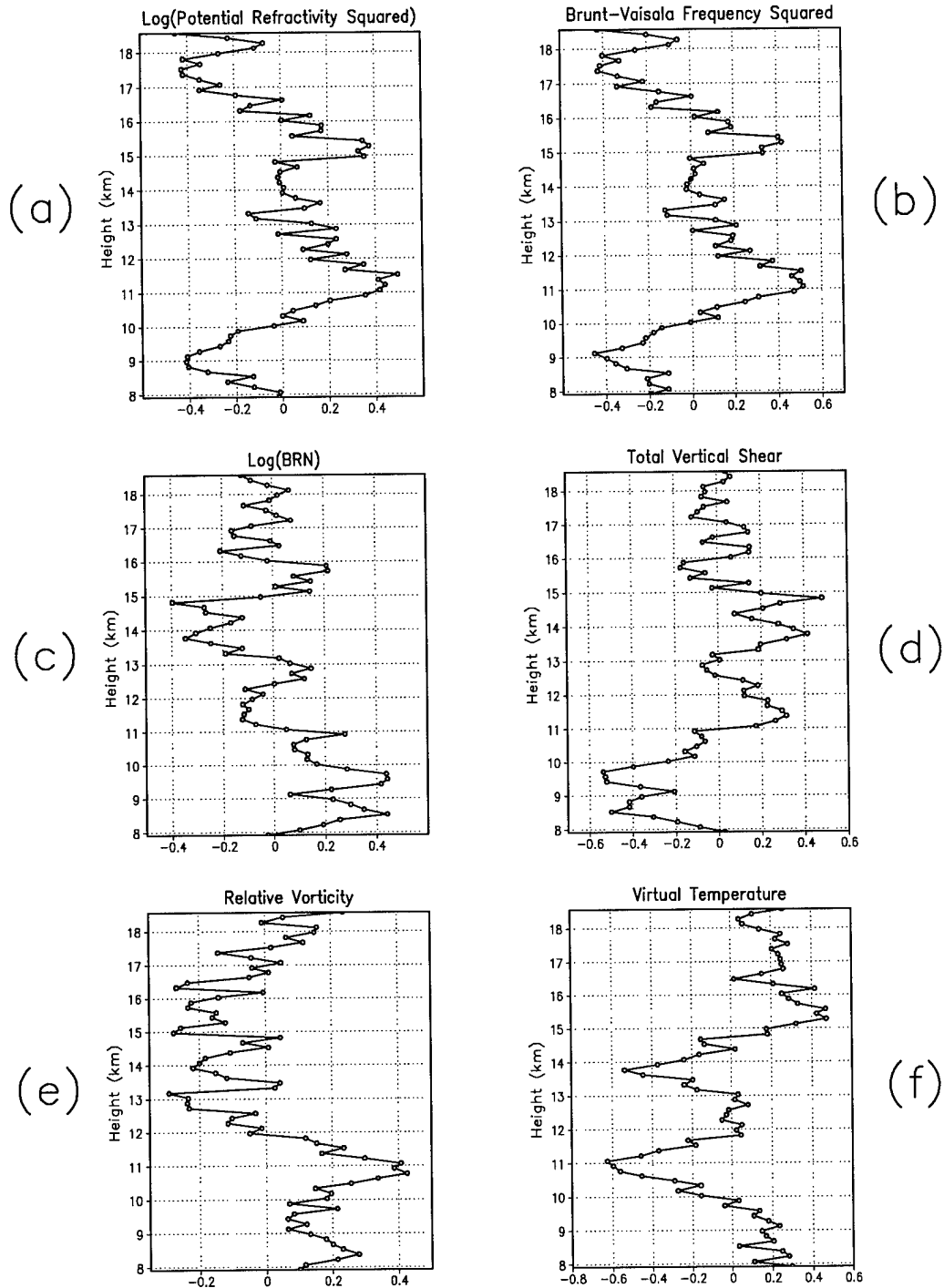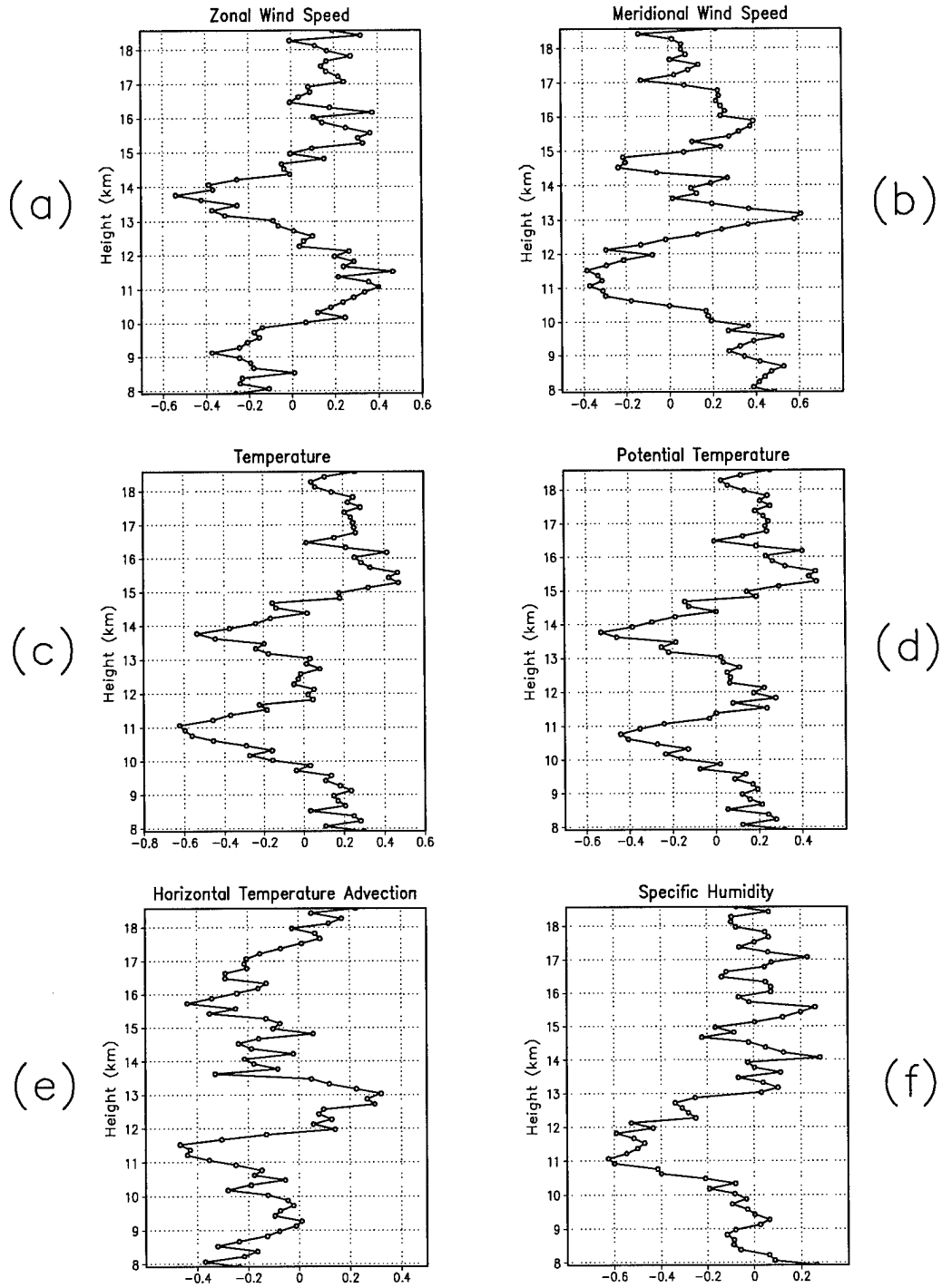
Figure 41   Case study 3 correlation coefficients of lag 0. Coefficients are computed at constant height between WSMR $\log(C_n^2)$ and variables at top of each graph.

The high $\log(C_n^2)$ seen from 27 April to 28 April between 8 km and 10 km is resolved into two patches in Figure 42. The high $\log(C_n^2)$ seen from 03 UTC to 15 UTC on 28 April corresponds to where the log of potential refractivity is high. However, the high $\log(C_n^2)$ seen from 15 UTC to 21 UTC on 27 April does not correspond to regions of high potential refractivity, high variance of radar measured wind speeds, nor a pattern of high total vertical shear. Further, high total variance of radar measured wind speed at 00 UTC 28 April occurs during a lull in $\log(C_n^2)$. This is inexplicable. Perhaps some assumptions within Tatarski's theory of C_n^2; such as specific humidity being conservative and passive, and no reflection of the radar's electromagnetic waves (11:40, 59-77); do not hold here. The other feature of interest for this case study also occurs at these times, but aloft between 15 km and 18 km.

5.3.3 Mid-Tropopause to Lower Stratosphere. As noted earlier, the upper band of high $\log(C_n^2)$ resides at the stratospheric inversion. The high $\log(C_n^2)$ seen on 28 April 1996 at the stratospheric inversion might be associated with the approach and departure of the polar jet, seen in Figures 34 and 35 from 00 UTC 28 April 1996 to 12 UTC 29 April 1996. Between 00 UTC and 12 UTC 28 April, the polar jet becomes cyclonically curved. Figure 43 shows radar zonal wind speeds averaged in 30 minute intervals and a modulated wave pattern appearing in the speeds. The modulation of speed could be from internal gravity waves in the cyclonic flow of the jet. Gravity waves might be propagating upwards from this region and providing a source of energy for mechanical turbulence aloft, enhancing C_n^2. Figure 44 shows that the high $\log(C_n^2)$ occurs in a motley of high potential refractivity, total wind speed variance, and total vertical shear (calculated from radar wind speeds). Any of these could be a source of high C_n^2 in this region.

Values of P are shown in Figure 45. A band of P values greater than 1 follows the lower tropopause boundary. The lower stratosphere boundary can be seen in values of P close to 1 or greater than 1. From 25 April to 26 April 1996 between 8 km and 10 km, very high values of P exist. The passage of a trough during these
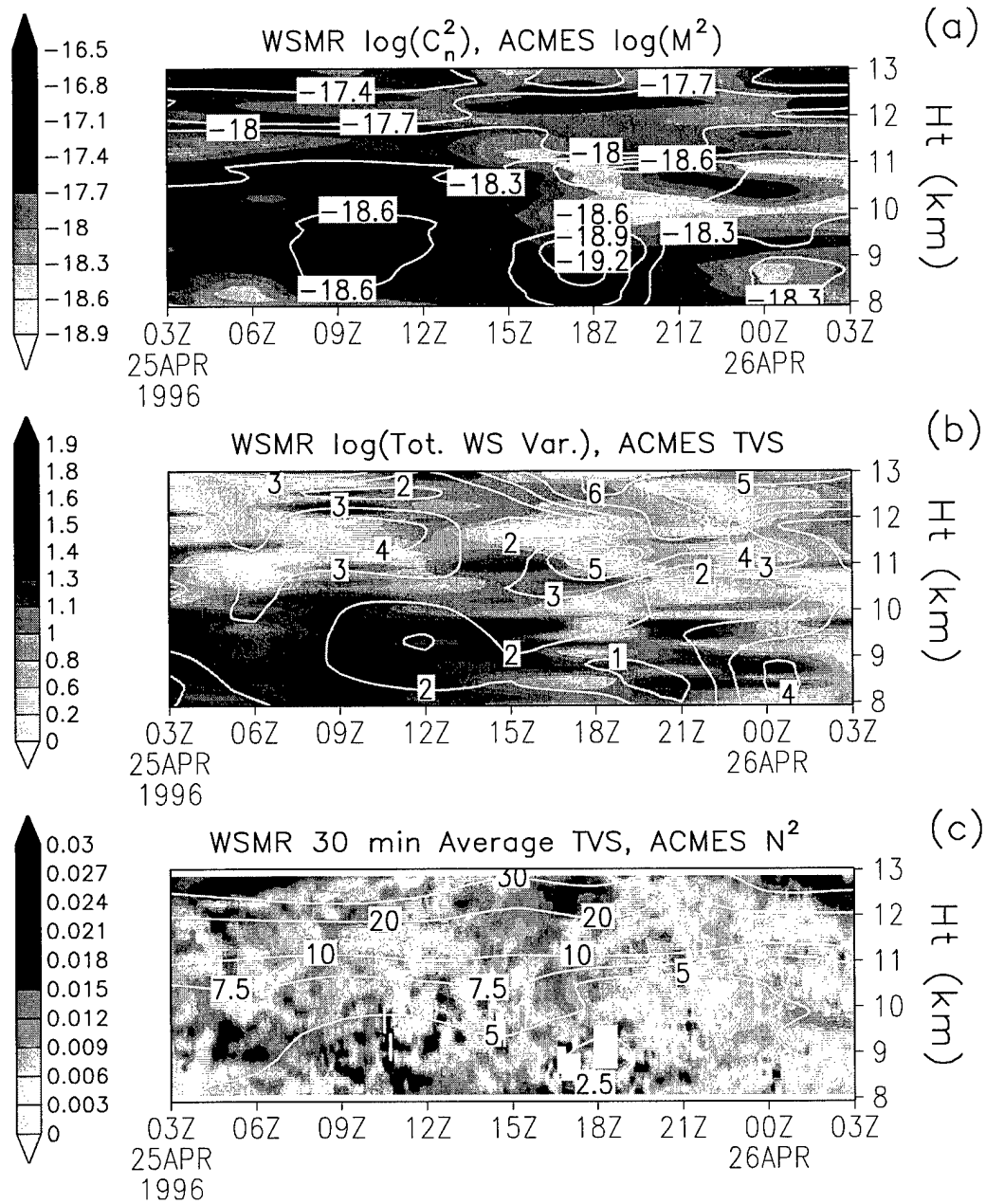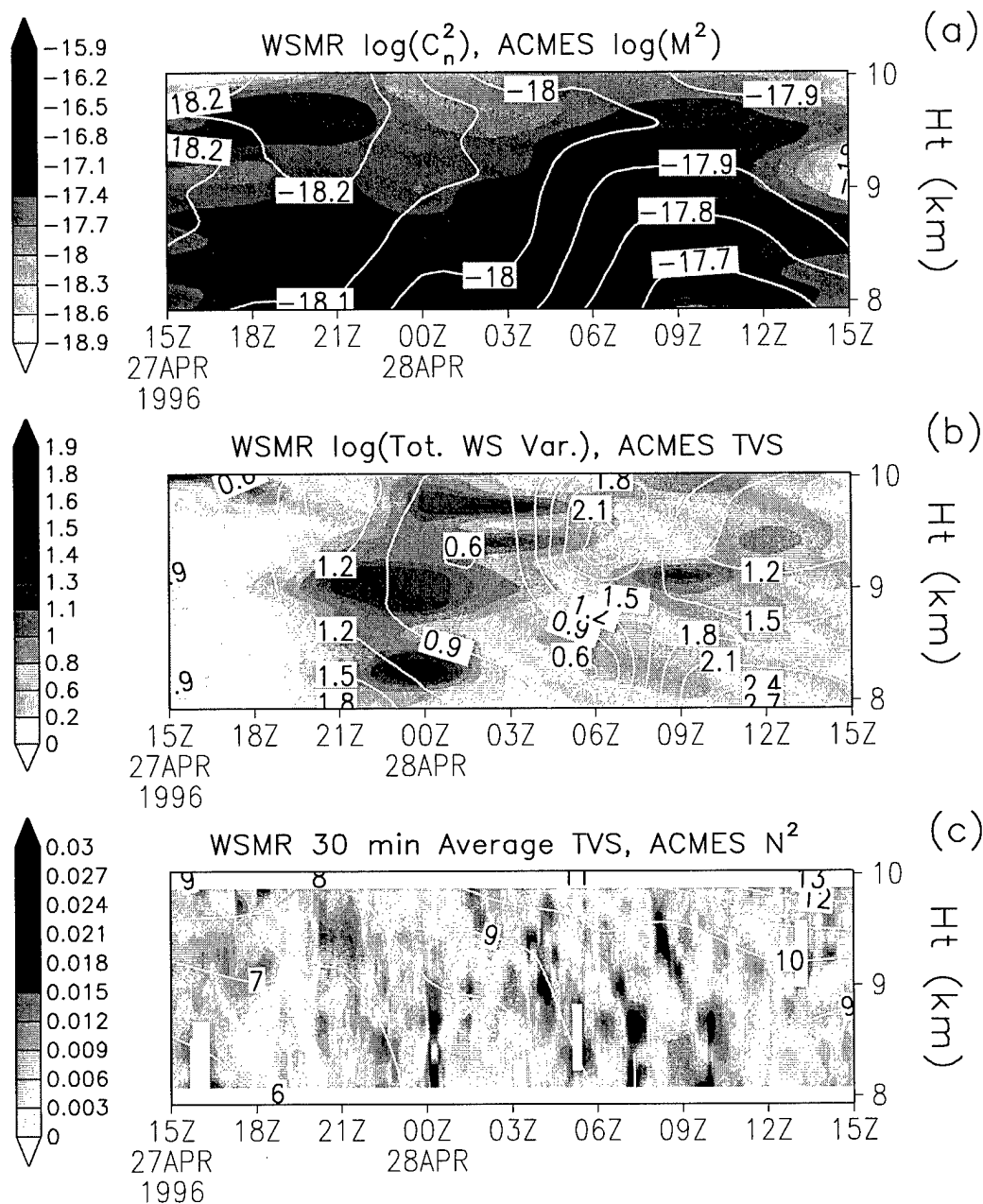
Figure 42   Case study 3 lower-level WSMR and ACMES data from 27 April to 28 April 1996.   (a)   The logarithm of potential refractivity squared is contoured.   (b)   The logarithm of WSMR total wind speed variance, (m^2/s^2) is shaded.   ACMES total vertical shear (1/s) is multiplied by 10^4.   (c)   WSMR radar total vertical shear (1/s) is shaded.   Brunt-Väisälä frequency squared $(1/s^2)$ is multiplied by 10^5.   White blocks are missing data that have been quality controlled.

67 of 115

67
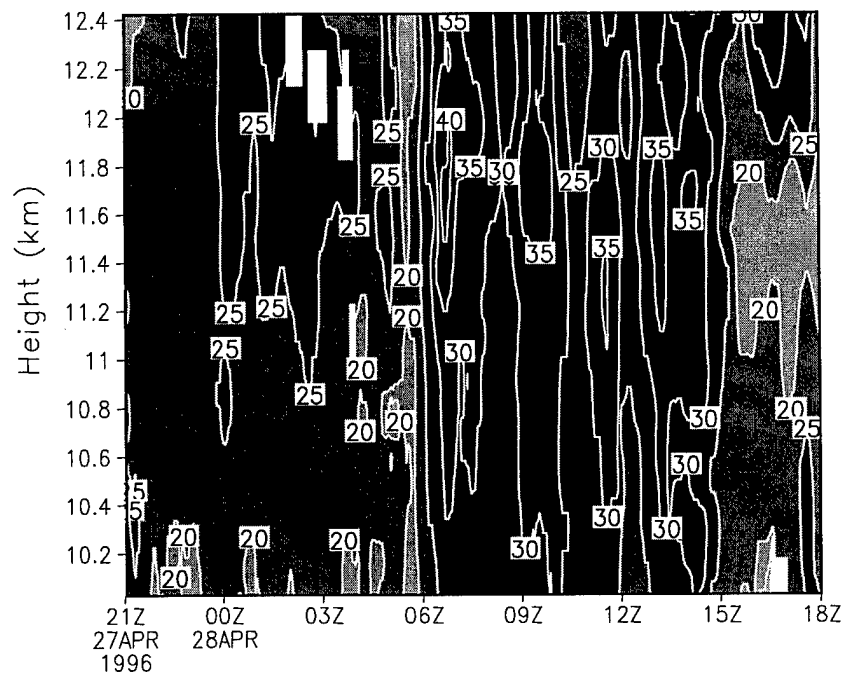
Figure 43   Case study 3 WSMR 30 min average zonal wind speed (m/s).   Zonal
wind speed measured every three minutes by the WSMR radar is aver-
aged about 30 minute intervals. A wave pattern appears in the region of
maximum wind speeds between 06 UTC 28 April and 15 UTC 28 April.
White blocks are missing data that have been quality controlled.

68
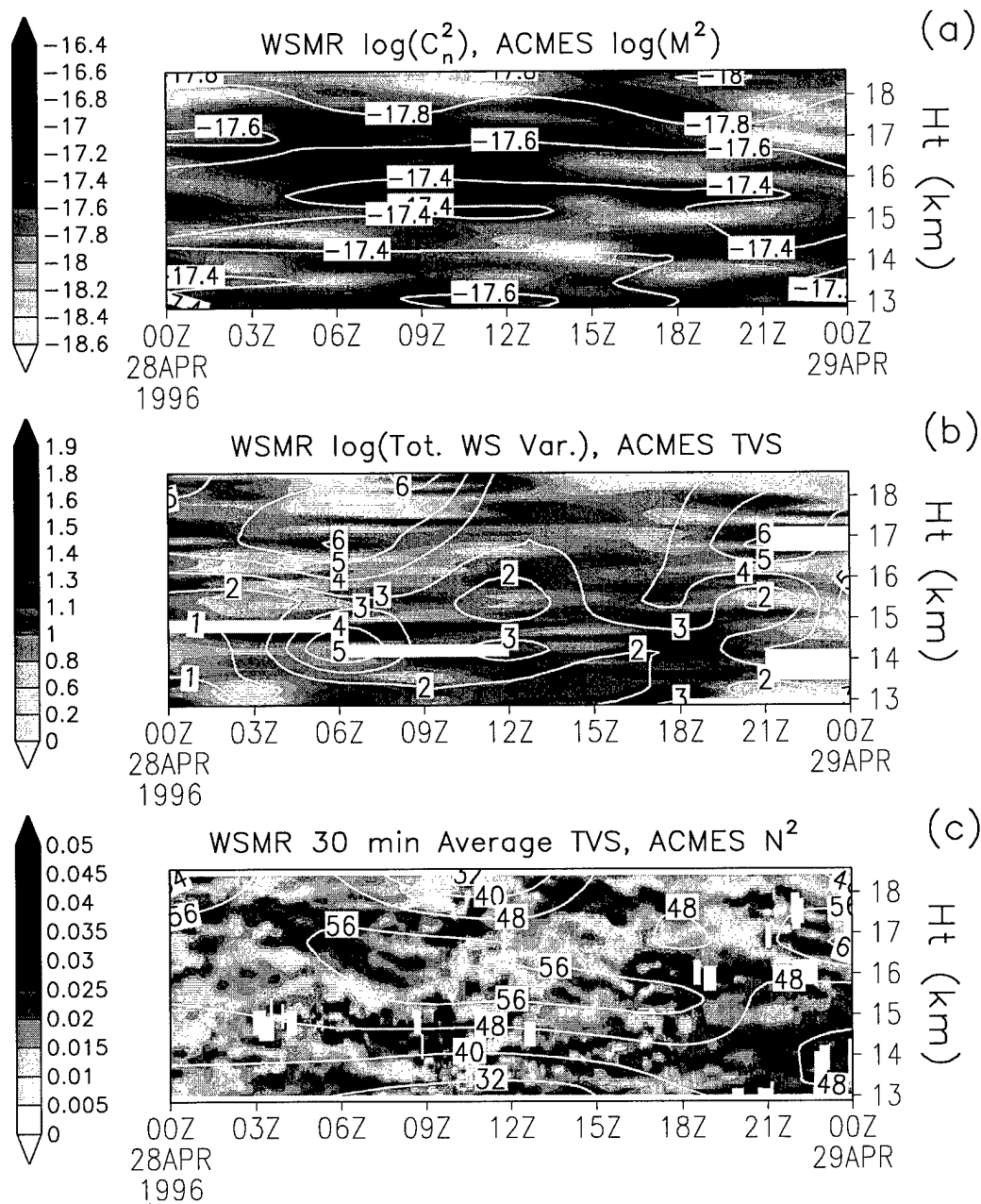
Figure 44   Case study 3 upper-level WSMR and ACMES data from 28 April to 29 April 1996.   (a) The logarithm of potential refractivity squared is contoured.   (b) The logarithm of WSMR total wind speed variance, (m^2/s^2) is shaded.   ACMES total vertical shear (1/s) is multiplied by 10^4.   (c) WSMR radar total vertical shear (1/s) is shaded.   Brunt-Väisälä frequency squared $(1/s^2)$ is multiplied by 10^5.   White blocks are missing data that have been quality controlled.
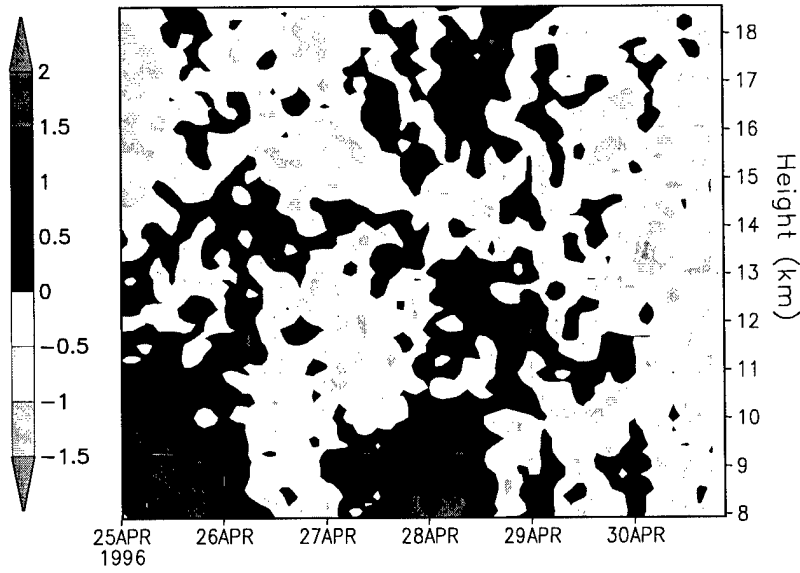
Figure 45   Case study 3 calculated $\log(P)$.   Values of $\log(P)$ are calculated by subtracting ACMES $\log(M^2)$ data from the WSMR $\log(C_n^2)$ data.

times and during 27 April to 28 April 1996 is likely associated with the higher values seen at these heights.

5.3.4   Summary.   This case study occurs south of the polar jet, but more north of the subtropical jet.   The negative correlation of $\log(C_n^2)$ to $\log(M^2)$ from 8 km to 10 km is explained by a patch of high $\log(C_n^2)$ occurring on 25 April 1996; which is not accountable by potential refractivity alone, but by increased mechanical turbulence.   Strong vertical shear during this time could be providing energy for the mechanically turbulent activity.   Turbulent behavior associated with the passage of a trough at this time might also be a source for the mechanical turbulence and high C_n^2 seen, changing the parameters P in $C_n^2 = PM^2$.

Another patch of high $\log(C_n^2)$ seen at these same heights on 27 April 1996 can not be explained by potential refractivity, high variance of radar measured wind speeds, nor total vertical shear.   However, a region of high $\log(C_n^2)$ seen at the stratospheric inversion on 28 April during the approach of the polar jet can explained by various factors: gravity wave activity providing a source of energy for turbulent

70

kinetic energy, high potential refractivity, high variance of radar measured wind speeds showing mechanical turbulence, and strong total vertical shear providing a source of turbulent kinetic energy.

VI. Conclusion

6.1 Summary of Results

In the analysis of this work, six meteorological features were found likely to affect C_n^2. Two of the features are directly related to potential refractivity, M, and the other four are related to the various other parameters in C_n^2, grouped into one called P.

The two meteorological features associated with affecting potential refractivity, and thus C_n^2, are jets and inversions. In the upper troposphere to lower tropopause, a good linear relationship exists between $\log(C_n^2)$ and $\log(M^2)$. The correlation is strong in the presence of a jet as vertical wind shear affects horizontal temperature gradients, which affect potential refractivity. This relationship between vertical wind shear and horizontal temperature gradients is due to the thermal wind relationship, not turbulent kinetic energy from shear. At jet core level, higher values of C_n^2 can be expected north, or on the lower pressure side, of the jet core where potential refractivity is greater from the increased static stability. South of jet core level, lower values of C_n^2 can be expected. Farther away from a jet, the correlation between $\log(C_n^2)$ and $\log(M^2)$ is lower. Synoptic-scale dynamics plays a strong and predictable role in affecting C_n^2 when a jet core is present in both time and space. The other meteorological feature which affects potential refractivity, and thus C_n^2, is temperature inversions. Typically higher values of C_n^2 can be found just above inversions, in the warmer side, as a result of warmer temperatures increasing potential refractivity, resulting in higher C_n^2. Cooler temperatures beneath inversions make for comparatively lower values of C_n^2, assuming similar values of P in $C_n^2 = PM^2$.

The remaining four meteorological features are related to effects on P, and thus C_n^2. The first feature is the effect of strong vertical wind shear on P. Bands of high C_n^2 occur within regions of strong vertical wind shear. During the approach of jets, very high wind shears are seen in the fine-scale radar data which correspond

almost exactly to the same location as the high C_n^2 seen by the radar. The bands of high C_n^2 cannot be accounted for by potential refractivity alone. It is likely that the strong vertical shear of wind is a source of turbulent kinetic energy, enhancing C_n^2. The second feature is high C_n^2 occasionally seen underneath inversions during the approach of jets that are associated with gravity waves. Gravity waves might be propagating kinetic energy into regions underneath inversions, providing turbulent kinetic energy and enhancing C_n^2. The other two meteorological features are tropopause boundaries and trough passage. High values of P are seen along the lower and upper tropopause boundaries, and during trough passage. Values of P tend to be greater than 1 along the tropopause boundaries and during trough passage. Between the two tropopause boundaries, values of P are typically less than 1, except in mechanically turbulent regions where P tends to become much greater than one–by one or two orders of magnitude. Along these boundaries and during trough passage, perhaps the outer scale of turbulence changes, or the amount of kinetic energy available for cascade through the inertial subrange changes. Vertical temperature gradients alone do not account for the patterns seen.

6.2 Remarks

Before concluding with a recommendation for future research, first a few remarks on modeling C_n^2.

Some regions of strong vertical wind shear seen in the WSMR radar data correspond to regions of high C_n^2. It is discouraging to find that the ACMES data, with a grid resolution of about 11 km, do not always show regions of strong vertical shear that are seen with the radar data. It is important to note that models will not always be accurate. The theory behind the quantities being modeled might be very accurate, but initial data values entered into a model and the model output might not always be.

Also, theory states C_n^2 is proportional to M^2, the square of potential refractivity. As potential refractivity is proportional to vertical temperature gradients and the Brunt-Väisälä frequency squared in dry environments, one would expect high C_n^2 in high Brunt-Väisälä frequency environments. The intensity of turbulence in the index of refraction is proportional to N^2 in dry environments. However, mechanical turbulence is likely in regions of low buoyant Richardson number, where $R_i = N^2 \div \left(\dfrac{\partial v}{\partial z}\right)^2$. For a given total wind shear, one would expect a greater probability of mechanical turbulence in low N^2 regions. As mechanical turbulence is the most likely reason for enhanced C_n^2 seen, a conflict between the two turbulence types arises. The best manner for prediction of C_n^2 resides in modifying the parameters P in $C_n^2 = PM^2$ to account for mechanical turbulence. Even this can lead to inconsistencies between modeled values of C_n^2 and actual values of C_n^2 in the atmosphere, as the potential for mechanically turbulent activity does not imply the turbulence will occur. However, any model for C_n^2 which does not account for mechanically turbulent activity, from strong vertical shear or possibly gravity wave activity, can produce huge inconsistencies between predicted values and actual C_n^2 observed in the atmosphere.

6.3 Recommendation for Future Research

Rather than qualitatively describing regions where mechanically turbulent activity exists, enhancing C_n^2, quantitatively parametrizing mechanically turbulent activity into the parameters P in $C_n^2 = PM^2$ would be most useful for modeling C_n^2. Including an accurate parametrization of mechanical turbulence into C_n^2 would be most useful to forecasters as an aid in forecasting optically turbulent regions of the atmosphere.

Appendix A. Thermal Wind Relationship

For winds in geostrophic balance in a hydrostatic environment, vertical gradients of wind speed and horizontal gradients of temperature are related through the thermal wind relationship.

Balance of the horizontal pressure gradient force with the Coriolis force on a rotating earth define the geostrophic wind.

$$-\frac{\partial \Phi}{\partial y} = f u_g \tag{A.1}$$

$$-\frac{\partial \Phi}{\partial x} = -f v_g \tag{A.2}$$

Substituting the Ideal Gas Law $\rho = \dfrac{p}{RT}$ into the hydrostatic equation yields

$$\left(\frac{RT}{p}\right)_p = -\frac{\partial \Phi}{\partial p} \tag{A.3}$$

Differentiating geostrophic equation (A.1) with respect to pressure

$$\frac{\partial}{\partial p}\left[-\frac{\partial \Phi}{\partial y}\right] = \frac{\partial}{\partial p}\left[f u_g\right]$$

$$-\frac{\partial^2 \Phi}{\partial p \partial y} = f \frac{\partial u_g}{\partial p}$$

Assuming Φ is continuous

$$-\frac{\partial^2 \Phi}{\partial y \partial p} = f \frac{\partial u_g}{\partial p}$$

$$\frac{\partial}{\partial y}\left[-\frac{\partial \Phi}{\partial p}\right] = f\frac{\partial u_g}{\partial p}$$

Substituting in equation (A.3)

$$\frac{\partial}{\partial y}\left[\left(\frac{RT}{p}\right)_p\right] = f\frac{\partial u_g}{\partial p}$$

$$\frac{R}{p}\frac{\partial}{\partial y}\left[(T)_p\right] = f\frac{\partial u_g}{\partial p}$$

$$\left(\frac{\partial T}{\partial y}\right)_p = \frac{fp}{R}\frac{\partial u_g}{\partial p} \tag{A.4}$$

Similarly for v_g

$$\left(\frac{\partial T}{\partial x}\right)_p = -\frac{fp}{R}\frac{\partial v_g}{\partial p} \tag{A.5}$$

Equations (A.4) and (A.5) define the thermal wind relationship in differential form.

A picture of the thermal wind relationship is shown in Figure 46. Near the core of a jet in the northern hemisphere, the lapse rate north of the core decreases. The potential temperature curves for this figure are shown in Figure 47. Higher static stability occurs north of the jet core. Assuming moisture and other parameters are the same at jet core level in the northern hemisphere, higher C_n^2 would exist to the north of the core, and lower C_n^2 to the south as $C_n^2 \propto M^2 \propto \left(\frac{\partial \theta}{\partial z}\right)^2$.
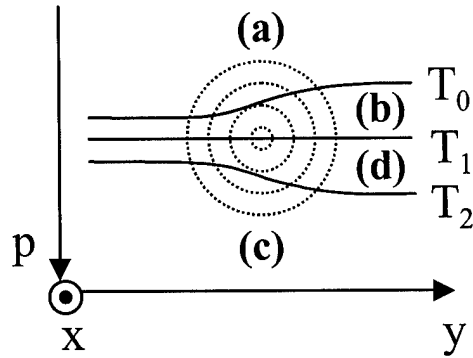
Figure 46   Appendix A thermal wind and temperature. With $v_g = 0$, u_g comes out of the diagram and speed is denoted by concentric circles, with greater speeds in the center. In region (a), $\dfrac{\partial u_g}{\partial p} > 0$ making $\left(\dfrac{\partial T}{\partial y}\right)_p > 0$ (in the northern hemisphere). The lapse rate decreases in region (b). The shear of winds at (c) also decrease the lapse rate in region (d).
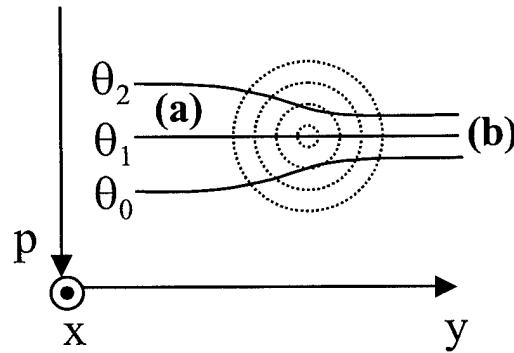
Figure 47   Appendix A thermal wind and potential temperature. With $v_g = 0$, u_g comes out of the diagram and speed is denoted by concentric circles, with greater speeds in the center. At jet core level in the northern hemisphere, the thermal wind relationship decreases static stability south of the jet (a) and increases it to the north (b).

Appendix B. C_n^2 and Temperature Inversions

At an inversion in a dry, hydrostatic environment, C_n^2 will be greater just above the inversion than below, assuming constant P in $C_n^2 = PM^2$.

Starting with the definition of potential temperature and then differentiating with respect to height

$$\theta = T \left(\frac{p_0}{p} \right)^\kappa \qquad \text{with} \qquad \kappa = \frac{R}{c_p} \tag{B.1}$$

$$\frac{\partial}{\partial z}[\theta] = \frac{\partial}{\partial z}\left[T \left(\frac{p_0}{p} \right)^\kappa \right]$$

$$\frac{\partial \theta}{\partial z} = \left(\frac{p_0}{p} \right)^\kappa \frac{\partial}{\partial z}[T] + T \frac{\partial}{\partial z}\left[\left(\frac{p_0}{p} \right)^\kappa \right]$$

$$\frac{\partial \theta}{\partial z} = \left(\frac{p_0}{p} \right)^\kappa \frac{\partial T}{\partial z} + T p_0^\kappa \frac{\partial}{\partial z}\left[p^{-\kappa} \right]$$

$$\frac{\partial \theta}{\partial z} = \left(\frac{p_0}{p} \right)^\kappa \frac{\partial T}{\partial z} + T p_0^\kappa \left(\frac{-\kappa}{p^{(\kappa+1)}} \right) \frac{\partial p}{\partial z}$$

$$\frac{\partial \theta}{\partial z} = \left(\frac{p_0}{p} \right)^\kappa \frac{\partial T}{\partial z} + T p_0^\kappa \left(\frac{-\kappa}{pp^\kappa} \right) \frac{\partial p}{\partial z}$$

$$\frac{\partial \theta}{\partial z} = \left(\frac{p_0}{p} \right)^\kappa \frac{\partial T}{\partial z} - \frac{\kappa T}{p} \left(\frac{p_0}{p} \right)^\kappa \frac{\partial p}{\partial z} \tag{B.2}$$

In a hydrostatic environment, $\frac{\partial p}{\partial z} = -\rho g$. Substituting into equation (B.2) yields

$$\frac{\partial \theta}{\partial z} = \left(\frac{p_0}{p}\right)^{\kappa} \frac{\partial T}{\partial z} - \frac{\kappa T}{p} \left(\frac{p_0}{p}\right)^{\kappa} (-\rho g)$$

$$\frac{\partial \theta}{\partial z} = \left(\frac{p_0}{p}\right)^{\kappa} \frac{\partial T}{\partial z} + \frac{\rho g \kappa T}{p} \left(\frac{p_0}{p}\right)^{\kappa}$$

Substituting in the Ideal Gas Law, $\rho = \frac{p}{RT}$, yields

$$\frac{\partial \theta}{\partial z} = \left(\frac{p_0}{p}\right)^{\kappa} \frac{\partial T}{\partial z} + \frac{\left(\frac{p}{RT}\right) g \kappa T}{p} \left(\frac{p_0}{p}\right)^{\kappa}$$

$$\frac{\partial \theta}{\partial z} = \left(\frac{p_0}{p}\right)^{\kappa} \frac{\partial T}{\partial z} + \frac{p g \kappa T}{p R T} \left(\frac{p_0}{p}\right)^{\kappa}$$

$$\frac{\partial \theta}{\partial z} = \left(\frac{p_0}{p}\right)^{\kappa} \frac{\partial T}{\partial z} + \frac{g \kappa}{R} \left(\frac{p_0}{p}\right)^{\kappa}$$

$$\frac{\partial \theta}{\partial z} = \left(\frac{p_0}{p}\right)^{\kappa} \left(\frac{\partial T}{\partial z} + \frac{g \kappa}{R}\right)$$

Substituting the definition of θ (B.1) back into the above equation yields

$$\frac{\partial \theta}{\partial z} = \frac{\theta}{T} \left(\frac{\partial T}{\partial z} + \frac{g}{c_p}\right) \tag{B.3}$$

79

Potential refractivity in a dry atmosphere, with $q = 0$ and $\frac{\partial q}{\partial z} = 0$, is given by

$$M = c_2 \frac{p}{T\theta} \frac{\partial \theta}{\partial z} \tag{B.4}$$

Substituting in equation (B.3) yields

$$M = c_2 \frac{p}{T\theta} \frac{\theta}{T} \left(\frac{\partial T}{\partial z} + \frac{g}{c_p} \right)$$

$$M = c_2 \frac{p}{T^2} \left(\frac{\partial T}{\partial z} + \frac{g}{c_p} \right) \tag{B.5}$$

And so C_n^2 given by

$$C_n^2 = PM^2$$

becomes

$$C_n^2 = P \left(c_2 \frac{p}{T^2} \left(\frac{\partial T}{\partial z} + \frac{g}{c_p} \right) \right)^2$$

$$C_n^2 = P' \frac{p^2}{T^4} \left(\frac{\partial T}{\partial z} + \frac{g}{c_p} \right)^2 \tag{B.6}$$

For the case of an inversion in a dry, hydrostatic atmosphere shown in Figure 48 with $\left(\frac{\partial T}{\partial z} \right)_{z_m} = 0$, $\left(\frac{\partial T}{\partial z} \right)_{z_l} < 0$, $\left(\frac{\partial T}{\partial z} \right)_{z_u} > 0$ and assuming a constant P', the lower C_n^2 is given by

$$C_n^2(z_l) = P' \frac{p^2(z_l)}{T^4(z_l)} \left(\left(\frac{\partial T}{\partial z} \right)_{z_l} + \frac{g}{c_p} \right)^2$$
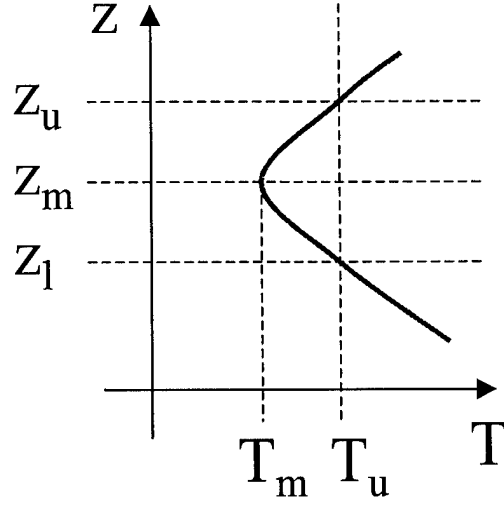
Figure 48   Appendix B lapse rate.

$$C_n^2(z_l) = P' \frac{p_l^2}{T_u^4} \left(- \left| \frac{\partial T}{\partial z} \right|_{z_l} + \frac{g}{c_p} \right)^2 \qquad \text{(B.7)}$$

And the upper C_n^2 is given by

$$C_n^2(z_u) = P' \frac{p^2(z_u)}{T^4(z_u)} \left(\left(\frac{\partial T}{\partial z} \right)_{z_u} + \frac{g}{c_p} \right)^2$$

$$C_n^2(z_u) = P' \frac{p_u^2}{T_u^4} \left(\left| \frac{\partial T}{\partial z} \right|_{z_u} + \frac{g}{c_p} \right)^2 \qquad \text{(B.8)}$$

Taking the ratio of the two C_n^2 yields

$$\frac{C_n^2(z_l)}{C_n^2(z_u)} = \frac{P' \dfrac{p_l^2}{T_u^4} \left(- \left| \dfrac{\partial T}{\partial z} \right|_{z_l} + \dfrac{g}{c_p} \right)^2}{P' \dfrac{p_u^2}{T_u^4} \left(\left| \dfrac{\partial T}{\partial z} \right|_{z_u} + \dfrac{g}{c_p} \right)^2}$$

81

$$\frac{C_n^2(z_l)}{C_n^2(z_u)} = \left(\frac{p_l}{p_u}\right)^2 \frac{\left(-\left|\frac{\partial T}{\partial z}\right|_{z_l} + \frac{g}{c_p}\right)^2}{\left(\left|\frac{\partial T}{\partial z}\right|_{z_u} + \frac{g}{c_p}\right)^2}$$

$$\frac{C_n^2(z_l)}{C_n^2(z_u)} = \left(\frac{p_l}{p_u}\right)^2 \frac{\left|\frac{\partial T}{\partial z}\right|_{z_l}^2 - 2\frac{g}{c_p}\left|\frac{\partial T}{\partial z}\right|_{z_l} + \left(\frac{g}{c_p}\right)^2}{\left|\frac{\partial T}{\partial z}\right|_{z_u}^2 + 2\frac{g}{c_p}\left|\frac{\partial T}{\partial z}\right|_{z_u} + \left(\frac{g}{c_p}\right)^2} \tag{B.9}$$

Close to the inversion with $\left(\frac{p_l}{p_u}\right) \approx 1$, and $\left|\frac{\partial T}{\partial z}\right|_{z_l} = \left|\frac{\partial T}{\partial z}\right|_{z_u}$, the denominator will be larger than the numerator. Therefore, C_n^2 in the upper level will be larger than C_n^2 in the lower level.

Appendix C. Turbulent Kinetic Energy Equation

The information in this appendix comes directly from P. K. Kundu's *Fluid Mechanics* (7:435-438). The purpose of this appendix is to briefly describe the terms in the turbulent kinetic energy (TKE) equation, as they are useful in describing the kinetic energy budget of fluid flows. As the derivation of the equation is involved, it is not covered.

The TKE equation is expressed in tensor notation

$$
\frac{D}{Dt}\overline{\left(\tfrac{1}{2}u_i^2\right)} = -\frac{\partial}{\partial x_j}\overbrace{\left(\frac{1}{\rho_0}\overline{pu_j} + \tfrac{1}{2}\overline{u_i^2 u_j} - 2\nu\overline{u_i e_{ij}}\right)}^{transport} \overbrace{-\overline{u_i u_j}\frac{\partial U_i}{\partial x_j}}^{shear\ prod} + \overbrace{g\alpha\overline{wT'}}^{buoyant\ prod} - \overbrace{2\nu\overline{e_{ij}e_{ij}}}^{viscous\ diss}
$$

$$(C.1)$$

where ν is kinematic viscosity, α is the thermal expansion coefficient, and e_{ij} is the fluctuating strain rate. More on these terms can be referenced in Kundu's book. Components of velocity are written in terms of a mean U_i and a fluctuating part u_i. Temperature is expressed as a sum of a mean and fluctuating part, $\overline{T} + T'$ respectively, as is pressure, $P + p$. Averaged quantities are time averages.

The transport terms of the TKE equation represent the spatial transport of TKE. The shear production term represents the rate of TKE generation from the interaction between Reynolds stress, $\overline{u_i u_j}$, and the mean shear of the fluid, $\frac{\partial U_i}{\partial x_j}$. The fifth term of the equation represents buoyant production or loss of TKE. The remaining term is the viscous dissipation term and is not negligible in the TKE budget of fluid flows.

Appendix D. Gravity Waves

The goal of this appendix is to show what gravity waves are and how they propagate. The equations which define gravity waves are covered first; then after describing the solutions to the equations with a dispersion relation, it is shown how they propagate.

D.1 Governing Equations

The equation of motion and the continuity equation are the two governing equations which are used to describe gravity waves here. These equations are defined first, simplified by the method of perturbations, and then combined so that solutions can be found in the next section.

D.1.1 Definitions. For a material volume element of the atmosphere on a rotating planet, the sum of surface and body forces acting on the element define the equation of motion. The forces acting on the element are the pressure gradient force, the Coriolis force, the gravitational force, and a frictional force. For simplicity, curvature of flow is not considered.

$$\overset{net}{M\frac{d\vec{v}}{dt}} = \overset{P.G.F.}{-\frac{M}{\rho}\nabla p} \overset{Coriolis}{-2M\vec{\Omega}\times\vec{v}} + \overset{gravity}{M\vec{g}} + \overset{friction}{\vec{F_F}} \tag{D.1}$$

Considering time scales less than the period of rotation of the planet, and no frictional forces (which is a fair assumption above the planetary boundary layer), the equation of motion reduces to

$$\overset{net}{M\frac{d\vec{v}}{dt}} = \overset{P.G.F.}{-\frac{M}{\rho}\nabla p} + \overset{gravity}{M\vec{g}} \tag{D.2}$$

84

Conservation of mass in the atmosphere is expressed in the continuity equation. For a moving element, a change in mass with respect to time is equal to the amount of mass leaving or entering the element. Loss is from divergence.

$$-\frac{d\rho}{dt} = \rho \nabla \cdot \vec{v} \tag{D.3}$$

or

$$\frac{d\rho}{dt} + \rho \nabla \cdot \vec{v} = 0 \tag{D.4}$$

D.1.2 Method of Perturbations. Equations (D.2) and (D.4) are simplified by the method of perturbations. This simplification converts the two equations into linear differential equations, which are more easily managed. Assumptions are that quantities can be expressed as a sum of a mean and a perturbation. The perturbation is small compared to the mean; consequently, products of perturbations are small compared to other terms in equations and are dropped. The linearization of the equations depends upon this. Separately, both the mean and the perturbation parts are solutions to the governing equations.

For gravity wave solutions, other assumptions are made to simplify the equations. The first assumptions are that the mean quantities are steady-state and *horizontally* homogeneous. Another assumption is that elements as a whole are incompressible, that is $\frac{d\rho}{dt} = 0$. The last important assumption is that the mean flow speed is zero. This assumption not only simplifies the equations, but also allows for easier comparison of the solution to the mean flow.

Looking first at the zonal component of wind in equation (D.2) and assuming $u = \overline{u} + u'$, $\rho = \overline{\rho} + \rho'$, and $p = \overline{p} + p'$

$$\rho \frac{d\vec{v}}{dt} = -\nabla p + \rho \vec{g}$$

$$\left(\overline{\rho} + \rho'\right) \frac{d}{dt}\left[\overline{u} + u'\right] = -\frac{\partial}{\partial x}\left[\overline{p} + p'\right]$$

$$\overline{\rho}\frac{d\overline{u}}{dt} + \rho'\frac{d\overline{u}}{dt} + \overline{\rho}\frac{du'}{dt} + \rho'\frac{du'}{dt} = -\frac{\partial \overline{p}}{\partial x} - \frac{\partial p'}{\partial x}$$

$$\left(\overline{\rho}\frac{d\overline{u}}{dt} + \frac{\partial \overline{p}}{\partial x}\right) + \rho'\frac{d\overline{u}}{dt} + \overline{\rho}\frac{du'}{dt} + \rho'\frac{du'}{dt} = -\frac{\partial p'}{\partial x}$$

Since the mean $\overline{u}$ is a solution to the original equation

$$(0) + \rho'\frac{d\overline{u}}{dt} + \overline{\rho}\frac{du'}{dt} + \rho'\frac{du'}{dt} = -\frac{\partial p'}{\partial x}$$

Since mean wind speed is zero

$$\rho'0 + \overline{\rho}\frac{du'}{dt} + \rho'\frac{du'}{dt} = -\frac{\partial p'}{\partial x}$$

$$\overline{\rho}\left(\frac{\partial u'}{\partial t} + \overrightarrow{v}\cdot\nabla u'\right) + \rho'\left(\frac{\partial u'}{\partial t} + \overrightarrow{v}\cdot\nabla u'\right) = -\frac{\partial p'}{\partial x}$$

$$\overline{\rho}\left(\frac{\partial u'}{\partial t} + \overrightarrow{\overline{v}}\cdot\nabla u' + \overrightarrow{v'}\cdot\nabla u'\right) + \rho'\left(\frac{\partial u'}{\partial t} + \overrightarrow{\overline{v}}\cdot\nabla u' + \overrightarrow{v'}\cdot\nabla u'\right) = -\frac{\partial p'}{\partial x}$$

Again, the mean wind is zero

$$\overline{\rho}\left(\frac{\partial u'}{\partial t} + 0 + \overrightarrow{v'}\cdot\nabla u'\right) + \rho'\left(\frac{\partial u'}{\partial t} + 0 + \overrightarrow{v'}\cdot\nabla u'\right) = -\frac{\partial p'}{\partial x}$$

$$\overline{\rho}\left(\frac{\partial u'}{\partial t} + \overrightarrow{v'}\cdot\nabla u'\right) + \rho'\left(\frac{\partial u'}{\partial t} + u'\frac{\partial u'}{\partial x} + v'\frac{\partial u'}{\partial y} + w'\frac{\partial u'}{\partial z}\right) = -\frac{\partial p'}{\partial x}$$

86

$$\overline{\rho}\left(\frac{\partial u'}{\partial t} + \overrightarrow{v'} \cdot \nabla u'\right) + \rho'\frac{\partial u'}{\partial t} + \rho'u'\frac{\partial u'}{\partial x} + \rho'v'\frac{\partial u'}{\partial y} + \rho'w'\frac{\partial u'}{\partial z} = -\frac{\partial p'}{\partial x}$$

Since products of perturbations are small compared to other terms

$$\overline{\rho}\left(\frac{\partial u'}{\partial t} + \overrightarrow{v'} \cdot \nabla u'\right) + \rho'\frac{\partial u'}{\partial t} + 0\frac{\partial u'}{\partial x} + 0\frac{\partial u'}{\partial y} + 0\frac{\partial u'}{\partial z} = -\frac{\partial p'}{\partial x}$$

$$\overline{\rho}\frac{\partial u'}{\partial t} + \overline{\rho}\overrightarrow{v'} \cdot \nabla u' + \rho'\frac{\partial u'}{\partial t} = -\frac{\partial p'}{\partial x}$$

$$\overline{\rho}\frac{\partial u'}{\partial t} + \overline{\rho}u'\frac{\partial u'}{\partial x} + \overline{\rho}v'\frac{\partial u'}{\partial y} + \overline{\rho}w'\frac{\partial u'}{\partial z} + \rho'\frac{\partial u'}{\partial t} = -\frac{\partial p'}{\partial x}$$

Scale analysis shows products of perturbation quantities and derivatives of perturbation quantities are much smaller than other terms. Therefore

$$\overline{\rho}\frac{\partial u'}{\partial t} + \overline{\rho}0 + \overline{\rho}0 + \overline{\rho}0 + 0 = -\frac{\partial p'}{\partial x}$$

$$\frac{\partial u'}{dt} = -\frac{1}{\overline{\rho}}\frac{\partial p'}{\partial x} \tag{D.5}$$

Similarly for the other two components of velocity

$$\frac{\partial v'}{dt} = -\frac{1}{\overline{\rho}}\frac{\partial p'}{\partial y} \tag{D.6}$$

$$\frac{\partial w'}{\partial t} = -\frac{1}{\overline{\rho}}\frac{\partial p'}{\partial z} - \frac{\rho'}{\overline{\rho}}g \tag{D.7}$$

Since elements are assumed to be incompressible, the continuity equation (D.4) becomes

$$0 + \rho \nabla \cdot \vec{v} = 0$$

$$\rho \left(\frac{\partial u}{\partial x} + \frac{\partial v}{\partial y} + \frac{\partial w}{\partial z} \right) = 0$$

$$\left(\frac{\partial u}{\partial x} + \frac{\partial v}{\partial y} + \frac{\partial w}{\partial z} \right) = 0$$

$$\left(\frac{\partial}{\partial x} \left[\bar{u} + u' \right] + \frac{\partial}{\partial y} \left[\bar{v} + v' \right] + \frac{\partial}{\partial z} \left[\bar{w} + w' \right] \right) = 0$$

$$\left(\frac{\partial \bar{u}}{\partial x} + \frac{\partial u'}{\partial x} \right) + \left(\frac{\partial \bar{v}}{\partial y} + \frac{\partial v'}{\partial y} \right) + \left(\frac{\partial \bar{w}}{\partial z} + \frac{\partial w'}{\partial z} \right) = 0$$

$$\left(\frac{\partial \bar{u}}{\partial x} + \frac{\partial \bar{v}}{\partial y} + \frac{\partial \bar{w}}{\partial z} \right) + \left(\frac{\partial u'}{\partial x} + \frac{\partial v'}{\partial y} + \frac{\partial w'}{\partial z} \right) = 0$$

$$\left(\nabla \cdot \vec{\bar{v}} \right) + \left(\frac{\partial u'}{\partial x} + \frac{\partial v'}{\partial y} + \frac{\partial w'}{\partial z} \right) = 0$$

And since the mean $\vec{\bar{v}}$ is a solution to the original equation $\rho \nabla \cdot \vec{v} = 0$

$$\left(\frac{\partial u'}{\partial x} + \frac{\partial v'}{\partial y} + \frac{\partial w'}{\partial z} \right) = 0 \qquad (D.8)$$

D.1.3 Combination. Now that the equation of motion (D.5) through (D.7) and continuity equation (D.8) are linearized from applying the method of perturba-

tions, they are combined to make equations in w' and p', for which wave solutions can be assumed in the next section. First, the continuity equation is differentiated with respect to time, so that the zonal and meridional components of velocity can be substituted in

$$\frac{\partial}{\partial t}\left[\frac{\partial u'}{\partial x} + \frac{\partial v'}{\partial y} + \frac{\partial w'}{\partial z}\right] = \frac{\partial}{\partial t}[0]$$

$$\frac{\partial^2 u'}{\partial t \partial x} + \frac{\partial^2 v'}{\partial t \partial y} + \frac{\partial^2 w'}{\partial t \partial z} = 0$$

Assuming that the perturbations are continuous,

$$\frac{\partial^2 u'}{\partial x \partial t} + \frac{\partial^2 v'}{\partial y \partial t} + \frac{\partial^2 w'}{\partial z \partial t} = 0$$

Substituting in the zonal (D.5) and meridional (D.6) components of velocity,

$$\frac{\partial}{\partial x}\left[-\frac{1}{\bar{\rho}}\frac{\partial p'}{\partial x}\right] + \frac{\partial}{\partial y}\left[-\frac{1}{\bar{\rho}}\frac{\partial p'}{\partial y}\right] + \frac{\partial^2 w'}{\partial z \partial t} = 0$$

$$-\frac{1}{\bar{\rho}}\frac{\partial^2 p'}{\partial x^2} - \frac{1}{\bar{\rho}}\frac{\partial^2 p'}{\partial y^2} + \frac{\partial^2 w'}{\partial z \partial t} = 0$$

$$\frac{\partial^2 p'}{\partial x^2} + \frac{\partial^2 p'}{\partial y^2} = \bar{\rho}\frac{\partial^2 w'}{\partial z \partial t} \tag{D.9}$$

Equation (D.9) is the first equation expressing gravity wave solutions. The last equation begins with the assumption that the elements are incompressible

$$\frac{d\rho}{dt} = 0$$

89

$$\frac{d\rho}{dt} = \frac{\partial \rho}{\partial t} + \vec{v} \cdot \nabla \rho = 0$$

$$\frac{\partial}{\partial t}\left[\overline{\rho} + \rho'\right] + \vec{\overline{v}} \cdot \nabla\left[\overline{\rho} + \rho'\right] + \vec{v'} \cdot \nabla\left[\overline{\rho} + \rho'\right] = 0$$

Since the mean pressure is steady-state and the mean wind is zero

$$0 + \frac{\partial \rho'}{\partial t} + 0 \cdot \nabla\left[\overline{\rho} + \rho'\right] + \vec{v'} \cdot \nabla\left[\overline{\rho} + \rho'\right] = 0$$

$$\frac{\partial \rho'}{\partial t} + \vec{v'} \cdot \nabla\left[\overline{\rho} + \rho'\right] = 0$$

$$\frac{\partial \rho'}{\partial t} + \vec{v'} \cdot \nabla\overline{\rho} + \vec{v'} \cdot \nabla\rho' = 0$$

Since the mean pressure is horizontally homogeneous

$$\frac{\partial \rho'}{\partial t} + \vec{v'} \cdot \left(0, 0, \frac{\partial \overline{\rho}}{\partial z}\right) + \vec{v'} \cdot \nabla\rho' = 0$$

$$\frac{\partial \rho'}{\partial t} + w'\frac{\partial \overline{\rho}}{\partial z} + \vec{v'} \cdot \nabla\rho' = 0$$

Scale analysis shows products of perturbation quantities and derivatives of perturbation quantities are much smaller than other terms. Therefore

$$\frac{\partial \rho'}{\partial t} + w'\frac{\partial \overline{\rho}}{\partial z} + 0 = 0$$

$$\frac{\partial \rho'}{\partial t} = -w'\frac{\partial \overline{\rho}}{\partial z} \tag{D.10}$$

Taking the vertical component of motion (D.7) and differentiating with respect to time

$$\frac{\partial}{\partial t}\left[\frac{\partial w'}{dt}\right] = \frac{\partial}{\partial t}\left[-\frac{1}{\bar{\rho}}\frac{\partial p'}{\partial z} - \frac{\rho'}{\bar{\rho}}g\right]$$

$$\frac{\partial^2 w'}{\partial t^2} = -\frac{1}{\bar{\rho}}\frac{\partial^2 p'}{\partial t \partial z} - \frac{g}{\bar{\rho}}\frac{\partial \rho'}{\partial t}$$

Substituting equation (D.10) in yields

$$\frac{\partial^2 w'}{\partial t^2} = -\frac{1}{\bar{\rho}}\frac{\partial^2 p'}{\partial t \partial z} - \frac{g}{\bar{\rho}}\left(-w'\frac{\partial \bar{\rho}}{\partial z}\right)$$

$$\frac{\partial^2 w'}{\partial t^2} - w'\frac{g}{\bar{\rho}}\frac{\partial \bar{\rho}}{\partial z} + \frac{1}{\bar{\rho}}\frac{\partial^2 p'}{\partial t \partial z} = 0$$

A simplification can be made to the above equation. As the mean density is steady-state, the quantity $-\frac{g}{\bar{\rho}}\frac{\partial \bar{\rho}}{\partial z}$ is a constant. This quantity is the Brunt-Väisälä frequency squared for the mean portion of the fluid.

$$N^2 = -\frac{g}{\bar{\rho}}\frac{\partial \bar{\rho}}{\partial z} \tag{D.12}$$

Substitution into equation (D.11) yields

$$\frac{\partial^2 w'}{\partial t^2} + N^2 w' + \frac{1}{\bar{\rho}}\frac{\partial^2 p'}{\partial t \partial z} = 0 \tag{D.13}$$

Equations (D.9) and (D.13) are a system of equations in two unknowns w' and p'. The next section assumes wave-like solutions to the two equations.

D.2 Solutions of Equations

Solutions to equations (D.9) and (D.13) are internal gravity waves. Wave-like solutions are assumed for w' and p' in order to find a dispersion relation for the frequency of the wave solutions. Finding a dispersion relation is useful for describing how gravity waves propagate. Plane wave solutions of the form $\psi' = \Psi \exp\left[i\left(\overrightarrow{K} \cdot \overrightarrow{r} - \omega t\right)\right]$ are assumed; where Ψ is a constant amplitude, $\overrightarrow{K} = (k, l, m)$ is the wavenumber, and ω is the constant frequency. Solutions of the form

$$w' = W \exp\left[i\left(\overrightarrow{K} \cdot \overrightarrow{r} - \omega t\right)\right] \tag{D.14}$$

and

$$p' = P \exp\left[i\left(\overrightarrow{K} \cdot \overrightarrow{r} - \omega t\right)\right] \tag{D.15}$$

are assumed.

To find the dispersion relation, equations (D.14) and (D.15) are first substituted into equation (D.13)

$$\frac{\partial^2}{\partial t^2}\left[W \exp\left[i\left(\overrightarrow{K} \cdot \overrightarrow{r} - \omega t\right)\right]\right] + N^2 W \exp\left[i\left(\overrightarrow{K} \cdot \overrightarrow{r} - \omega t\right)\right]$$

$$+\frac{1}{\bar{\rho}}\frac{\partial^2}{\partial t \partial z}\left[P \exp\left[i\left(\overrightarrow{K} \cdot \overrightarrow{r} - \omega t\right)\right]\right] = 0$$

$$(-i\omega)^2 W \exp\left[i\left(\overrightarrow{K} \cdot \overrightarrow{r} - \omega t\right)\right] + N^2 W \exp\left[i\left(\overrightarrow{K} \cdot \overrightarrow{r} - \omega t\right)\right]$$

$$+\frac{1}{\bar{\rho}}(-i\omega)(im) P \exp\left[i\left(\overrightarrow{K} \cdot \overrightarrow{r} - \omega t\right)\right] = 0$$

92

$$(-i\omega)^2 W + N^2 W + \frac{1}{\bar{\rho}} (-i\omega)(im) P = 0$$

$$-\omega^2 W + N^2 W + \frac{P\omega m}{\bar{\rho}} = 0$$

$$W(N^2 - \omega^2) + \frac{P\omega m}{\bar{\rho}} = 0$$

$$W = -\frac{\omega m}{\bar{\rho}(N^2 - \omega^2)} P \qquad\qquad (D.16)$$

Next, the assumed solutions are substituted into equation (D.9)

$$\frac{\partial^2}{\partial x^2}\left[P \exp\left[i\left(\overrightarrow{K} \cdot \overrightarrow{r} - \omega t\right)\right]\right] + \frac{\partial^2}{\partial y^2}\left[P \exp\left[i\left(\overrightarrow{K} \cdot \overrightarrow{r} - \omega t\right)\right]\right]$$

$$= \bar{\rho}\frac{\partial^2}{\partial z \partial t}\left[W \exp\left[i\left(\overrightarrow{K} \cdot \overrightarrow{r} - \omega t\right)\right]\right]$$

$$(ik)^2 P \exp\left[i\left(\overrightarrow{K} \cdot \overrightarrow{r} - \omega t\right)\right] + (il)^2 P \exp\left[i\left(\overrightarrow{K} \cdot \overrightarrow{r} - \omega t\right)\right]$$

$$= \bar{\rho}(im)(-i\omega) W \exp\left[i\left(\overrightarrow{K} \cdot \overrightarrow{r} - \omega t\right)\right]$$

$$(ik)^2 P + (il)^2 P = \overline{\rho}(im)(-i\omega)W$$

$$-P\left(k^2 + l^2\right) = \overline{\rho}m\omega W$$

$$P = -\frac{\overline{\rho}m\omega}{\left(k^2 + l^2\right)}W \tag{D.17}$$

Substituting equation (D.16) into (D.17) yields

$$P = -\frac{\overline{\rho}m\omega}{\left(k^2 + l^2\right)}\left(-\frac{\omega m}{\overline{\rho}\left(N^2 - \omega^2\right)}P\right)$$

$$\frac{P}{P}\frac{\overline{\rho}\left(N^2 - \omega^2\right)}{\omega m} = \frac{\overline{\rho}m\omega}{\left(k^2 + l^2\right)}$$

$$\left(N^2 - \omega^2\right) = \frac{m^2\omega^2}{\left(k^2 + l^2\right)}$$

$$\left(N^2 - \omega^2\right)\left(k^2 + l^2\right) = m^2\omega^2$$

$$N^2\left(k^2 + l^2\right) - \omega^2\left(k^2 + l^2\right) - m^2\omega^2 = 0$$

$$N^2\left(k^2 + l^2\right) - \omega^2\left(k^2 + l^2 + m^2\right) = 0$$

$$\omega^2 = N^2 \frac{(k^2 + l^2)}{(k^2 + l^2 + m^2)} \tag{D.18}$$

Equation (D.18) is the dispersion relation for gravity waves. For a wavenumber $\vec{K} = (0, 0, m)$, the frequency of the waves with respect to the mean wind is zero and thus there are no gravity waves. Therefore, phase propagation of gravity waves is not solely in the vertical, but at an angle to the vertical. This makes sense as the restoring force of gravity acts in the vertical and waves cannot oscillate solely in the horizontal. More on the propagation of gravity waves is covered in the next section.

D.3 Propagation

Gravity waves move in three different ways: by perturbation velocities, by phase velocities, and by group velocities. An unusual feature of gravity waves is that phase velocities are perpendicular to group velocities. For example, as plane waves propagate downwards, the group envelope of waves will propagate upwards, perpendicular to the phase velocities. Proof that phase velocities and group velocities are perpendicular comes by simply taking the inner product of the two and demonstrating that the result is zero, for the non-trivial case.

The phase velocity of gravity waves is given by

$$\vec{v_p} = \frac{\omega}{K} \left(\frac{\vec{K}}{K} \right) \tag{D.19}$$

and the group velocity is given by

$$\vec{c_g} = \left(\frac{\partial \omega}{\partial k}, \frac{\partial \omega}{\partial l}, \frac{\partial \omega}{\partial m} \right) \tag{D.20}$$

Substituting the dispersion relation (D.18) into the definitions for phase and group velocities yields

$$\vec{v_p} = \left(\frac{|N| K_H}{K^3} k, \frac{|N| K_H}{K^3} l, \frac{|N| K_H}{K^3} m \right) \tag{D.21}$$

and

$$\vec{c_g} = \left(\frac{|N| m^2}{K^3 K_H} k, \frac{|N| m^2}{K^3 K_H} l, -\frac{|N| K_H}{K^3} m \right) \tag{D.22}$$

where

$$K_H = \sqrt{k^2 + l^2} \tag{D.23}$$

Performing the inner product on the phase and group velocities yields

$$\vec{v_p} \cdot \vec{c_g} = \left(\frac{|N| K_H}{K^3} k, \frac{|N| K_H}{K^3} l, \frac{|N| K_H}{K^3} m \right) \cdot \left(\frac{|N| m^2}{K^3 K_H} k, \frac{|N| m^2}{K^3 K_H} l, -\frac{|N| K_H}{K^3} m \right)$$

$$= \left(\frac{|N| K_H}{K^3} k \right) \left(\frac{|N| m^2}{K^3 K_H} k \right) + \left(\frac{|N| K_H}{K^3} l \right) \left(\frac{|N| m^2}{K^3 K_H} l \right) + \left(\frac{|N| K_H}{K^3} m \right) \left(-\frac{|N| K_H}{K^3} m \right)$$

$$\vec{v_p} \cdot \vec{c_g} = \frac{N^2 m^2}{K^6} k^2 + \frac{N^2 m^2}{K^6} l^2 - \frac{N^2 K_H^2}{K^6} m^2$$

$$\vec{v_p} \cdot \vec{c_g} = \frac{N^2 m^2}{K^6} \left(k^2 + l^2 - K_H^2 \right)$$

96

Substituting in the definition of K_H from equation (D.23) shows

$$\vec{v_p} \cdot \vec{c_g} = \frac{N^2 m^2}{K^6} \left(k^2 + l^2 - \left(k^2 + l^2 \right) \right)$$

$$\vec{v_p} \cdot \vec{c_g} = \frac{N^2 m^2}{K^6} \left(0 \right)$$

$$\vec{v_p} \cdot \vec{c_g} = 0 \tag{D.24}$$

Therefore, phase velocities are perpendicular to group velocities. From the vertical components of equations (D.21) and (D.22) it can be seen that phase velocities and group velocities have the same magnitude in the vertical, but opposite sign.

Bibliography

1. Doggett, M. K., M. Squires, and R. Kiess. "An Evaluation of the Quality of Local Climate Statistics Generated from the Output of a 3-D Mesoscale Atmospheric Model," *Preprints, 11th Conf. on Applied Climatology, 1999, Dallas, TX.* 344-349. American Meteorological Society.

2. General Accounting Office. *Theater Missile Defense: Significant Technical Challenges Face the Airborne Laser Program.* GAO/NSIAD-98-37. October 1997.

3. Hajek, D. L. *Regression Analysis of Radar Measured Optical Turbulence with Synoptic Scale Meteorological Variables.* MS thesis, AFIT/GM/ENP/98M-03. School of Engineering, Air Force Institute of Technology (AU), Wright-Patterson AFB OH, March 1998.

4. Johnson, M. "Atmospheric Development for ABL," ABL-AFOSR Atmospheric Workshop. Kirtland AFB, 26 July 2000.

5. Johnson, M. Chief, ABL Atmospheric Development Branch. Electronic Message. 144500Z, 13 November 2000.

6. Kalnay, E. and others. "The NCEP/NCAR 40-Year Reanalysis Project," *Bulletin of the American Meteorological Society, 77*: 437-471 (March 1996).

7. Kundu, P. K. *Fluid Mechanics.* New York: Academic Press, 1990.

8. List, R. J. *Smithsonian Meteorological Tables.* Washington: Smithsonian Institution, 1951.

9. Nastrom, G. D. and F. D. Eaton. "The Coupling of Gravity Waves and Turbulence at White Sands, New Mexico, from VHF Radar Observations," *Journal of Applied Meteorology, 32*: 81-87 (January 1993).

10. Nastrom, G. D. and F. D. Eaton. "Variations of Winds and Turbulence Seen by the 50-MHz Radar at White Sands Missile Range, New Mexico," *Journal of Applied Meteorology, 34*: 2135-2148 (October 1995).

11. Tatarski, V. I. *Wave Propagation in a Turbulent Medium.* New York: McGraw-Hill Book Company, 1961.

12. VanZandt, T. E. and others. "Vertical Profiles of Refractivity Turbulence Structure Constant: Comparison of Observations by the Sunset Radar with a New Theoretical Model," *Radio Science, 13*: 819-829 (September 1978).

13. Weber, B. L. and D. B. Wuertz. *Quality Control Algorithm for Profiler Measurements of Winds and Temperatures.* NOAA TM-ERL-WPL-212. October 1991.

Vita

Captain Jeffrey W. Budai attended Texas A&M University under the Air Force Institute of Technology's Airman Education and Commissioning Program. He graduated with a Bachelor of Science degree in Meteorology in May 1995. In September 1995, he received his commission from the Air Force Officer Training School. In August 1999, after an assignment to Germany and an assignment with the Air Force Research Laboratory, he entered the Graduate School of Engineering and Management, Air Force Institute of Technology.

REPORT DOCUMENTATION PAGE

1. REPORT DATE (DD-MM-YYYY) 01-03-2001	2. REPORT TYPE Master's Thesis	3. DATES COVERED (From – To) Sep 1999 – Mar 2001

4. TITLE AND SUBTITLE

ANALYZING THE EFFECTS OF METEOROLOGY ON RADAR MEASURED INDEX OF REFRACTION STRUCTURE PARAMETER

5a. CONTRACT NUMBER

5b. GRANT NUMBER

5c. PROGRAM ELEMENT NUMBER

6. AUTHOR(S)

Jeffrey W. Budai, Captain, USAF

5d. PROJECT NUMBER

5e. TASK NUMBER

5f. WORK UNIT NUMBER

7. PERFORMING ORGANIZATION NAMES(S) AND ADDRESS(S)

Air Force Institute of Technology
Graduate School of Engineering and Management (AFIT/EN)
2950 P Street, Building 640
WPAFB, OH 45433-7765

8. PERFORMING ORGANIZATION REPORT NUMBER

AFIT/GM/ENP/01M-1

9. SPONSORING/MONITORING AGENCY NAME(S) AND ADDRESS(ES)

SMC/TMAB
Major Michael Johnson
3300 Target Rd
Kirtland AFB, NM 87117-5776

10. SPONSOR/MONITOR'S ACRONYM(S)

11. SPONSOR/MONITOR'S REPORT NUMBER(S)

12. DISTRIBUTION/AVAILABILITY STATEMENT

APPROVED FOR PUBLIC RELEASE; DISTRIBUTION UNLIMITED.

13. SUPPLEMENTARY NOTES

14. ABSTRACT

Forecasting optical turbulence is essential for the Air Force's Airborne Laser program to optimize placement of aircraft. To find how meteorology affects C_n^2, the intensity of turbulence in the index of refraction, case studies of synoptically interesting times are first chosen. Correlation coefficients are then computed between radar measured C_n^2 and meteorological quantities. The potential for mechanically turbulent activity is looked at. In the analysis of this work, six meteorological features were found likely to affect C_n^2. Two features associated with affecting potential refractivity, and thus C_n^2, are jets and inversions. North of jet core level in the northern hemisphere, higher values of C_n^2 can be found north of the core, with lower values to the south. With temperature inversions, typically higher values of C_n^2 can be found just above inversions with comparatively lower C_n^2 values underneath. The remaining four features affecting C_n^2 are not directly related to potential refractivity alone. The first is bands of high C_n^2 occurring within regions of strong vertical wind shear. The second feature is high C_n^2 occasionally seen underneath inversions during the approach of jets that are associated with gravity wave activity. The other two meteorological features are tropopause boundaries and trough passage.

15. SUBJECT TERMS

Index of Refraction, Atmospheric Refractive Index, Potential Refractivity, Optical Turbulence, Turbulence, Radar Measurements, Electromagnetic Wave Propagation, Meteorological Phenomena

16. SECURITY CLASSIFICATION OF:			17. LIMITATION OF ABSTRACT	18. NUMBER OF PAGES	19a. NAME OF RESPONSIBLE PERSON Lt Col Michael K. Walters, ENP
a. REPORT UNCLASSIFIED	b. ABSTRACT UNCLASSIFIED	c. THIS PAGE UNCLASSIFIED	UL	113	19b. TELEPHONE NUMBER (Include area code) (937) 255-3636, ext. 4681

REPORT DOCUMENTATION PAGE

The public reporting burden for this collection of information is estimated to average 1 hour per response, including the time for reviewing instructions, searching existing data sources, gathering and maintaining the data needed, and completing and reviewing the collection of information. Send comments regarding this burden estimate or any other aspect of the collection of information, including suggestions for reducing this burden to Department of Defense, Washington Headquarters Services, Directorate for Information Operations and Reports (0704-0188), 1215 Jefferson Davis Highway, Suite 1204, Arlington, VA 22202-4302. Respondents should be aware that notwithstanding any other provision of law, no person shall be subject to an penalty for failing to comply with a collection of information if it does not display a currently valid OMB control number. **PLEASE DO NOT RETURN YOUR FORM TO THE ABOVE ADDRESS.**

1. REPORT DATE (DD-MM-YYYY) 01-03-2001	2. REPORT TYPE Master's Thesis	3. DATES COVERED (From – To) Sep 1999 – Mar 2001

4. TITLE AND SUBTITLE

ANALYZING THE EFFECTS OF METEOROLOGY ON RADAR MEASURED INDEX OF REFRACTION STRUCTURE PARAMETER

5a. CONTRACT NUMBER

5b. GRANT NUMBER

5c. PROGRAM ELEMENT NUMBER

6. AUTHOR(S)

Jeffrey W. Budai, Captain, USAF

5d. PROJECT NUMBER

5e. TASK NUMBER

5f. WORK UNIT NUMBER

7. PERFORMING ORGANIZATION NAMES(S) AND ADDRESS(S)

Air Force Institute of Technology
Graduate School of Engineering and Management (AFIT/EN)
2950 P Street, Building 640
WPAFB, OH 45433-7765

8. PERFORMING ORGANIZATION REPORT NUMBER

AFIT/GM/ENP/01M-1

9. SPONSORING/MONITORING AGENCY NAME(S) AND ADDRESS(ES)

SMC/TMSW
Major Michael Johnson
3300 Target Rd
Kirtland AFB, NM 87117-5776

10. SPONSOR/MONITOR'S ACRONYM(S)

11. SPONSOR/MONITOR'S REPORT NUMBER(S)

12. DISTRIBUTION/AVAILABILITY STATEMENT

APPROVED FOR PUBLIC RELEASE; DISTRIBUTION UNLIMITED.

13. SUPPLEMENTARY NOTES

14. ABSTRACT

Forecasting optical turbulence is essential for the Air Force's Airborne Laser program to optimize placement of aircraft. To find how meteorology affects C_n^2, the intensity of turbulence in the index of refraction, case studies of synoptically interesting times are first chosen. Correlation coefficients are then computed between radar measured C_n^2 and meteorological quantities. The potential for mechanically turbulent activity is looked at. In the analysis of this work, six meteorological features were found likely to affect C_n^2. Two features associated with affecting potential refractivity, and thus C_n^2, are jets and inversions. North of jet core level in the northern hemisphere, higher values of C_n^2 can be found north of the core, with lower values to the south. With temperature inversions, typically higher values of C_n^2 can be found just above inversions with comparatively lower C_n^2 values underneath. The remaining four features affecting C_n^2 are not directly related to potential refractivity alone. The first is bands of high C_n^2 occurring within regions of strong vertical wind shear. The second feature is high C_n^2 occasionally seen underneath inversions during the approach of jets that are associated with gravity wave activity. The other two meteorological features are tropopause boundaries and trough passage.

15. SUBJECT TERMS

Index of Refraction, Atmospheric Refractive Index, Potential Refractivity, Optical Turbulence, Turbulence, Radar Measurements, Electromagnetic Wave Propagation, Meteorological Phenomena

16. SECURITY CLASSIFICATION OF:			17. LIMITATION OF ABSTRACT	18. NUMBER OF PAGES	19a. NAME OF RESPONSIBLE PERSON Lt Col Michael K. Walters, ENP
a. REPORT UNCLASSIFIED	b. ABSTRACT UNCLASSIFIED	c. THIS PAGE UNCLASSIFIED	UL	113	19b. TELEPHONE NUMBER (Include area code) (937) 255-3636, ext. 4681